UNIVERSITÀ
DI PARMA

DOTTORATO DI RICERCA IN

SCIENZE CHIMICHE

CICLO XXX

Crystal structure and defectiveness in modified Metal-Organic Frameworks

Dottorando:

Stefano Canossa

Coordinatore:
Chiar.mo Prof. Roberto Corradini

Relatore:
Chiar.mo Prof. Giovanni Predieri

Co-relatrice:
Chiar.ma Prof. Alessia Bacchi

A.A. 2014-2017

To my Parents

To my Professors

To my Friends

To my Foes

To myself

While there's a teacher,

There's a purpose.

Index

Addendum

Appendix 101

Introduction

三十輻共一轂當其無有車之用

埏埴以為器當其無有器之用

鑿戶牖以為室當其無有室之用

故有之以為利無之以為用

The thirty spokes unite in the one nave; but it is on the empty space, that the use of the wheel depends.

Clay is fashioned into vessels; but it is on their empty hollowness, that their use depends.

The door and windows are cut out to form an apartment; but it is on the empty space, that its use depends.

Therefore, what has a positive existence serves for profitable adaptation, and what has not that for actual usefulness.

道德經

Dao De Jing

0.1 · Metal-Organic frameworks

"I am not afraid to consider the final question as to whether, ultimately - in the great future- we can arrange the atoms the way we want. The very atoms, all the way down!" [1]

Being about to give a brief description of what Metal-Organic Frameworks (MOFs) are, I love to recall the words of an enthusiastic, almost impatient Richard Feynman while giving an inspiring talk at the American Physical Society meeting in late December 1959[1]. At those times, materials were mostly considered as solids obtained from raw materials by means of mechanical treatments (grinding, engraving, assembly, etc.), or by melting and solidifying into moulds.

This approach, called "*top-down*", differs substantially from the synthetic chemistry approach, which uses molecular or atomic precursors to assemble its final substances on an atomic scale. Predicting this change, the legendary Feynman imagined a "*great future*" when materials themselves could be created by assembling their component in a controlled manner, atom by atom (or molecule by molecule), thus allowing a fine tuning of their structure and composition ("*bottom-up*" approach). A few decades later, this revealed to be much more than a mere daydreaming of an outstanding Nobel laureate physicist, and a brand-new branch of materials science came to light: Nanotechnology.

At this point, an outsider may point out: where can we place MOFs in this panorama? Since we synthesize these materials by selecting their building blocks, i.e. the atomic or molecular constituents, and providing the convenient conditions for them to assembly in an engineered way, we can surely state that MOFs are one of the most glaring example of arranging atoms and molecules "the way we want", exactly as Prof Feynman foresaw. Thus, we are truly in the real depths of Nanotechnologies, and we are navigating in a precise region, namely Crystal Engineering.

To conclude this prelude, I think a short yet clear definition of this peculiar combination of terms is due, and I leave such a responsibility to Professors Desiraju, Ramanan and Vittal by quoting the starting sentence of their book on the subject[2] :

"*Crystal engineering is the understanding of intermolecular interactions in the context of crystal packing and the utilization of such understanding in the design of new solids with desired physical and chemical properties*."

0.1.1 · Definition and major features

Metal-Organic Frameworks are functional materials, usually crystalline, formed by a 2- or 3-dimensional network of coordinative bonds between organic molecules and metals or metal oxo-clusters. By giving this very flexible definition, we set aside some other requirements that are considered crucial by some eminent researchers in the field.

As an example, the most controversial and discussed one is the presence of accessible voids, which should be proven by gas sorption isotherm measurements. The latter is subtly supported by the International Union of Pure and Applied Chemistry since, in a dedicated paper dated July 2013[3], Batten S. R. et al stated: "*A metal-organic framework, abbreviated to MOF, is a coordination network with organic ligands containing potential voids.*"

To date, the definition of MOF remains rather vague and very close to the one of "coordination polymers", the main difference being the dimensionality of the coordination network, which should be higher than 1-D in the case of MOFs (Figure 0.1).

For our purposes, we can consider a MOF as an infinite alternation of organic molecules and metal centres or oxo-clusters, extending in three dimensions and resulting in a crystalline material with proven porosity. Bearing this in mind, we define "**Secondary Building Units**" (**SBUs**) the inorganic clusters present in the solid phase, and "**linkers**" the organic molecules bridging together the SBUs.

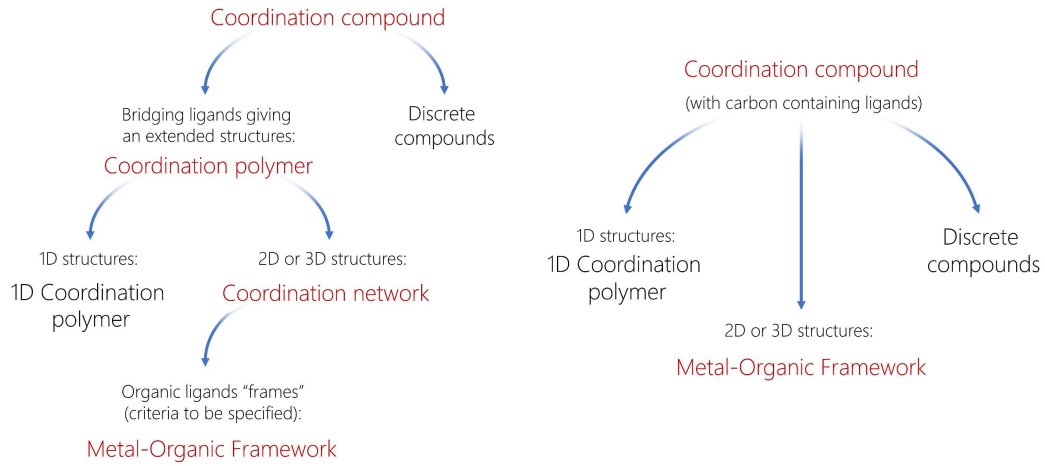

Figure 0.1. *Tentative hierarchies of coordination polymers and Metal-Organic Frameworks, as presented by Batten et al [4] (left) and O'Keeffe et al [5] (right).*

So far, we justified the term "metal-organic" and explained what "framework" is supposed to mean, but there is much more to be said about MOFs, aside from their structural arrangement. The first and most important feature of MOFs is the possibility to engineer their composition and structure and confer to the final material the properties needed for a certain use. This means that it is virtually possible to use any linker and SBU desired for a target MOF, and this is done by designing, synthesising and functionalising the organic ligands, and choosing the metal that will form the final SBUs.
However, in reality, these possibilities are limited by three important factors. First: the linker attainment relies on organic synthesis, and, after having designed a promising molecule inspired by its potential use for a novel MOF, its synthesis may be more or less difficult. Another even more strong limitation is given by the fact that there is much less freedom in the design of the SBU than there is with the linkers. As a matter of fact, the list of metal aggregates occurring in MOF chemistry is not very long, and while using a certain metal, it is likely to observe one of these SBUs in the final material (Figure 0.2).

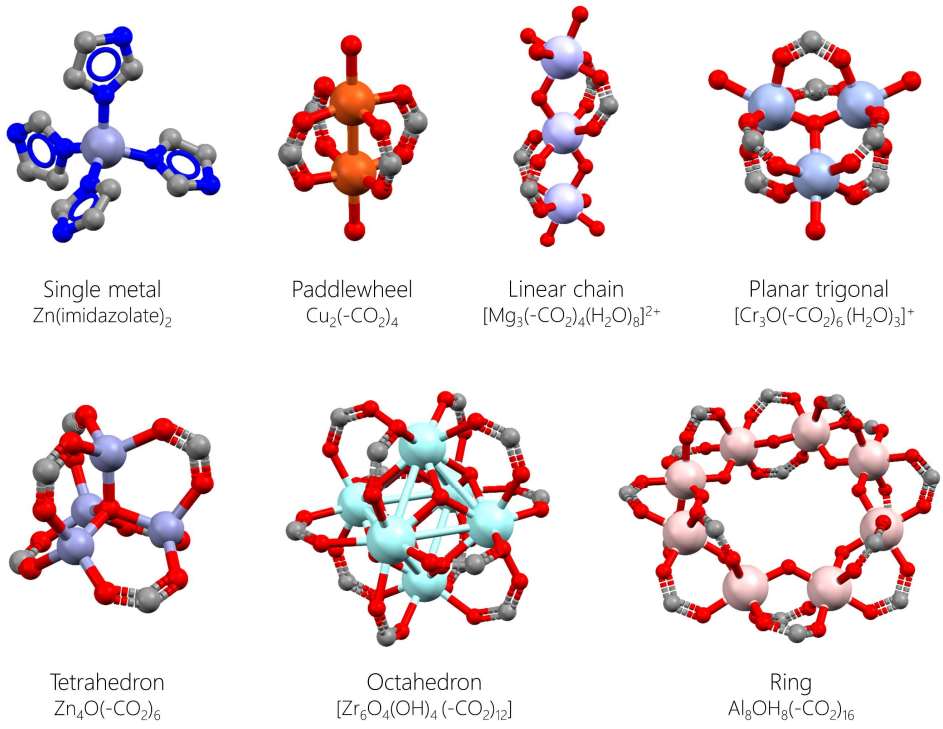

Figure 0.2. A few examples of the most remarkable SBU types in MOF chemistry. The examples are only indicative of the SBU geometry; several example of similar geometries with metal centres different from the represented ones can be found.

The third aspect that limits the possible affordable MOFs is the required synthetic procedure. First of all, it takes place under kinetic control and therefore some forms or polymorphs of certain MOFs are not easily affordable, especially if metastable.
Furthermore, MOFs are classically synthesized under solvothermal conditions and this could give more weigth to this aspect by limiting the number of synthesizable phases.
Additional limitations are given by the linkers solubility, which is generally very low in the vast majority of available solvents. In fact, the syntheses are often carried out in N,N'-dimethylformamide or similar media and, importantly, usually require heating (up to 393K).
All these challenging aspects however fail in discouraging passionate researchers whose aim is to develop and study new materials in this field. This is not only because of the researchers inherent attraction for hard tasks and scientific exploration.
As already mentioned, MOFs are currently among the most promising functional materials. Therefore, research efforts in this field are mostly focused on their applications, which constitute the main driving force and funding source. A general overview on this topic will be provided in the following paragraph.

0.1.2 · Functional properties and applications

While discussing about materials and considering porous solids, the attention inevitably shifts from the crystalline phase towards its voids, either they belong to the periodic structure itself or to defects and other deviations from the ideal perfect crystals.
This does not mean that the crystal phase structure and composition is irrelevant for the material application, but that its behaviour (and therefore the application itself) depends on both the crystalline and the cavities part. After some examples, this will become immediately clear.
What follows is not intended to be an exhaustive overview on MOFs applications, since it would require much more than one chapter to cover every use, describe it and give an up-to-date point of view on this topic. This is neither the aim of this part, nor is strictly related to the subject of the present work. Therefore, only some indicative examples are presented, just to give an idea on how versatile these materials are and to understand why nowadays so much attention and research efforts are paid to them.

0.1.2.1 · Catalytic applications

In 1999 Li et al. reported the synthesis and structure of MOF-5[6], a robust MOF with 61% porosity and a Brunauer-Emmett-Teller (BET) surface area of 2320 m^2/g, substantially higher than the ones commonly found for zeolites and activated carbon[7].

Since this research was published, the number of new reported MOFs suddenly increased, and the pursuit of a higher internal surface area became one leitmotif in this field (Figure 0.3), because of the central importance held by the surface area in heterogeneous catalysis. This theme remained an evergreen in MOFs chemistry.

The first example of catalysis in an extended framework dates back to 1994, when a Cd-based framework [Cd(4,4'-bipyridine)$_2$(NO$_3$)$_2$] was used for an effective cyanosilylation of aldehydes as a result of axial ligand removal, highlighting at the same time the size-selectivity of MOF catalysts, which are able to exclude large substrates from the pores[8].

In this case, the lead role in the MOF structure is played by the organic part, but there are manifold papers describing MOF-based catalysts acting by accepting additional coordination to the SBU metal centres, especially if coordinatively unsaturated.

Usually such sites act as Lewis acid catalysts, and the mother of all examples in this case is [Cu$_3$(benzene-1,3,4-tricarboxylate)$_2$], known as HKUST-1[9]. This was indeed found able to catalyse isomerisations, cyclisations and other rearrangements thanks to its coordinatively unsaturated paddlewheel-like SBUs.

By going deeper in the literature, MOFs are found to catalyse also methane oxidation[10] hydroxylation and epoxidation of olefins[11], Michael addition and Henry reaction[12], water splitting[13], and many others.

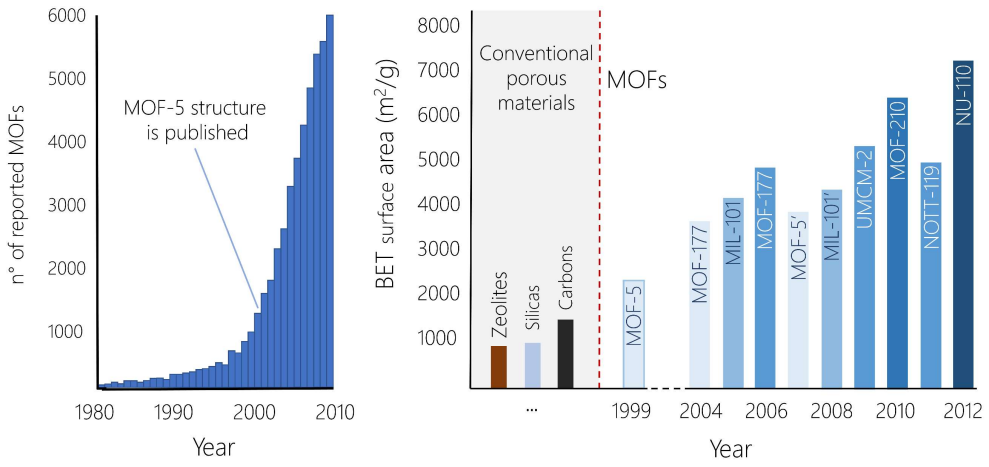

Figure 0.3. Some noteworthy data regarding MOFs research popularity and performances through the last decades, as reported by Furukawa et al[14]. On the left, the graph shows the increase of MOFs reported structure from late '70s to 2010, highlighting the impact that the discovery of MOF-5 had on the shift of the scientific community to these solids. On the right, some outstanding MOFs adsorption performances compared to those of conventional inorganic porous materials.

0.1.2.2 · Environment-oriented applications

In the present times, mankind is facing an overall change of the earth behaviour caused by human activities on the environment. This change is so dramatic and its effects so serious that many geologists usually refer to it with a specific term: **Anthropocene**[15,16]. The most renowned effect belonging to this phenomenon is a global-scale climate change whose main and most dangerous feature is the raise of the earth atmosphere temperature with a worrying exponential-like trend[17]. In such a context, the Scientific Community must have a firm position and the moral duty to work towards a solution. Since the main responsible for this problem has been identified by manifold studies in the increasing amount of carbon dioxide (Figure 0.4) due to human abuse of fossil fuels for energy production, the main target of the current scientific fight against climate change is to find feasible ways to sieve this pollutant from the atmosphere and to satisfy the energy demand of human society by means of combustion-free technologies.

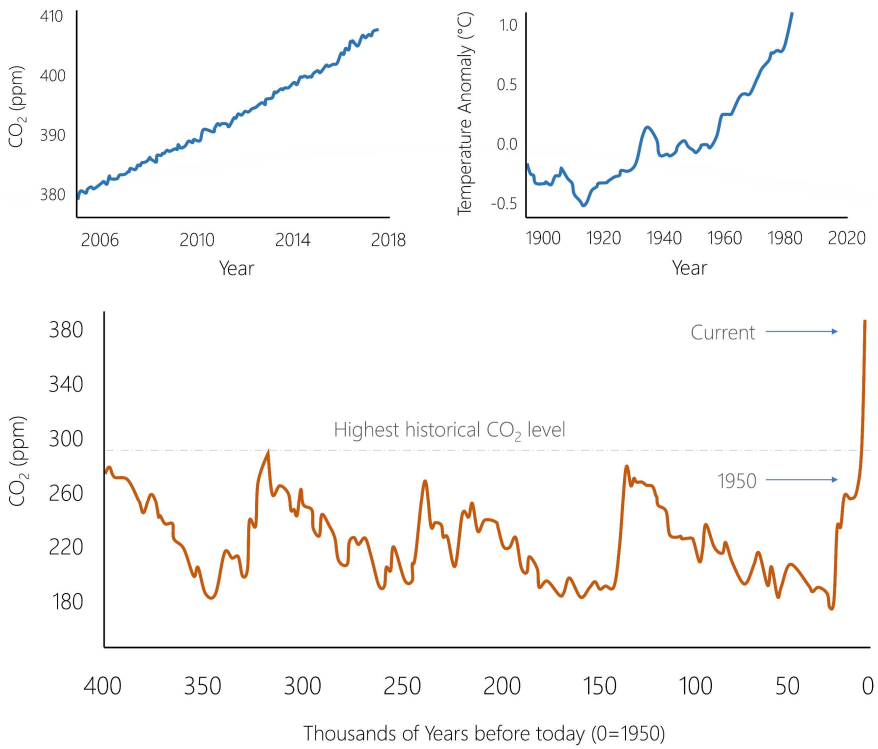

Figure 0.4. Above, CO_2 concentration trends during the last decade (a) and from 400.000 years ago to the present year (b). Below, the global land-ocean temperature index. The data was recorded by the US National Oceanic and Athmospheric Administration and are freely available on the NASA web-site[18].

In this panorama, MOFs could really make the difference. For instance, high surface area MOFs can trap a remarkable amount of CO_2 in their cavities[19]. In this manner, they can act like sieving materials, but also potentially convert the guests or store them for a further conversion in non-polluting chemicals[20].
Furthermore, MOFs also contribute to pursue more sustainable and carbon-free sources of energy. The most remarkable example of their contribution in this regard is the use in hydrogen-fuelled engines and power supplies. This is due to MOFs potential high hydrogen storage capacity at moderate and more safe pressure conditions, thus limiting the main concerns regarding hydrogen-powered energy sources[21,22].

0.1.2.3 · Biomedical applications

It is not surprising that, among the main research fields looking at MOFs potentialities, pharmaceutical chemistry occupies an important space. In this field, these materials can be a "transport shuttle" or a "showcase" for target drug molecules.
As for the "transport shuttle" application, this is basically a drug storage and delivery. Target drugs can be trapped by means of weak forces (electrostatic, H-bond or π interactions, coordination to an unsaturated metal centre, etc.) inside MOF crystals. Then, these could be taken as ingestible powder, and the drug released with a certain rate, which is achieved by designing the inner chemically active sites of the solid[23–26].
Obviously, the chosen MOFs should be biocompatible, therefore allowing the use of only a few types of metals, mostly Zr, Fe, Mg or Zn, and low toxicity linkers[27,28].
Another interesting application of MOFs in biomedical research is more strictly related to the characterisation of new drugs. The determination of the absolute configuration of a drug is a well-known major issue in pharmaceutical research, since undesired enantiomers, even in small quantities, could have dangerous effects on the patient.
As a matter of fact, the identification of a specific drug enantiomer usually relies on the structure determination by SCXRD or NMR spectroscopy. However, not rarely the enantiomer assignment by NMR can be complicated, and no single crystal suitable for SCXRD can be grown.
In these cases, MOFs can be used as a "showcase". The target molecule can be trapped inside the pores of the material, where it will be adsorbed to specifically designed sites.
This method became renowned in recent years with the name of Crystalline Sponge Method[29]. In this way, the desired molecule remains immobilised and most likely ordered throughout the solid phase, and can be "observed" by performing SCXRD on the loaded MOF[30,31].

0.1.2.4 · Chemical sensors

One last application to be mentioned concerning MOFs is their use as chemical sensors. Given the exceptional tunability of their structures, it is easy to realise the potential use of MOFs as containers where a molecular guest can enter and trigger a chemical or physical response[32]. This reaction can be therefore detected to provide information on the nature and quantity of trapped molecules. In this field, the main aim is to design and synthesize MOFs with remarkable sensitivity, selectivity, response time, structural stability and reusability.

Without going into specific details, usually the signal sent by the material after having trapped a target molecule can be a change in the absorption of light of the MOF (solvatochromism[33], vapochromism[34,35], field effects[36]) or alterations of peculiar luminescence behaviours (quenching/enhancement[37], radioluminescence[34,38]). In this regard, many devices have been developed for the detection of organic molecules, as well as ions and even radiations.

Further explored possibilities are also the design of chiral framework able to perform preferential enantiomer sorption[39] or the construction of an array-based device containing several different MOFs that collectively act as a chemical nose[40,41]. These are only a few examples of this type of applications, whose number is constantly increasing together with the type of the sensed analytes and the device architectures.

0.2 · Post-Synthetic Modifications

Given the huge MOFs potential, the mentioned difficulties concerning their synthesis can be easily accepted as promising challenges. However, as a matter of fact, there are limitations to the possible range of materials we can synthesize. For this reason, crystal engineers found a way to circumvent this unavoidable disadvantage: the use of **Post-Synthetic Modifications**[42] (**PSM**, Figure 0.5). All PSM techniques can be grouped into two main classes: **framework functionalisation** and **linker/cation exchange**.

The first is the most obvious one, since it is easy to imagine of using the chemical species constituting the framework as reagents for a functionalisation[43]. In facts, what is commonly done in this regard is to adopt, for a MOF synthesis, a linker with a certain functional group, which will not play any structural role in the final solid. In this way, it is possible to introduce in the synthesized MOF molecules able to react with the mentioned functional group, thus binding irreversibly to the framework. Eventually, these molecules will remain in the cavities, ready to interact with potential incoming guests.

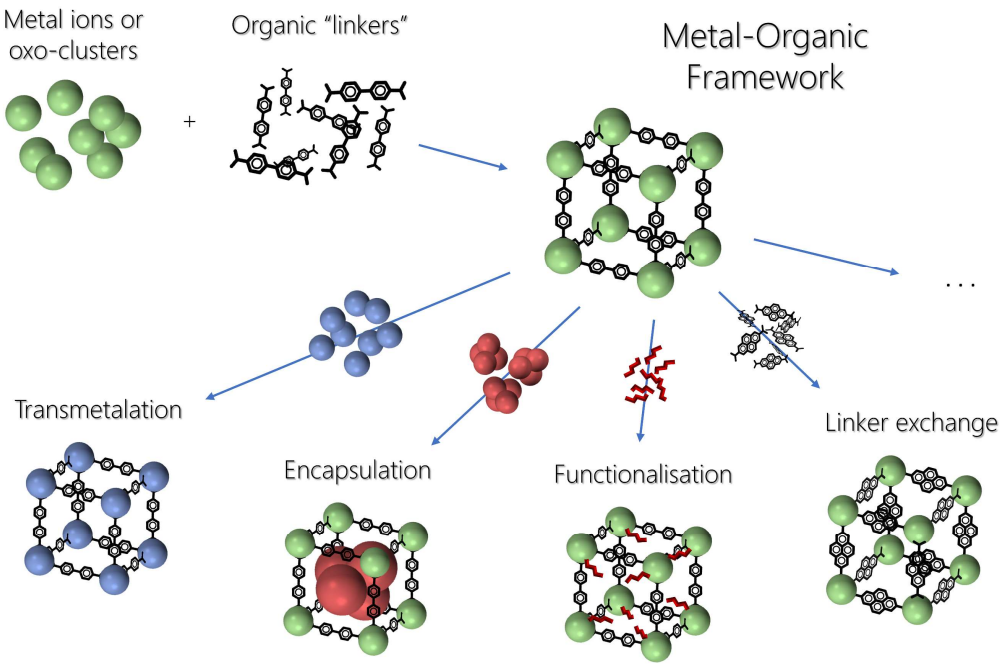

Figure 0.5. Graphical simplification of some noteworthy Post-Synthetic Modifications in MOF chemistry.

The post-synthetic exchange of metal centres or linkers in a MOF without any alteration of its arrangement might be considered as an improbable phenomenon.
Actually, MOFs are much keener to this behaviour than a general coordination chemist could expect, and this becomes an important advantage while dealing with synthesis of phases that are not affordable for kinetic reasons.
The most studied transformation of this kind is the **Post-synthetic Ion Metathesis** (**PSIM**), also known as **Transmetalation**[44], which is basically the exchange of the starting framework metal centres with external ones coming from the surrounding environment (Figure 2.1, Chapter II). Obviously, the coordination geometry of the substituting metals should be compatible with that of the native ones, otherwise the substitution will not be isostructural and the phase integrity will not survive the transformation.
Transmetalation is not only captivating for the phenomenon itself, but is a useful strategy to achieve materials whose properties are due to the presence of one specific metal (e.g., magnetic properties) or improved after the cation substitution, as in the cases of better gas absorption exhibited by Cu or Co substituted analogues of Zn-based MOFs[45,46].
All PSMs usually come with more or less severe damages to the treated materials. Therefore, XRD studies are not always feasible, both for possible losses of crystallinity and the creation of static disorder. This aspect will have an important impact on the described work.

0.3 · Structure determination: noteworthy aspects

Since the structural characterisation by **Single Crystal XRD** (**SCXRD**) will constitute an important part of the present work, some aspects regarding the use of this analysis on Metal-Organic Frameworks are discussed below. This will come in useful when some peculiar features of the diffraction patterns are considered, and therefore the general behaviour of MOFs in XRD measurements should be a common basic knowledge.
Assuming that the reader is familiar with SCXRD performed on molecular crystals, in which aspects is this analysis on MOFs different and which are the main difficulties that a crystallographer working with these materials usually face?

0.3.1 · Effects of porosity

The first important peculiarity in this regard is due to MOFs structure and, more precisely, to their porosity. The **presence of voids** has two detrimental effects on X-ray diffraction experiments. First, in a highly porous MOF the number of atoms contributing to the coherently diffracted intensities is much lower with respect to a non-porous solid with the same chemical composition. This is caused by the fact that the ordered fraction of the solid has a volume which is remarkably lower with respect to the total, and therefore big-size single crystals usually diffract much worse than expected by only considering their volume. Together with the difficulties in growing decent MOF single crystals in terms of size, this makes the use of synchrotron radiation sometimes necessary to have high resolution data from MOFs.
Another negative effect of the voids presence is caused by their content. In facts, MOFs are usually full of molecules (gases or solvents), and these are, in most cases, disordered or short-range-ordered without any relevant structural correlation with the host crystalline phase. This results in incoherently scattered X-rays, whose presence contributes to the total intensity found in the Bragg peaks. As a result, the agreement between the intensities calculated from the modelled structure and the measured ones gets unavoidably worse.
One widespread practice, which is used by crystallographers to limit the effect of the voids content, is the use of the "**SQUEEZE**" command of the crystallographic program PLATON[47] or similar analogues from other structure refinement software (the "**Mask**" function in Olex2[48]). These tools start by defining a region where only disordered unmodeled species are present, i.e., all the space which is not occupied by any assigned atom. Then, a back-Fourier transform is performed on the electron density belonging to these regions to obtain the void content structure factor. Eventually, the latter is used together with the structure factor of the modelled phase to describe the total measured Bragg intensities.

In this way, a new set of reflections is written and used for the structure refinement, resulting in a better agreement between the calculated intensities and the new "masked" ones. Since the measured intensities are not used anymore, the R-factor value decreases significantly, and the goodness of fit improves. However, it should be considered that by adopting this strategy we are choosing to use artificially tailored reflections while throwing away a non-negligible part of the measured scattered intensities, which are the information provided by the experiment.

0.3.2 · Effects of static disorder

The second aspect of MOFs structure which confers to these solids a peculiar behaviour in XRD experiments is the **presence of static disorder**. Defects are an essential part of every crystal phase, but while in most cases it can be ignored because of their low amount and the poor contribution to the total scattered intensities, in MOFs the deviations from the perfect crystalline state are usually far from being insignificant. However, until now, not so much attention is paid to the careful characterisation of static disorder in these materials.
There are two major causes of defectiveness in MOFs. One can be found in their synthesis, during which the chemical availability of the reagents or the fast kinetics of the phase growth after the nucleation may result in substitutional disorder events, e.g., missing linkers or missing metals/SBUs[49–51]. The second cause can be found in post-synthetic treatments, which are rarely safe for the solid phase, and might cause both substitutional and positional disorder.
Lately, disorder in MOFs has become a relevant topic, although very complex and delicate to deal with, and an increasing number of research studies are focusing on the so called "**Defect engineering**"[52], the purpose being to design and achieve specific concentrations and types of defect, to influence the final properties of the target material in a reproducible way.
Returning to XRD analyses, defects are the reason why MOFs diffraction patterns usually exhibit a remarkable amount of diffuse scattering. This also contributes, along with the scattering from the cavities content, in altering the Bragg measured intensities, and sometimes causes serious problems during the structure refinement. If the incoherent component is strong and the disorder in the solid has an important influence on its properties and behaviour, a total scattering approach is of undeniable importance to give the most complete possible description of the material.

0.4 · Thesis outline

In this last part of the introduction, some basic information regarding the thesis work are briefly provided. As already mentioned, the performed activities have been strongly devoted to accurate structural elucidations by SCXRD. The synthesis of functional new MOFs is thereby not present, nor is the characterisation of known MOFs functional properties, e.g. surface area, optic or magnetic behaviour, etc. At this point, the reader may rightly ask: if no new MOF is synthesized and most of the activities regard structural studies, what are the objects of these analyses and what is their purpose?

0.4.1 · The target and the real purpose

The performed activities aimed to modify a MOF by post-synthetic treatments, and to characterise the obtained phases. Overall, two PSM will be described: a transmetalation and a functionalisation of the MOF by the synthesis of Ti oxide nanoaggregates in its pores. The used solid is IRMOF-9, a renowned Zn-based MOF whose description will be provided in the next chapter.

The structural studies will focus on the starting and the final material, as well as on its intermediate stages during the modification. This special look at the evolving solid can be considered the real purpose of the work, since accurate structural information regarding MOFs during PSMs are rarely found in the literature. The most important benefit of the chosen approach is not so much the detailed description of the obtained material, which is essential to understand any of its functional features. What really makes the difference in this regard are the achievable information concerning the behaviour of the starting one during the PSM.

Any possible insight on the evolution of the solid could help in rationalising the reaction mechanisms and how the material reacts to the ongoing post-synthetic treatment. This is of special importance when dealing with MOFs, whose structures are all but fixed and inhert.

Chapter I

IRMOF-9

"All the kids were playing in the field and one kid said to me:
- See that bird, what kind of a bird is that? -
And I said: - I haven't the slightest idea what kind o f a bird it is -
He says: - It's a brown throated thrush, your father doesn't tell you anything -

But it was the opposite: my father had taught me.

Looking at a bird he says,
- Do you know what that bird is? It's a brown throated thrush.
But in Portuguese it's a *Jontelapero*, in Italian a *ciuttera pichidda*,
in Chinese it's a *Chung Long Ta*, in Japanese a *Potara Tokodacha* - et cetera.
- Now, you know in all the languages you want to know what the name of that bird is and when you've finished with all that, you'll know absolutely nothing whatever about the bird. -"

Richard P. Feynman

"The Pleasure of Finding Things Out"
1981

1.1 · Introducing IRMOF-9

The whole thesis work is focused on IRMOF-9, a renowned material whose entrance in the MOFs family dates back to 2002[53]. The reasons for this choice lie in a few but relevant advantages.

First, it can be grown in large and single crystals with a regular and thick shape, sometimes reaching more than 1 mm in length. This involves obvious advantages in Single Crystal X-Ray Diffraction (SCXRD) and Scanning Electron Microscopy (SEM) analyses, especially when laboratory instruments are used instead of synchrotrons and when separate analyses of different regions of the same crystalline domain are needed. Moreover, the synthesis is straightforward and relatively fast, and the structure is at the same time robust and flexible. This will become clear as soon as its characterisation will be described.

Concerning the name, IRMOF-9 stands for Iso-Reticular MOF-9, and this material is part of a series of MOFs with different organic linker but same topology and SBU. In the article where its structure has been described[53], Eddaoudi et al presented the systematic design and synthesis of iso-reticular MOFs as a proof-of-principle. For this reason, the related structures are reported without further investigations on possible presence of defects, instabilities to temperature changes/solvent exposure, or any other peculiar behaviour.

The present chapter describes the work done to reduce this gap, since information in this respect is of extreme importance while facing post-synthetic modifications and therefore the behaviour of the material to be modified is the first aspect to be known as much as possible.

1.1.1 · Synthesis and average structure

IRMOF-9 synthesis has been designed and optimised to obtain high-quality single crystals in terms of size, low amount of intergrown domains and crystallinity. The optimal procedure (paragraph A.1.1, Appendix), consists in a solvothermal reaction in N,N-dimethylformamide (DMF) of biphenyl-4,4′-dicarboxylic acid and $Zn(NO_3)_2 \cdot 6H_2O$. The product phase appears as colourless prismatic crystals (Figure 1.1, left).

If the synthesis is prolonged beyond 3 days, IRMOF-9 starts to disintegrate and another phase appears as colourless crystals with a hexagon-like shape (Figure 1.1, right). This phase has already been reported by Sapchenko et al[54] and its composition, which differs from IRMOF-9 in the presence of dimethylammonium ions (CCDC 769432[55]), suggests that the decomposition of the DMF during the synthesis plays a crucial role in the formation of this secondary phase.

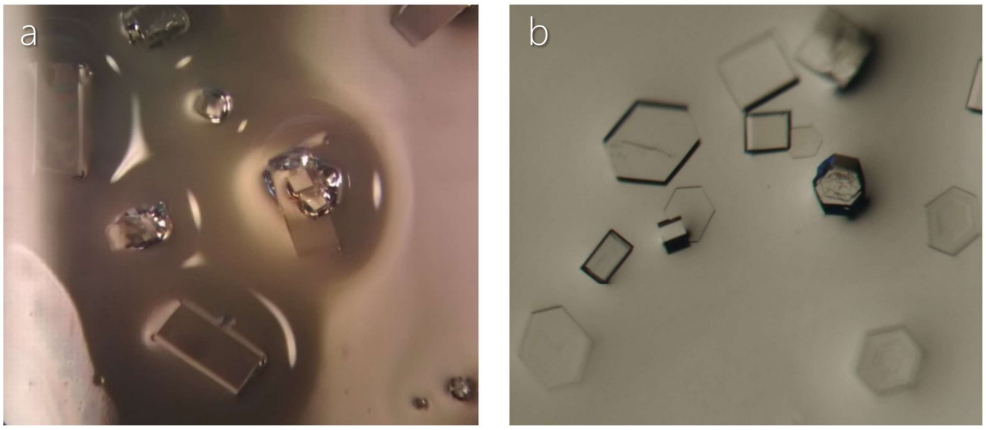

Figure 1.1. From the left: sample images of the crystals formed in the IRMOF-9 synthesis after 2 (a) and 3 (b) days. In the second image, the presence of the parasite phase is clearly recognisable.

As long as IRMOF-9 structure is concerned, its network is the result of the connection of Zn_4O SBUs by means of biphenyl-4,4'-dicarboxylate (**BPDC**) ions (Figure 1.2).
Each SBU is coordinated by six linkers, resulting in an octahedral building block (Figure 1.2, b). Consequently, the resulting framework should have a cubic symmetry, as in the case of MOF-5, which is made of the same SBUs bridged by terephtalate anions.
However, the system optimises the packing by forming a double interpenetrated lattice. For this reason, the final crystal system of the phase is not cubic but orthorhombic, and the space group is **Pnnm**.
The two involved networks interact with each other by performing a **linker-embrace** interaction between adjacent octahedral building blocks. This results in a slight but recognisable distortion of the cubic symmetry of the two single networks to a rhombic prismatic one.
The structure of IRMOF-9 is characterised by the presence of different kind of voids. The most important ones are the channels developing with a zig-zag trend along the *a* crystallographic axis. The channel aperture has a triangular shape, whose dimensions are 21.4 and 12.8 Å (Section A.3.2 Appendix), thus allowing the entrance of molecular guests of suitable size. Other minor cavities are present, which have smaller dimensions, but still large enough for the passage of light solvent molecules like H_2O or DMF. The smallest ones are those formed by the adjacent SBUs belonging to the two interpenetrated networks. These voids, however, are not accessible and contain a DMF molecule which is observed to be disordered in four positions (paragraph 1.1.2).

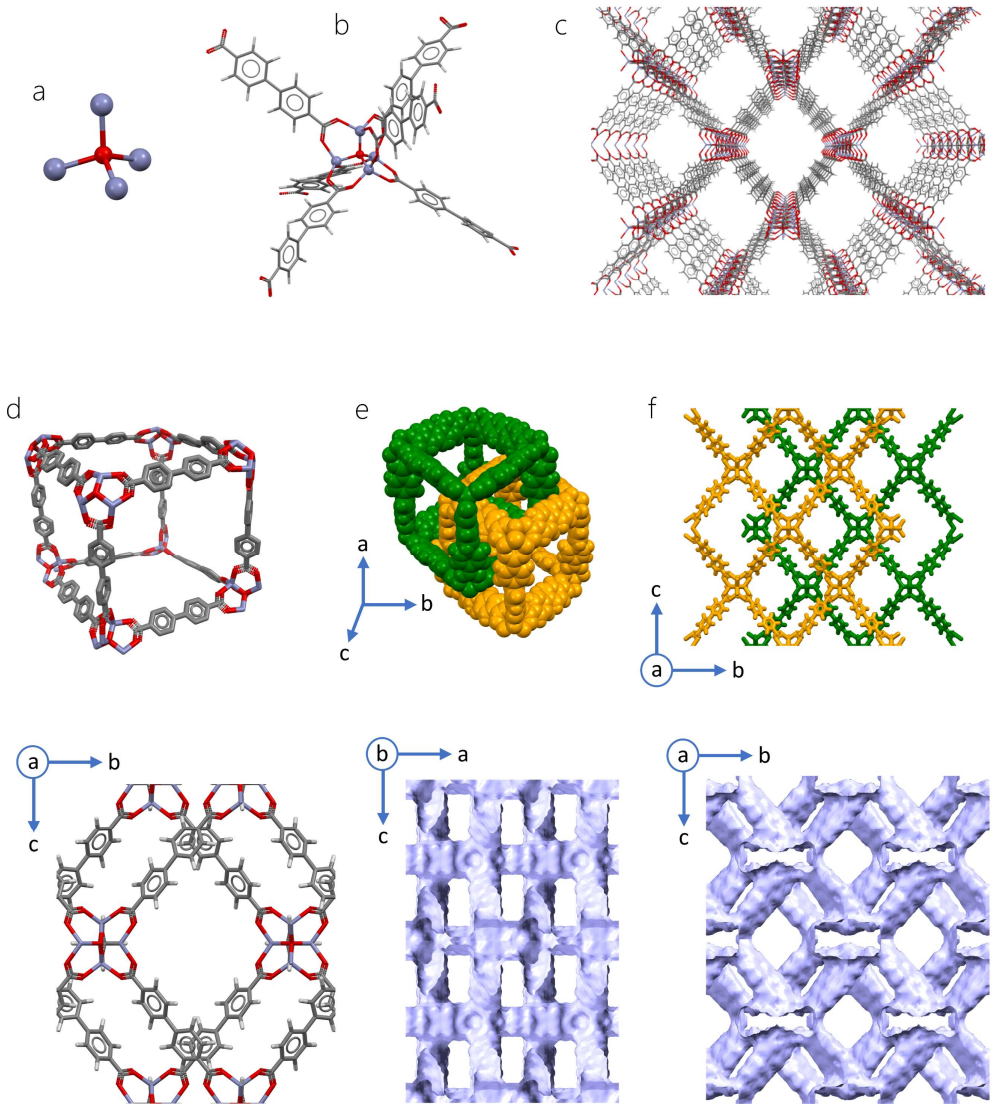

Figure 1.2. The structural features of IRMOF-9 are summarised. From the upper left corner, the Zn_4O SBU (a), the basic building block (b) and its arrangement in a single network (c) are shown. In the second line, the interpenetration is described by considering the cage formed by the connection of different SBUs in a single network (d). These pseudo cubic cages interlock (e), yielding the double interpenetrated lattice (f). Below, the complete unit cell is shown along the a axis, together with the external surface mapping along the b and a directions, performed using the "Display voids" function of the Mercury software[56].

Overall, the hollow volume amounts to 6884.11 $Å^3$, which constitutes the 68.9% of the total solid volume (details on the voids calculations can be found in paragraph A.3.1.1, Appendix). It is of fundamental importance to keep in mind that this space is always occupied mostly by disordered DMF molecules, and, in minor quantity, by H_2O, dimethylamine and formic acid, which are disordered as well.
The last three species are present because solvent used for the synthesis was not anhydrous, and therefore in the adopted conditions (383 K) DMF tends to decompose by reacting with water traces. This presence, which is not observable by means of XRD, will constitute an important active part of the material and will strongly influence its chemical and physical behaviour.

1.1.2 · Crystal quality and defectiveness

IRMOF-9 crystals usually appear as orthogonal prisms, not rarely truncated, and their size can range from 0.5 to more than 1 mm (the values are relative to the synthesis reported in paragraph A.1.1, Appendix).
The crystallinity is another virtue of this material, since the specimens feature a few damages after the synthesis. To confirm this qualitatively, some crystals have been soaked in DMF solutions of Methylene blue and Rhodamine 101 for 30 days (paragraph A.1.2, Appendix). The two molecules were chosen because of their strong colour and different molecular sizes. Although this difference is not dramatic, the effects on the inclusion capability of IRMOF-9 are easy to recognise: Methylene blue is able to enter in the channels and disperse in the solid, whereas Rhodamine 101 only remains adsorbed in the very external layers, thus confirming that the possible damages of the crystal does not affect significantly its effective porosity (Figure 1.3).
Concerning SCXRD analyses, IRMOF-9 pattern shows a rather low resolution when measured at room temperature. This is likely due to the non-crystalline fraction of the solid (the pores content), which scatters the X-rays incoherently.
The overall reciprocal space, evaluated by considering precession images calculated from the diffraction data (Figure 1.4), shows no remarkable sign of high mosaicity, as can be inferred from the outcomes of the soaking trials in the organic dyes solutions.
One very distinctive trait, which is clearly visible in the precession images, is the modulation of the Bragg intensities. Such a feature is not unusual in MOFs diffraction patterns, especially while dealing with interpenetrated networks. The reason lies in the presence and position of the SBUs and is due to the intensities scattered from their metal atoms. This aspect will be addressed in chapter III.

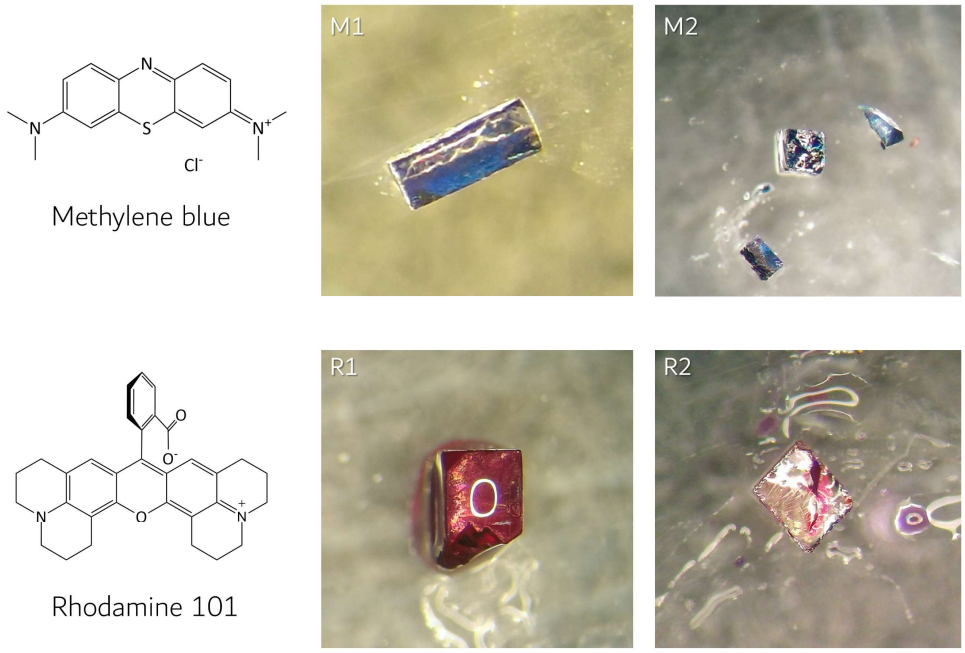

Figure 1.3. The dye molecules used for evaluating the defectiveness of IRMOF-9 and optical microscope pictures of the MOF after the soaking treatment (R1 and R2 for Rhodamine 101, M1 and M2 for Methylene blue). The external appearance of the treated crystals (B1, R1) and their cut sections (M2, R2) are shown separately.

As already mentioned in the Introduction, "MOFs structures" and "disorder" are two tightly bound concepts. IRMOF-9 constitutes no exception, even though its structural situation is more ordered than many others.

In this phase, there are two main disordered components: the solvent molecules and the linkers. Apart from the molecules inside the channels, the DMF trapped in the isolated cavities between the closest SBUs shows four equilibrium positions, where they weakly coordinate four different Zn atoms (bond distance 3.093(19)Å, Figure 1.5, a).

As for the linkers, the ones disposed along the channel axis are affected by a static disorder involving the phenyl rings (Figure 1.5, b).

This disorder is probably correlated to the site chosen by the disordered DMF. No static disorder is observed for the SBUs, and this agrees with the fact that the XRD pattern does not show a significant amount of diffuse scattering.

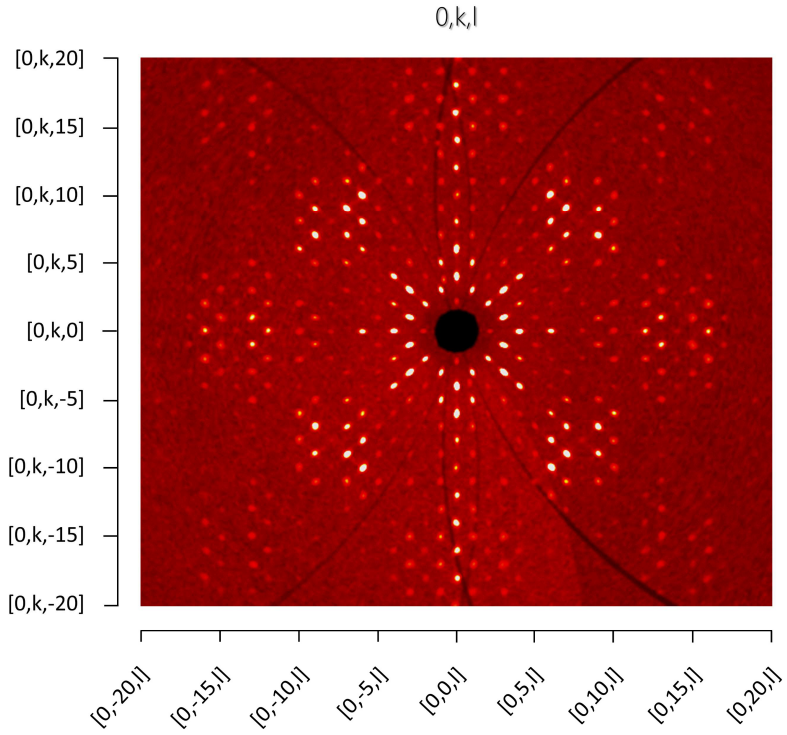

Figure 1.4. Image of the (0,k,l) plane of IRMOF-9 reciprocal space calculated from SCXRD images using the "Unwarp precession images" function of the CrysAlisPro software[57].

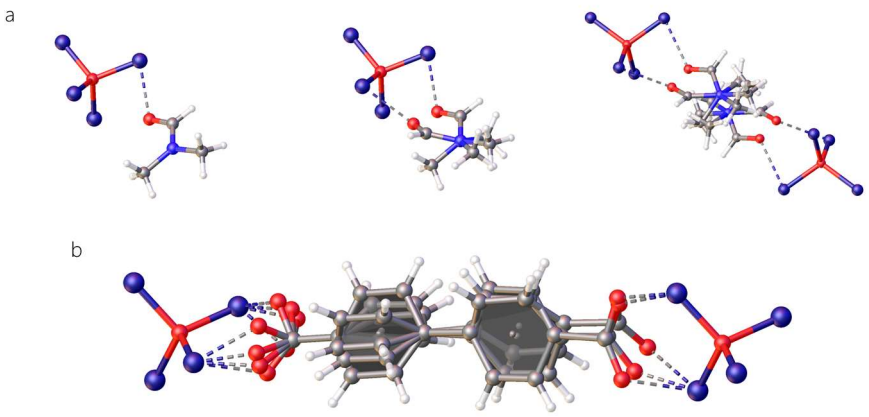

Figure 1.5. The two kinds of disorder in IRMOF-9 are displayed by using the Olex2 software[48]*. The positional disorder of the DMF molecule trapped between two SBUs is shown so that the four positions superimpose progressively from the left (a). Below, the disorder affecting the phenyl rings of the linkers disposed along the channel axis (b).*

1.2 · Peculiar behaviours

Since in the next chapters IRMOF-9 post-synthetic treatments will be described with special regard to its response to the external environment changes, some peculiar behaviours of this phase have been investigated.

1.2.1 · Stability at low temperature

The low temperature stability of IRMOF-9 has been evaluated. Hence, to have high resolution data, most of the SCXRD analyses have been carried out by using synchrotron radiation at 100K. The DSC profile recorded on IRMOF-9 crystals kept in a DMF droplet shows a broad and intense peak centred at 238K (DSC1, Appendix). This signal is observed both by lowering and raising the temperature around this point, thus confirming the reversibility of the transition.
SCXRD data have been collected at 100K, after a fast-freezing treatment in liquid nitrogen. The former single crystal is observed to be twinned in at least four recognizable domains, two dominant and two minor ones (Figure 1.6).

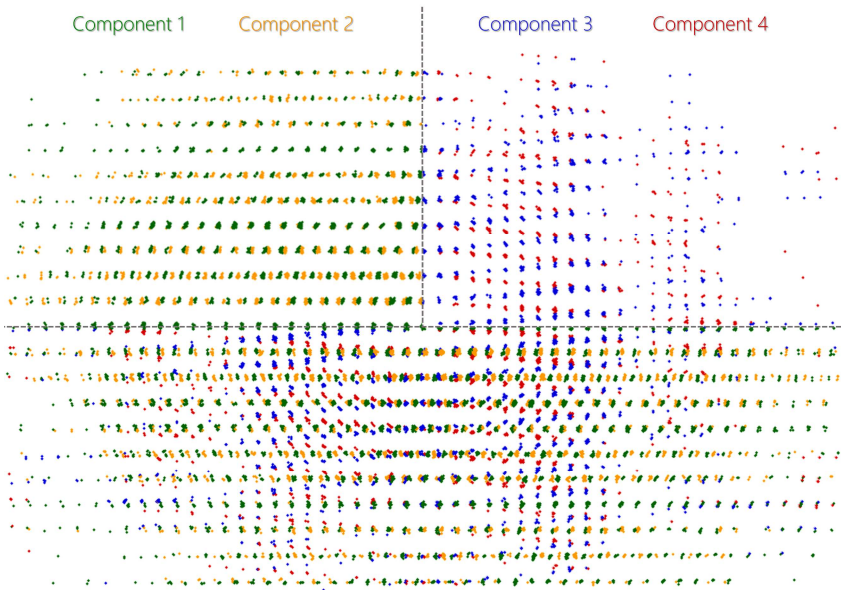

Figure 1.6. Reciprocal lattice of a former IRMOF-9 crystal after the fast-freezing at 100K, as shown by the "Ewald Explorer" function of the CrysAlisPro software[57]. The four domains are highlighted with different colours and separated in two pairs shown in the two upper quarters of the picture. The displayed view is along the b reciprocal direction, which is the same for every crystal domain.*

Consequently, the β angle changed from 90° to 95.149(4)°. Given the symmetry of the starting solid, this can occur towards the positive or the negative direction of *c*. For this reason, the final crystal shows two main domains related to each other by a rotation of ~ 180° about the *a* crystallographic axis. The causes of this dramatic change become clear after a first look at the IRMOF-9LT structure. Besides the difference in the linkers arrangement, the most notable change is the presence of two additional DMF molecules bound to the Zn atom, which points towards the channel centre (Figure 1.7).

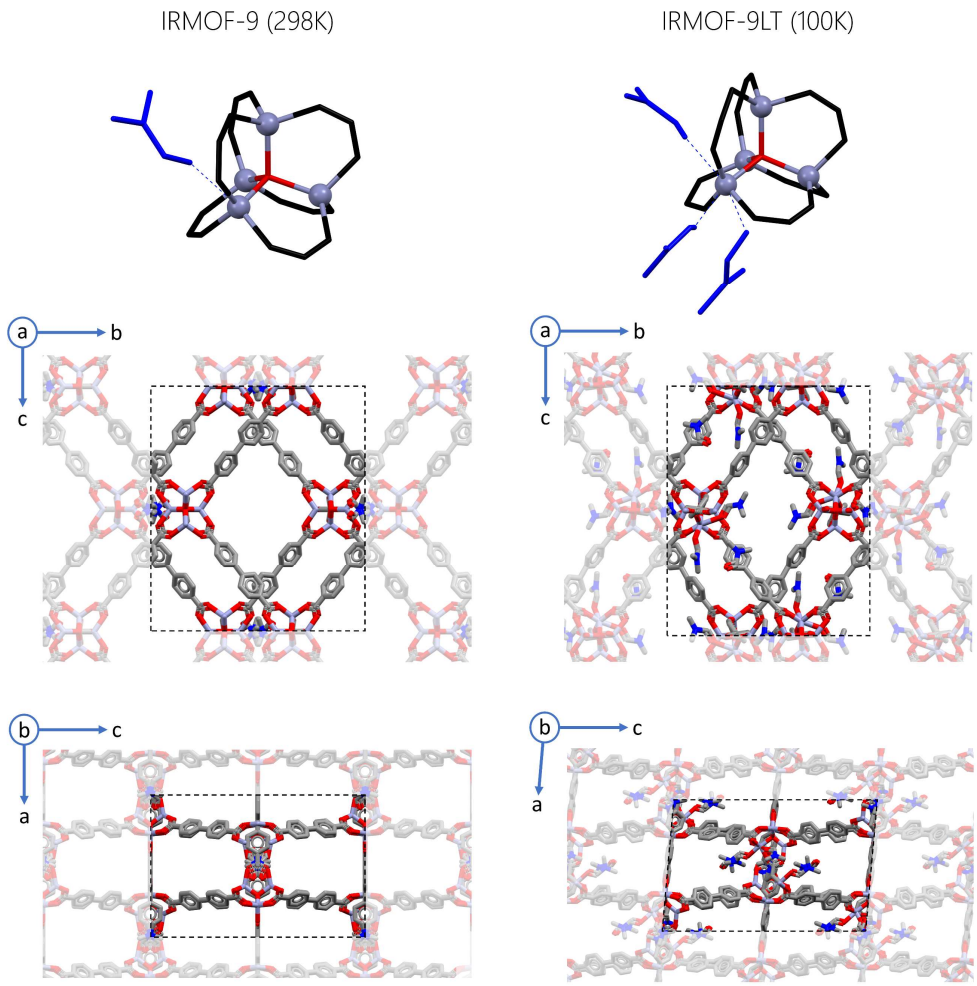

Figure 1.7. *Comparison between the IRMOF-9 and the IRMOF-9LT structures (left and right columns respectively). Above, the SBUs situation is represented highlighting the change of the coordinative environment in terms of number of DMF molecules (marked with a blue colour) bound to the involved Zn atom. Below, the unit cells are displayed along the a and b direction, highlighted with a dotted line.*

Two of these molecules coordinate the metal centre with bond distances 2.19(2) Å and 2.49(2) Å (Figure 1.7, upper right corner), and a third lies between the coordinated ones bridging them by means of H-bonds. The DMF present in the small cavity between the SBUs is still disordered in the same positions found in the IRMOF-9 structure (Figure 1.5).
The reason of the phase transition can be found in the competition between the lower energy of an ideal coordination geometry of the linkers around the SBUs and the energy gain resulting from an additional coordination of DMFs coming from the channels. Above 238K, thermal motions of these molecules in their disordered state prevents a stable coordination, which it may be present as fluxional. Once the temperature is lowered under this limit, the entropic contribution is not strong enough to avoid the stabilisation of the coordinative bond, and the framework adapts to the highly populated coordination sphere of the interested Zn atom.
It is important to mention that the chemical occupancy of these DMFs has been fixed to 0.5 to have a decent similarity between the Atomic Displacement Parameters (ADPs) of the solvent molecules and those of the linkers. However, since in a model refinement ADPs and occupancies correlate to each other and the data quality is low because of the phase transition, it is not sure whether the possibly higher ADPs of the DMFs are due to their real partial presence or to static/dynamic positional disorder.
To confirm the necessity of DMF for this phase transition, DSC analyses in the temperature range 223-263K were performed on IRMOF-9 after soaking in isopropanol for two weeks at room temperature. The thermal profile shows no distinguishable signal (DSC4, Appendix), thus confirming that the material, once DMF molecules are washed away by isopropanol, does not undergo any transition in the considered temperature range.

1.2.2 · Stability to solvents

IRMOF-9 is sensitive to environmental moisture and readily decompose within seconds if removed from DMF. This is a renowned weakness of Zn-based MOFs and causes a decrease of porosity and inevitable change in the structure composition[58]. This behaviour has been proven to be enhanced in cases of interpenetrated MOFs[59].
Solvent exchange is another aspect that should be considered carefully. The exchange of DMF with dichloromethane (DCM) and acetone has been observed to have negative effects on the quality of the crystals, and resulted in a collapse of the framework. In both cases, although the solid remained crystalline, the structure solution was not possible since the crystals were very damaged and the exposure to synchrotron radiation caused a fast amorphisation, thus preventing the attainment of structural information. Only in the case of DCM, one specimen survived long enough to provide reflections for the indexing of its

unit cell. This can be considered the deformation of the starting one due to the voids shrinking (table 1.1, graph 1.1). The volume, which amounts to 7117.2(9) $Å^3$, is dramatically lower with respect to the starting one (9988(3) $Å^3$ at 298K) and suggests that the overall effect of DCM towards IRMOF-9 is to wash away the inner DMF without replacing it, yielding a collapsed framework which is probably not porous anymore. A completely different behaviour is observed after soaking IRMOF-9 in isopropanol (iPrOH). The crystals are stable and do not show any remarkable decrease of crystallinity even after 1 month. Data collected with laboratory source at room temperature showed no remarkable change in the cell parameter and in the symmetry of the solid.

	IRMOF-9 in DMF (298K)	IRMOF-9 in iPrOH (100K)	IRMOF-9 in DMF (100K)	IRMOF-9 in DCM (100K)
a (Å)	17.134(3)	17.1852(2)	17.1224(9)	14.337(4)
b (Å)	22.456(5)	22.0643(4)	21.412(2)	17.2881(10)
c (Å)	25.957(5)	26.1140(3)	26.6098(11)	28.7152(15)
α (°)	90	90.7490(10)	90	89.971(5)
β (°)	90	90	95.149(4)	89.964(6)
γ (°)	90	90	90	90.154(6)
V ($Å^3$)	9988(3)	9901.0(2)	9716.6(13)	7117.2(9)

Table 1.1. *Cell parameters and volumes of IRMOF-9 at room temperature and of IRMOF-9 at 100K after soaking in DMF, iPrOH and DCM. In the case of iPrOH, the standard crystallographic axes assignment has been changed to facilitate the comparison with the original cell parameters. The cell axes are highlighted with different colours accordingly with graph 1.1.*

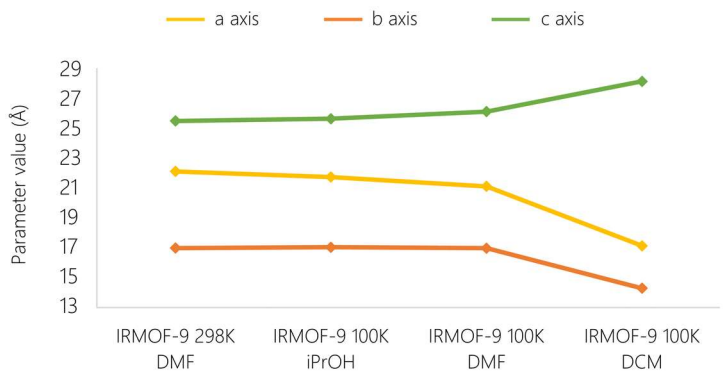

Graph 1.1. *Cell parameters trend in IRMOF-9 from native crystals to the differently solvated forms at 100K (DMF, iPrOH and DCM); the plotted data is taken from table 1.1. The clear correlation between the increase of the c axis and the decrease of the remaining a and b axes is consistent with a deformation of the unit cell.*

Synchrotron SCXRD data collected at 100K confirmed the absence of structural DMF, as well as the presence of iPrOH in the framework (Figure 1.8). As in the case of IRMOF-9LT, the phase is found to be twinned, the two domains are related by ~180° rotation about the *a* axis, and the space group changed from Pnnm to $P2_1/n$.

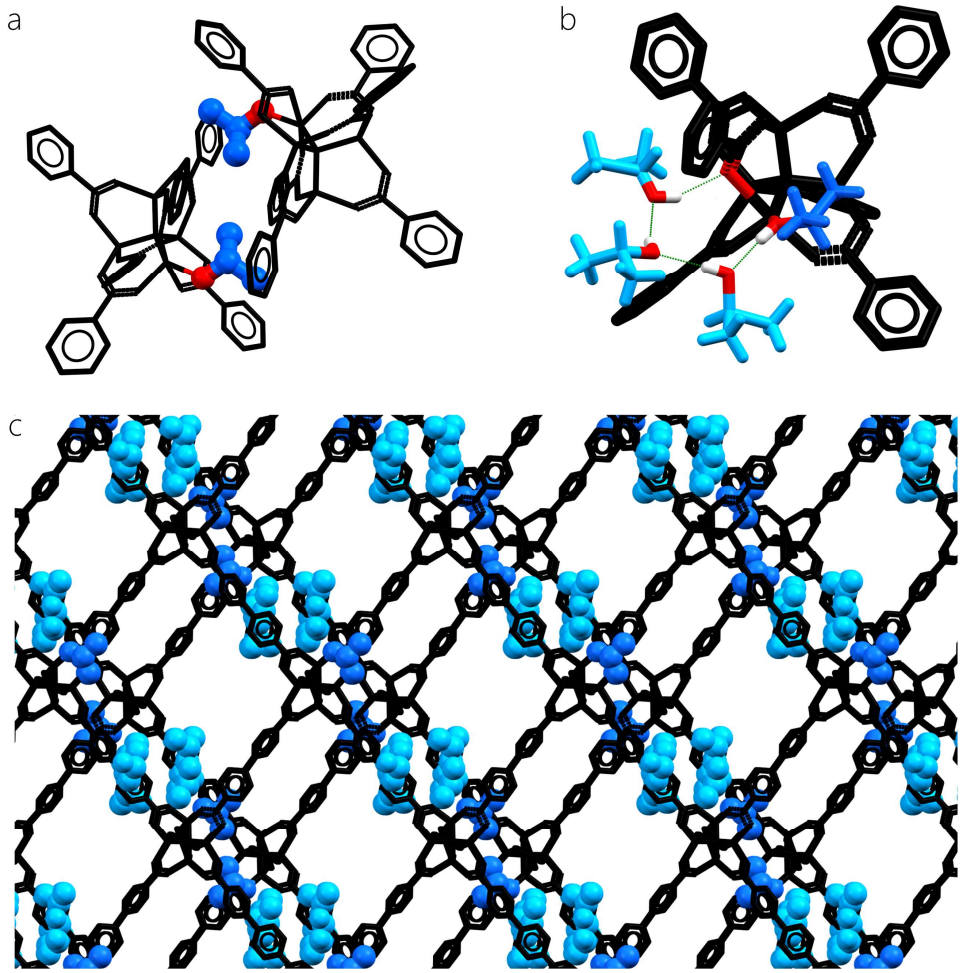

Figure 1.8. Some distinctive features of IRMOF-9 structure after soaking in iPrOH (data collected at 100K). Above, the peculiar situation of the SBUs: an isopropanol molecules is stably coordinated toone Zn for each SBU (a), pointing the alkyl groups towards the cavity formed by the two adjacent SBUs of the two interpenetrated networks. The three other ordered iPrOH molecules are involved, together with the coordinated one, in a head-to-tail H bond, which ends with a hydrogen donation to an oxygen atom of a linker carboxylate group (b). The overall framework viewed along the channels axes (c), shows the presence of this iPrOH ring pointing towards the centre of the cavity, while the Pmm symmetry present in the starting solid in this direction is broken by the misalignment of the SBU pairs.

This symmetry break brought the β angle value to 90.7490(10)°, as a result of the incline of the *a* axis. In this case, however, the deformation does not involve the coordination geometry of the linker molecules, but rather the movement of the two lattices of the framework (Figure 1.8, c).

This is due to the coordination of isopropanol molecules on specific Zn centres, right where the linkers perform their embrace-like contact. Since aliphatic groups of the solvent points toward the SBU of the adjacent network, lowering the temperature forces the two nets to adapt to the resulting bulk, thus breaking the Pmm symmetry present in the native IRMOF-9 along the *a* direction. The coordinated isopropanol is involved in a 4-molecules OH···O head-to-tail hydrogen bonds starting from its oxygen atom and ending on another one belonging to a linker carboxylate group. Remarkably, no DMF molecule is present in the small cavity between the closest SBUs. Therefore, the two interpenetrated lattices might be able to move and possibly open this void at room temperature. This allowed the DMF to be washed away and replaced by the isopropanol, yielding a penta-coordinated Zn.

1.2.2.1 · Zn-BPDC stable phases in aqueous solution

Given the strong instability of IRMOF-9 in humid environments, the reaction between Zn and BPDC in aqueous solution has been carried out to observe the stable phases. Aiming to use water-soluble reactants, the sodium salt of BPDC has been used. This makes the molecule obviously more reactive towards the Zn^{2+} ions and a direct mixing of the two reagents (Na_2BPDC and $Zn(NO_3)_2$) would result in a massive precipitation. For this reason, a gel medium was used to avoid convective motions and diffusive layer effects, and to slow down the reaction of the two reagents, therefore decreasing the local supersaturation rate[60,61].

The synthetic strategy has been the counter-diffusion of the two reactant aqueous solutions in a water containing agarose gel (paragraph A.1.3, Appendix). The experiments were carried out in a "U" tube containing the gel in its horizontal section, and the two solutions in the vertical extremities (Figure A.1.1, Appendix). Overall, the syntheses afforded two phases appearing as parallelogramic and rectangular platelets (Figure 1.9), namely ZnBPDC1 and ZnBPDC2, both with composition $Zn(BPDC)\cdot 3H_2O$.

Remarkably, these are found to grow in the same regions of the gel and sometimes intergrown with each other, thus constituting a remarkable case of concomitant polymorphism[62].

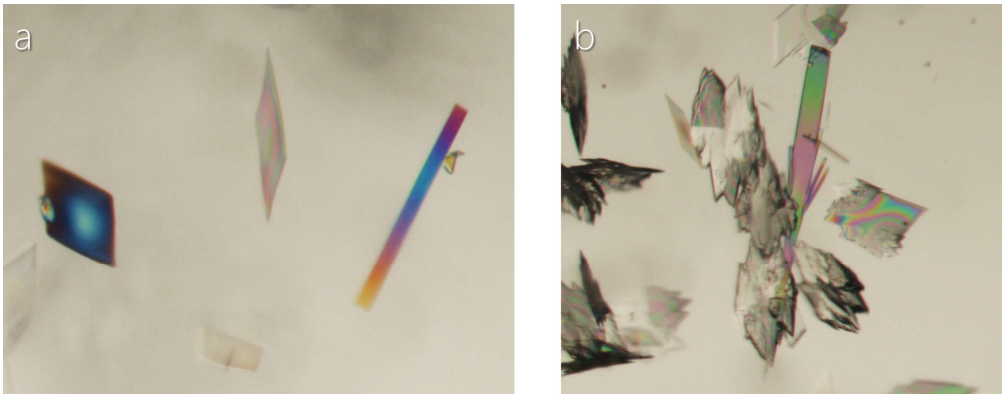

Figure 1.9. *Optical microscope images of the two polymorphs grown suspended in the gel (a), sometimes present as intergrown phases (b); the colours are due to the polarisation of the light.*

ZnBPDC1 structure has already been reported (CCDC 800389[55]) by Tao et al[63], whereas ZnBPDC2 one is unprecedented and isostructural with an already known Ca-based analogue (CCDC 682688[55]). Regarding the structures, the main difference lies in their coordinative environment. In ZnBPDC1 the metal has an octahedral coordination geometry (Figure 1.10, a), accepting coordination from two BPDC ions and four water molecules, the latter bridging different metal centres (Figure 1.11). In the case of ZnBPDC2, the metal centre is hepta-coordinated (Figure 1.10, b), since the carboxylate group binds three metal centres (Figure 1.12).

Also in ZnBPDC2 water molecules are shared between different metals. As a result, both structures consist of a close packing of 1D chains formed by Zn atoms, which are held together by means of water and BPDC molecules. Remarkably, the latter behave like monotopic ligands, being one of the two carboxylate groups always involved in hydrogen bonds with water molecules without contacting the metal.
The XRPD pattern of IRMOF-9 crystals after the exposure to air moisture shows peaks attributable to both phases (XRPD1, Appendix). Their simultaneous formation in the degradation process agrees with their proven analogue kinetical stability.

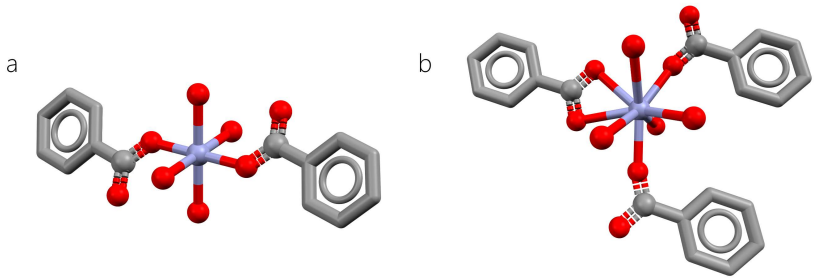

Figure 1.10. Coordination sphere of the Zn atoms in ZnBPDC1 (a) and ZnBPDC2 (b). Hydrogen atoms are omitted and only the involved halves of BPDC molecules are shown for the sake of clarity.

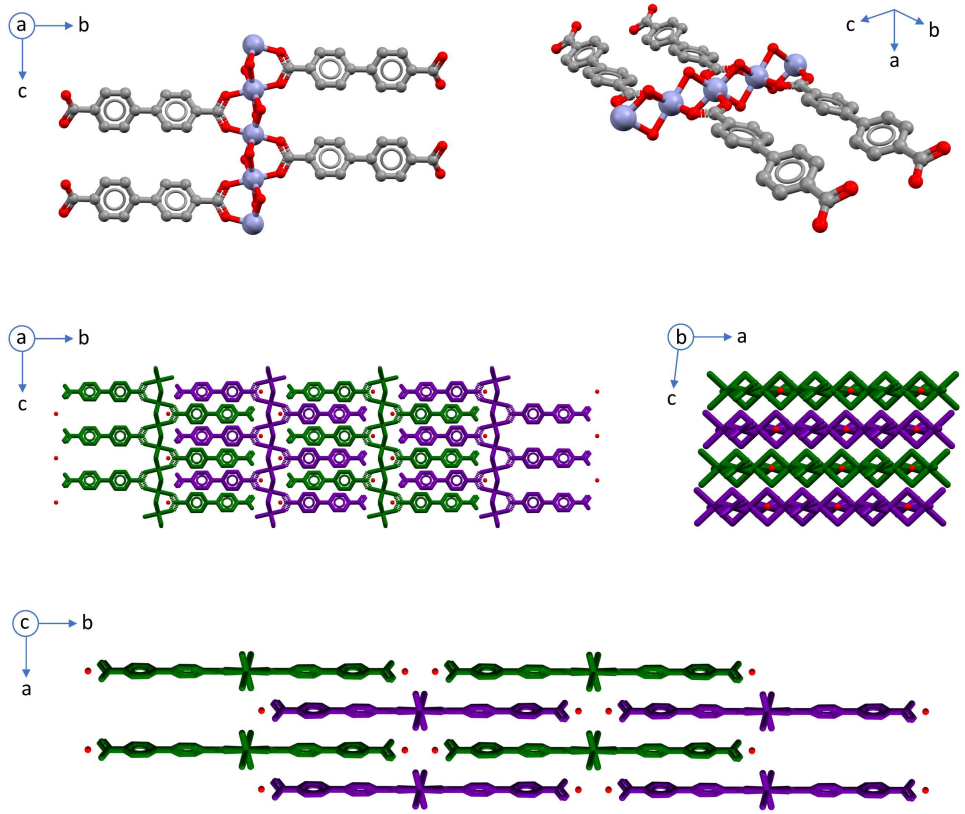

Figure 1.11. The structural features of ZnBPDC1 are displayed; hydrogen atoms are omitted for the sake of clarity. Above, a fraction of the 1D chain is showed from two different points of view. Below, the packing of different chains is shown along the three crystallographic directions. The layer alternation is highlighted by changing the colour from one layer to the adjacent one (oxygen atoms belonging to uncoordinated water molecules are marked in red.

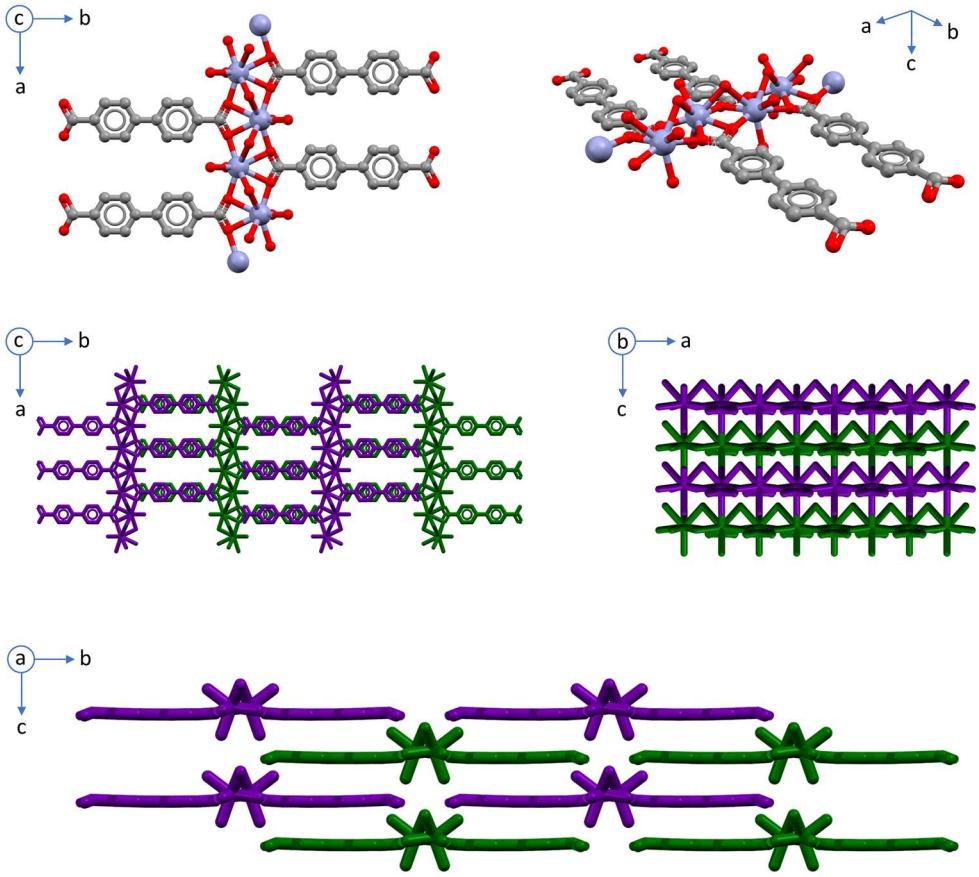

Figure 1.12. The structural features of ZnBPDC2 are displayed; hydrogen atoms are omitted for the sake of clarity. Above, a fraction of the 1D chain is showed from two different points of view. Below, the packing of different chains is shown along the three crystallographic directions; The layer alternation is highlighted by changing the colour from one layer to the adjacent one.

1.3 · Concluding remarks

IRMOF-9 structure has proven to be flexible and versatile. According to the experimental data and its interpretation, this flexibility involves three different degrees of freedom held by the overall framework.

First, the rhombic disposition of the SBU-linkers arrangement is capable of deforming by shortening the distance between the SBU pairs along the *b* direction. This results in a "breathing" movement of the framework[64], thus reducing the unit cell volume and, as a consequence, the hollow fraction of the solid.

The occurrence of such a behaviour can be related to the type of solvent present in the cavities. If able to substitute the linkers in the coordination sphere of the metals, the solid disintegrates and transforms in a totally different phase. This is what has been observed when IRMOF-9 is exposed to moisture or soaked in water.

A study by Liu et al[59] analysed this case in particular and proposed a mechanism based on Molecular Dynamics simulations, which revealed a water-assisted linker detachment from the SBU by means of hydrolysis with formation of protonated BPDC molecules, and coordination of hydroxyl groups to the Zn centres.

If the solvent does not substitute the linkers, but it is capable to enter in the coordination sphere causing steric hindrance, the system responds by deforming the linkers disposition around the SBUs. This leads to a distortion of the overall framework and, potentially, to a symmetry decrease, as observed in the case of isopropanol.

A different behaviour is observed in the case of DCM and acetone, whose presence causes a collapse of the framework. Given the negligible coordinative properties of these two solvents, what has been observed might be related to a probable structural role of the solvent dynamic coordination around the SBUs. In the case of DMF and iPrOH, their fluxional coordination creates a hindrance on the SBUs and limit the linkers movements, which can allow the solid to collapse. On the other hand, when a poorly coordinative solvent is introduced in the framework, the mentioned hindrance is not present and the cavities are free to deform and minimise the voids.

The second structural degree of freedom held by IRMOF-9 is the capability of moving the two interpenetrated networks, allowing the opening of the small cavity formed by the SBU closest pairs. Although not always observed, this behaviour emerged after exchanging the solvent with iPrOH and lowering the temperature to 100K. This highlighted the possibility that the two networks are capable to slide one on the other if any physical reason emerges.

Lastly, another source of structural flexibility is the capability to accept additional stable coordinative bonds to the metal centres without altering the overall linker-SBU topology. This behaviour highlights the possibility to permanently increase the coordination number on the metal centres, i.e., a functionalisation of the framework on the SBUs.

Chapter II

Zn-to-Co transmetalation

"Pleasure to me is wonder.
The unexplored,
the unexpected,
the thing that is hidden and the changeless thing
that lurks behind superficial mutability."

H. P. Lovecraft

"Collected Essays, Volume 5: Philosophy"
1921

2.1 · General issues in transmetalation

Among all Post-Synthetic Modifications, transmetalations are maybe the easiest to perform (Figure 2.1). The general procedure usually consists, for a certain MOF, in the choice of a solvent where it is stable and of a metal whose coordination geometry is analogue to that of the starting framework metals. Once appropriate candidates are chosen, the MOF is soaked for a certain time span in a solution containing a salt of the selected metal in an arbitrary concentration; all these variables obviously need to be optimised for each case.
At this point, the only thing to do is to analyse the trend of the cation exchange during soaking time, and eventually characterise the material thus obtained. This easiness comes with obvious drawbacks, above all the inability to use whichever metal is needed to exchange in the framework, and that the yield is usually unavoidably lower than 100% [65–67].

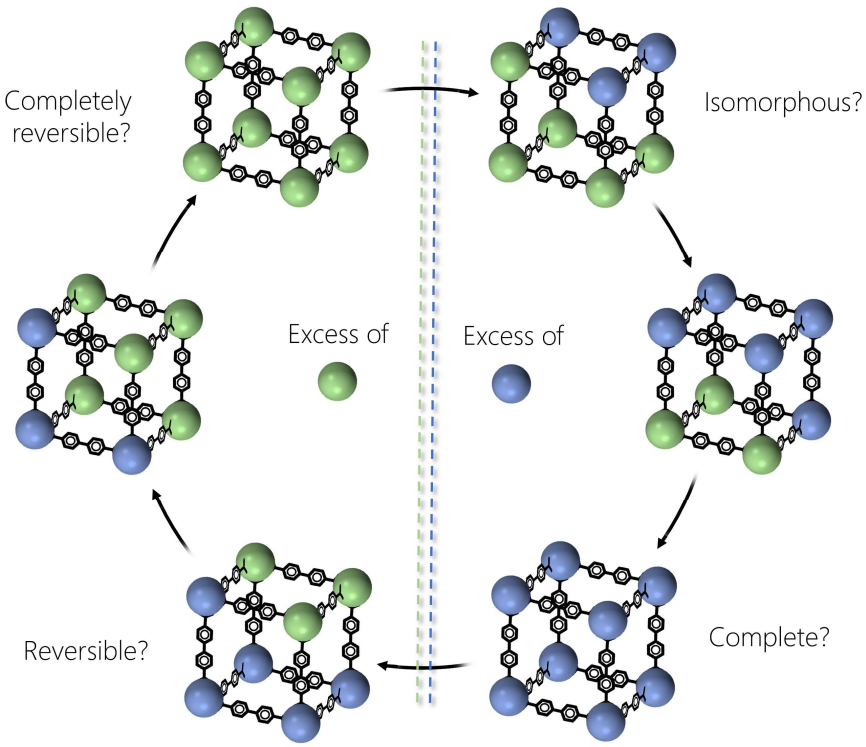

Figure 2.1. Graphical simplification of the transmetalation process and its performance possibilities.

In case one of the main purposes is the accurate structural characterisation of the final MOF, this could constitute a real problem since it produces disorder in the material and this would negatively affect its diffraction pattern.

Indeed, in the probable cases in which the distribution of the metal substitutions is not prevalently ordered inside the solid, this would cause a strong diffuse scattering in the XRD pattern and the structure solution and refinement could become all but straightforward.

In even more unlucky cases, the framework may not be able to endure the necessary structural changes in the SBU and the crystal might face a dramatic drop of crystallinity[68] or even amorphisation[69].

In this respect, Zn-to-Co transmetalations have been described as particularly efficient in preserving the MOF original architecture without damaging the solid[70]. Moreover, especially this type of PSM is observed to enhance gas adsorption properties of the material for H_2, CH_4 and CO_2 [46]. When the general phenomenon is studied, the mostly used material is MOF-5 (paragraph 0.1.2.1, Introduction) because of its simple and cheap synthesis, the quality of the crystals, and because it is unanimously considered as the "forefather" of all the Zn_4O based frameworks.

One of the structural close relatives of MOF-5 is IRMOF-9 and this is the reason why the work regarding the transmetalation of this MOF focused on the Zn-to-Co cation exchange in which, judging by the results, the "new generations" show promising improvements.

2.2 · Transformation of IRMOF-9 into Co-IRMOF-9

The transmetalation procedure consisted in the soaking of IRMOF-9 in a high concentration $CoCl_2$ DMF solution for one month (paragraph A.1.4, Appendix). After 7 days of soaking, the crystals exhibited an intense blue colour. This colour is observed to follow the habit of the solids, proceeding progressively towards its inner part (Figure 2.2). Remarkably, the colour was maintained after having left some specimens in pure DMF for 7 days at room temperature. This suggested that the colour change was not due to the trapping of Co^{2+} and Cl^- ions inside the MOF pores, but to a structural change of the framework itself.

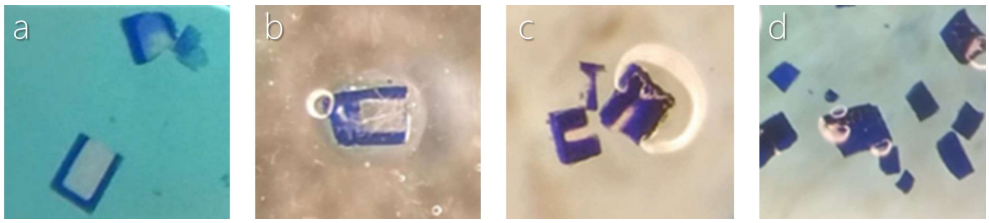

Figure 2.2. Optical Microscope images of IRMOF-9 crystals at different transmetalation stages. The crystals were cut in order to expose the internal section. The picture on the very left was taken after 1 week of soaking, and the subsequent ones progressively every 7 days.

Morphological and elementary composition analyses were performed by Environmental Scanning Electron Microscopy (ESEM) on crystals after 3 weeks of soaking treatment (Figure 2.3). For these analyses, some specimens have been chosen, cut in half, and their section has been exposed to the electron beam. EDX measurements provided qualitative information on the presence of Zn and/or Co in the solid.

The composition of the solid in terms of Zn:Co ratio flips while going from the surface towards its centre. Overall, the outer layers show a negligible amount of Zn, which is found mainly in the core, where the presence of Co is detectable as well (EDX1, Appendix).

It is important to remember that crystals of various sizes in the same soaking solution are likely to exchange a different percentage of their cations after a fixed amount of time because of the differences in their area-to-volume ratios. For this reason, crystals at different stages of transmetalation might be present in a single soaking batch.

By considering the morphology of the solid, the completely transmetalated part is remarkably less damaged with respect to the central one, which does not look belonging to the same crystalline domain (Figure 2.4).

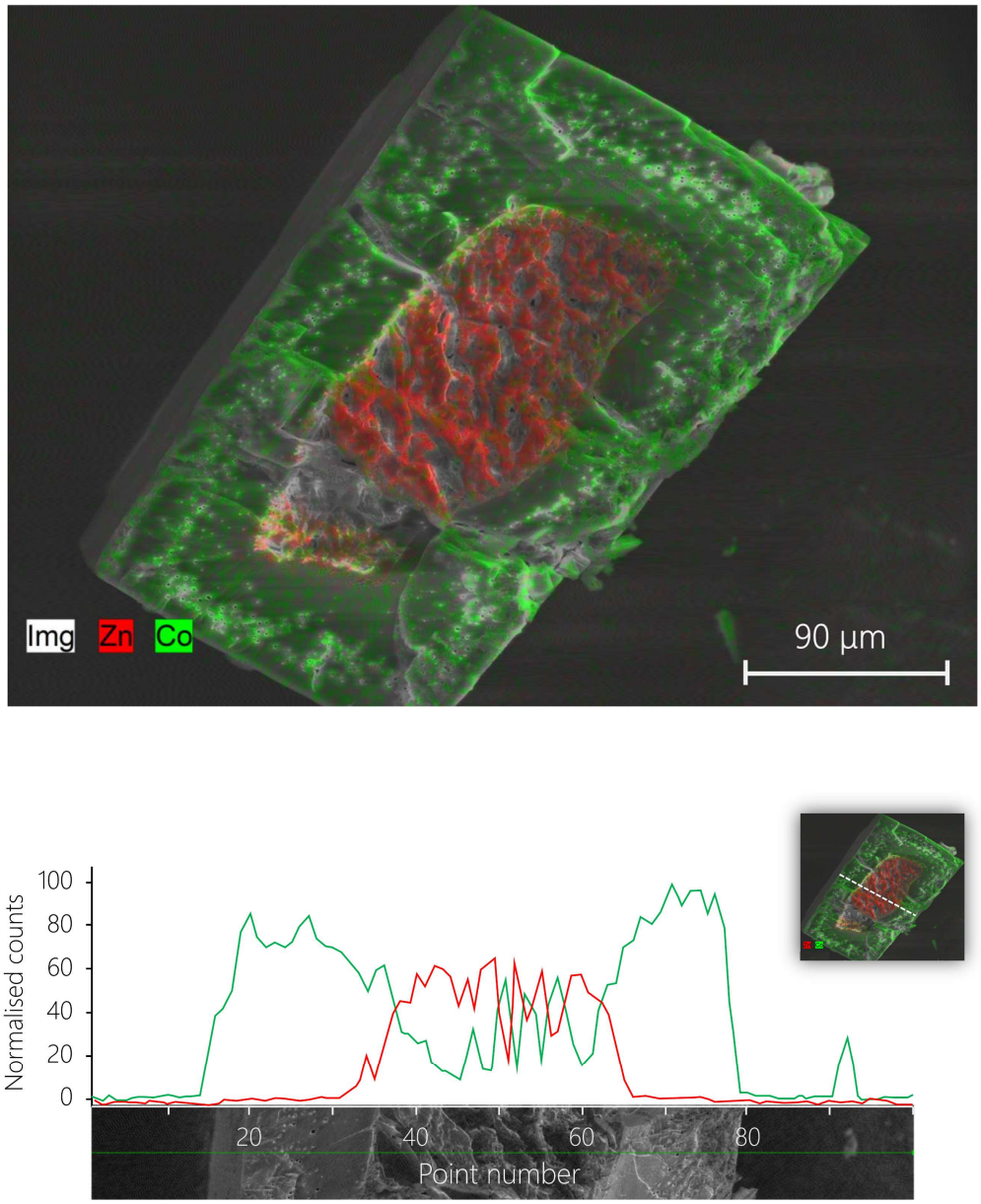

Figure 2.3. ESEM/EDX analysis of a partially transmetalated IRMOF-9 crystal; the presence of Zn and Co metal centres is displayed with a red and a green colour respectively. The crystal has been cut in order to expose its section to the electron beam. Above, the overall metal composition map; below, a linear scan of the composition performed in the middle of the section parallel to the smaller sides.

Moreover, several holes with a shape resembling the typical crystal habit of the solid are clearly visible in the transmetalated part, decreasing in size while going from the crystal surface inwards (Figure 2.4-2.5).
Both these evidences could suggest that the transformation does not proceed by exchanging metal by metal in the SBUs, but rather by a demolition-reconstruction of the crystal phase. In this case, the observed µm-sized holes might be due to interruptions during the new phase growth. Their presence is concentrated in the outer regions of the solid and their bigger size is due to the faster transformation occurring near the surface, thus causing growth defects during the new phase formation.

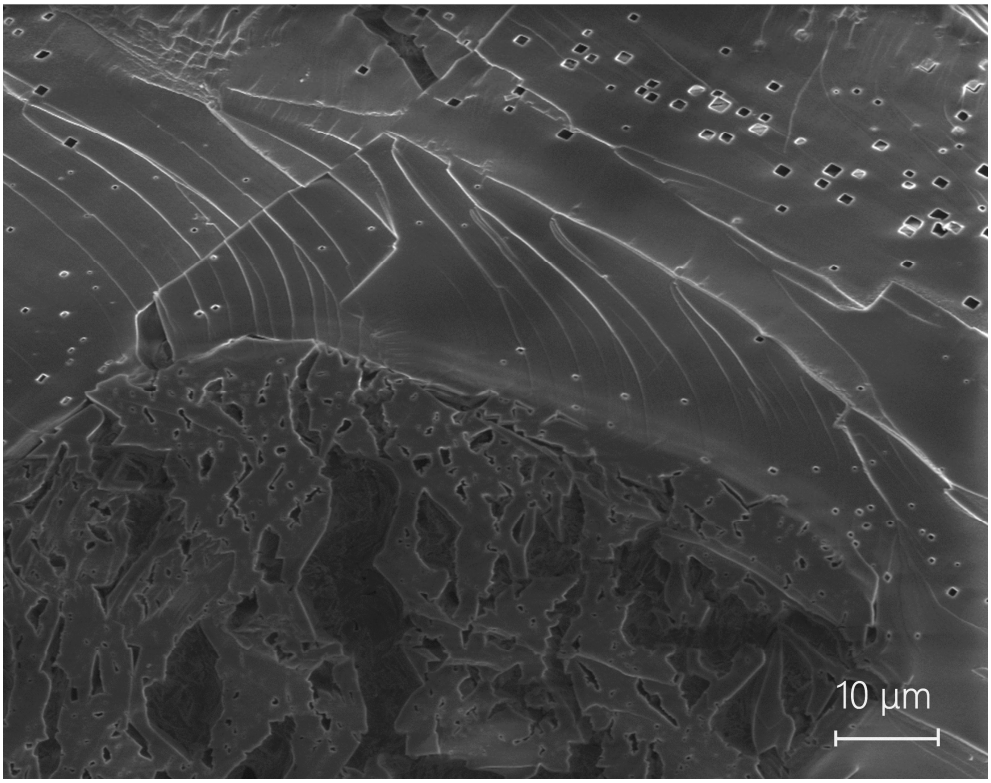

Figure 2.4. ESEM image magnification of the crystal shown in picture 2.3, where the Zn- and the Co-rich parts are recognisable. Remarkably, the transmetalated part (upper part of the picture) shows a more homogeneous morphology, together with the presence of holes resembling the crystal habit.

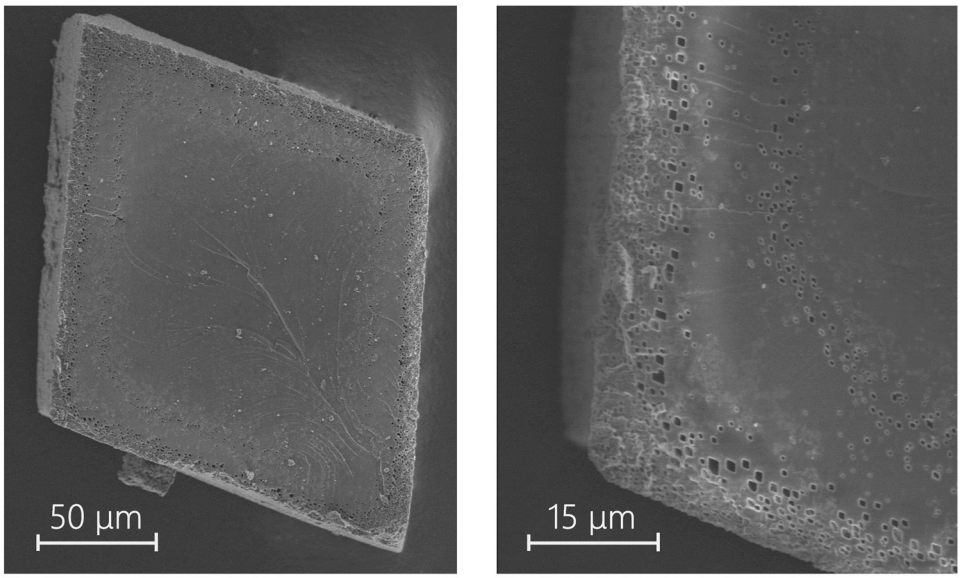

Figure 2.5. ESEM images of the external surface of a partially transmetalated IRMOF-9 crystal. On the right, a magnification highlights the presence of holes decreasing in size while proceeding towards the solid centre.

Aiming to observe the trend of the metal exchange, ICP-OES analyses were performed on samples taken at different soaking times. For this experiment, the soaking temperature of the analysed batch was set to 305K to speed up the cation exchange and shorten the time required for transformation to reach completeness. The resulting data shows that the process significantly decreases in speed during time, resulting in a pseudo-logarithmic curve of the Co:Zn compositional ratio (paragraph A.8.1, Appendix).
This is coherent with the fact that the Co cations readily exchange with the Zn ones in the superficial layers of the crystal. The deeper the transformation goes, the slower it becomes due to the limited diffusion rate in the inner regions.
Further analyses performed on crystals of completely transmetalated crystals (Co-IRMOF-9) left in a DMF solution containing $ZnCl_2$ confirmed the cation exchange reversibility. However, in the latter case the process does not reach completeness after 30 days of soaking, yielding a Zn:Co ratio of ~5.8. This difference can be attributed to the higher lability of Zn^{2+} cation with respect to Co^{2+}. Given the d^7 configuration of the latter, the crystal field energy stabilisation is theoretically more favourable to a stable coordination.

Crystals of Co-IRMOF-9 were transferred into a capillary containing pure DMF, and their XRPD pattern was recorded (paragraph A.2.4, Appendix). The same was done with IRMOF-9, to allow a comparison between the two phases. While the two patterns clearly belong to two isostructural phases, slight differences in the peaks position are consistent with subtle changes in the cell parameters due to the transformation (Figure 2.6).
DSC profile of Co-IRMOF-9 was recorded to verify the possible occurrence of a phase transition similarly to the one observed for IRMOF-9 (paragraph 1.4.1, Chapter I). Indeed, also this phase thermal profile shows an analogue signal, but centred at 181.25K (compared to 237.97K for IRMOF-9; DSC2, Appendix). Evidently, the coordination of additional DMF molecules to the Co_4O SBUs is much less stabilising compared to the case of Zn_4O.

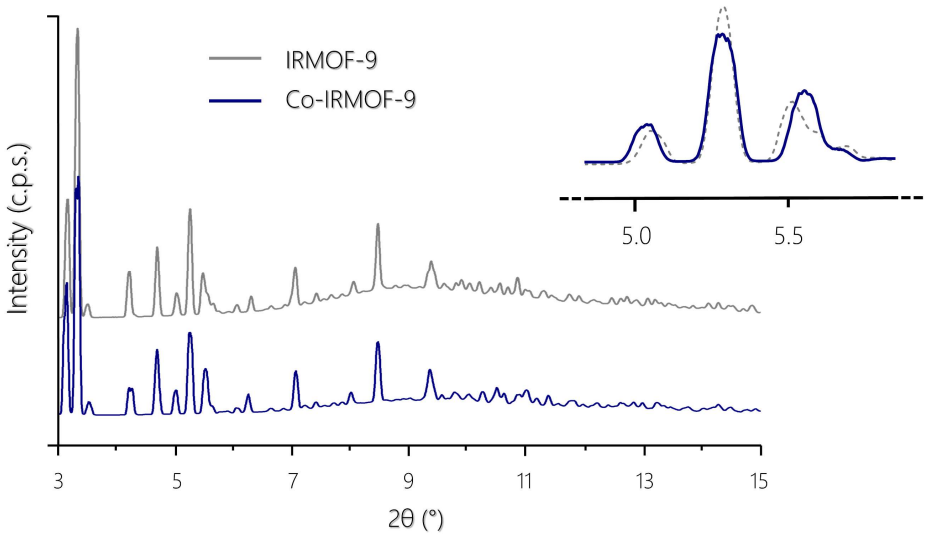

Figure 2.6. Superimposed XRPD patterns of the IRMOF-9 and Co-IRMOF-9 phases (information regarding the data acquisition and processing can be found in paragraph A.2.4, Appendix).

2.3 · Co-IRMOF-9 structure

Since the crystals apparently retained the original crystal habit after the complete cation exchange, SCXRD analyses have been performed, thus confirming the single-crystal-to-single-crystal character of the transformation. The data were collected with synchrotron radiation at 258K to avoid the low temperature phase transition and to allow a comparison with the IRMOF-9 structure present in the literature (CCDC 175580[55]), the latter being collected at this temperature condition. In the following discussion, the structural features of IRMOF-9 are taken from the data published by Eddaoudi et al[53].

The unit cell parameters deviate slightly from those of IRMOF-9, and the framework arrangement is identical, although some differences in the SBU coordination geometry are present. Concerning the M_4O SBUs (M=Co/Zn), the O-metal bond distances are roughly similar, since they range from 1.929 to 1.950 Å in IRMOF-9, and from 1.918(4) to 1.970(4) Å in Co-IRMOF-9. The most recognisable difference involves the geometry of the linkers disposition around the SBUs. To be accurate, not all the linkers are oriented differently if compared to the Zn-based phase, but only those who are not involved in the embrace-like interaction.

By observing the superimposition of two symmetry-equivalent SBUs (Figure 2.7), it is indeed recognisable a more open disposition of these three linkers in the case of Co-IMROF-9 (Figure 2.7, b). This distortion causes an elongation of the *c* axis, together with the shortening of the *b* axis of the unit cell. The consequence on the arrangement of the SBUs is an increase of the distance between SBU pairs, but not between SBUs belonging to the same pair (Figure 2.8).

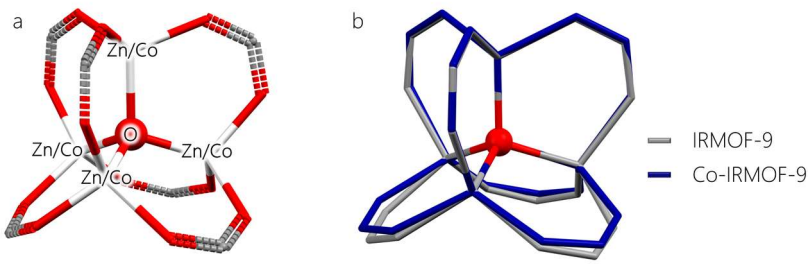

Figure 2.7. Comparison between IRMOF-9 and Co-IRMOF-9 SBU coordination geometries. The general SBU coordination geometry is represented on the upper right corner (a). Aside, the two structural situations are superimposed (b) to highlight the differences in the coordination geometry of three carboxylate pointing towards the channel (the lower ones in the picture).

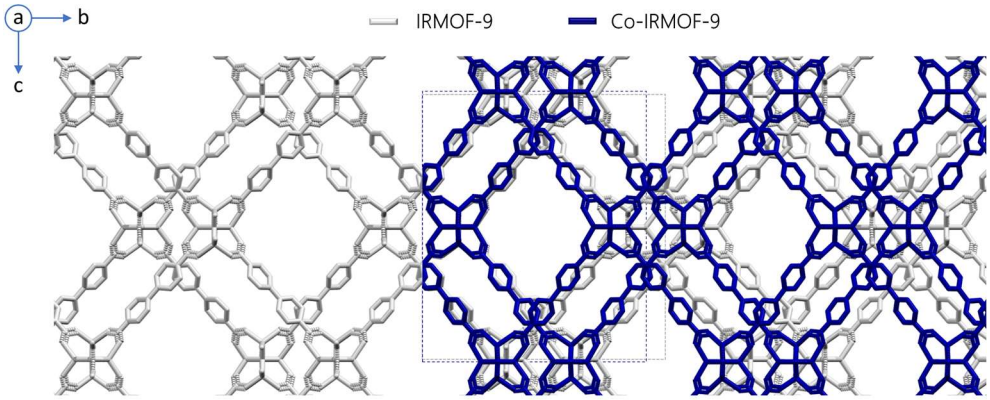

Figure 2.8. Comparison between IRMOF-9 and Co-IRMOF-9 structures at 258K. The two lattices are compared by superimposition to highlight the differences in the SBU coordination geometry and the deformation of the unit cell. The cell dimensions are reported in a blue and a dotted black line for IRMOF-9 and Co-IRMOF-9 respectively.

The average structure analysis shows a peculiar situation, being the linker molecules disordered in two different manners. Along the channel direction (parallel to the *a* axis), the phenyl rings of BPDCs are disordered by rotating about the molecule axis, whereas the linkers constituting the "walls" of the channel exhibit a positional disorder along the *b*+*c* and *b*-*c* crystallographic directions (Figure 2.9-2.10). This evidence agrees with the SBU distortion described above, even though it does not provide any direct information regarding the reasons of this distortion. No static disorder affecting the metals in the SBU is observed.

Overall, the reciprocal space of the solid shows clear sign of mosaicity increase, since the Bragg reflections are elongated in a concentric manner around the origin of the reciprocal space. This is observed mainly in the (0,k,l) plane and therefore affects the *a** direction of the reciprocal space, which corresponds to the *a* direction of the crystalline domain. The peak shape suggests that this loss of crystallinity led to the formation of four major domains slightly displaced with each other (Figure 2.11).

A low but distinguishable amount of diffuse scattering is present very close to the Bragg peaks, smearing them out in the *b** and *c** direction. This is linked to a disorder in the *b* and *c* direction of the crystal and can relate to missing-metal defects which most affects the *bc* plane where the framework is more flexible.

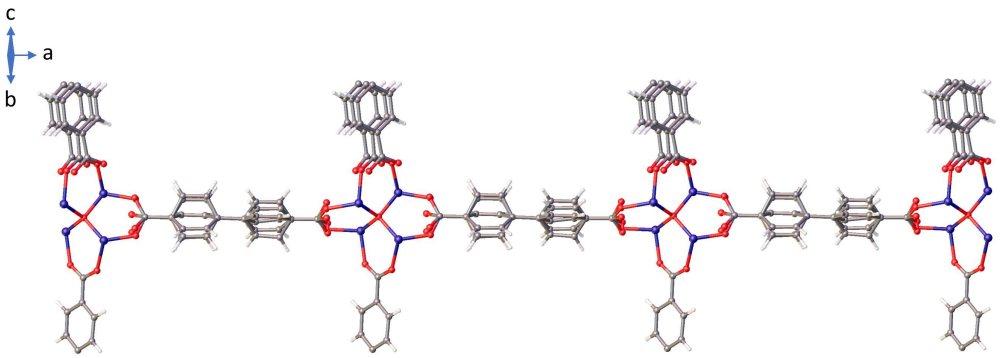

Figure 2.9. A chain belonging to a single network is shown along the b axis, highlighting the two disorder types affecting the linker molecules in Co-IRMOF-9.

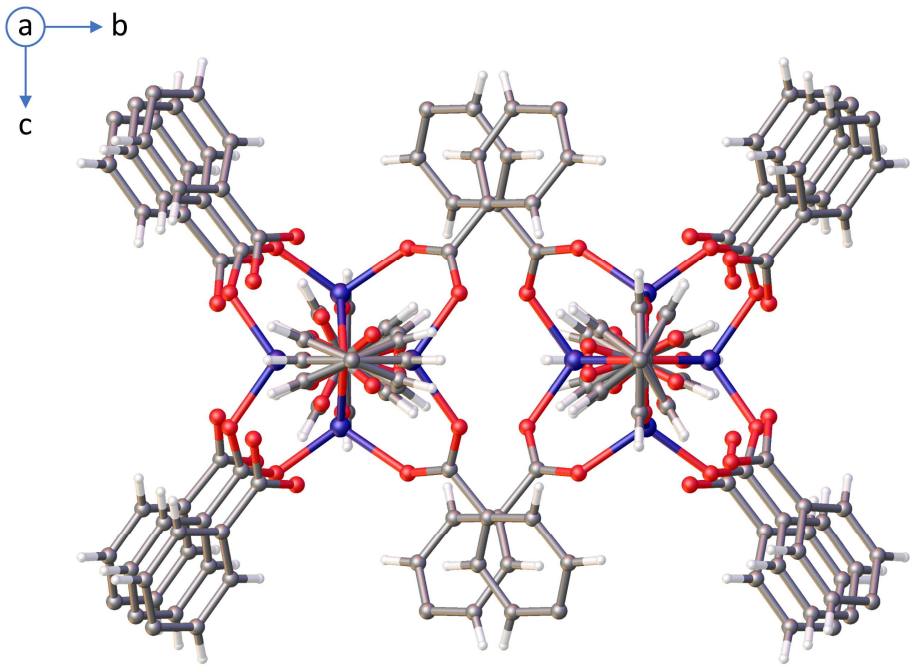

Figure 2.10. The main features of the two disorder types involving the linker molecules in Co-IRMOF-9 are displayed by showing a SBU pair of the interpenetrated lattice along the a axis.

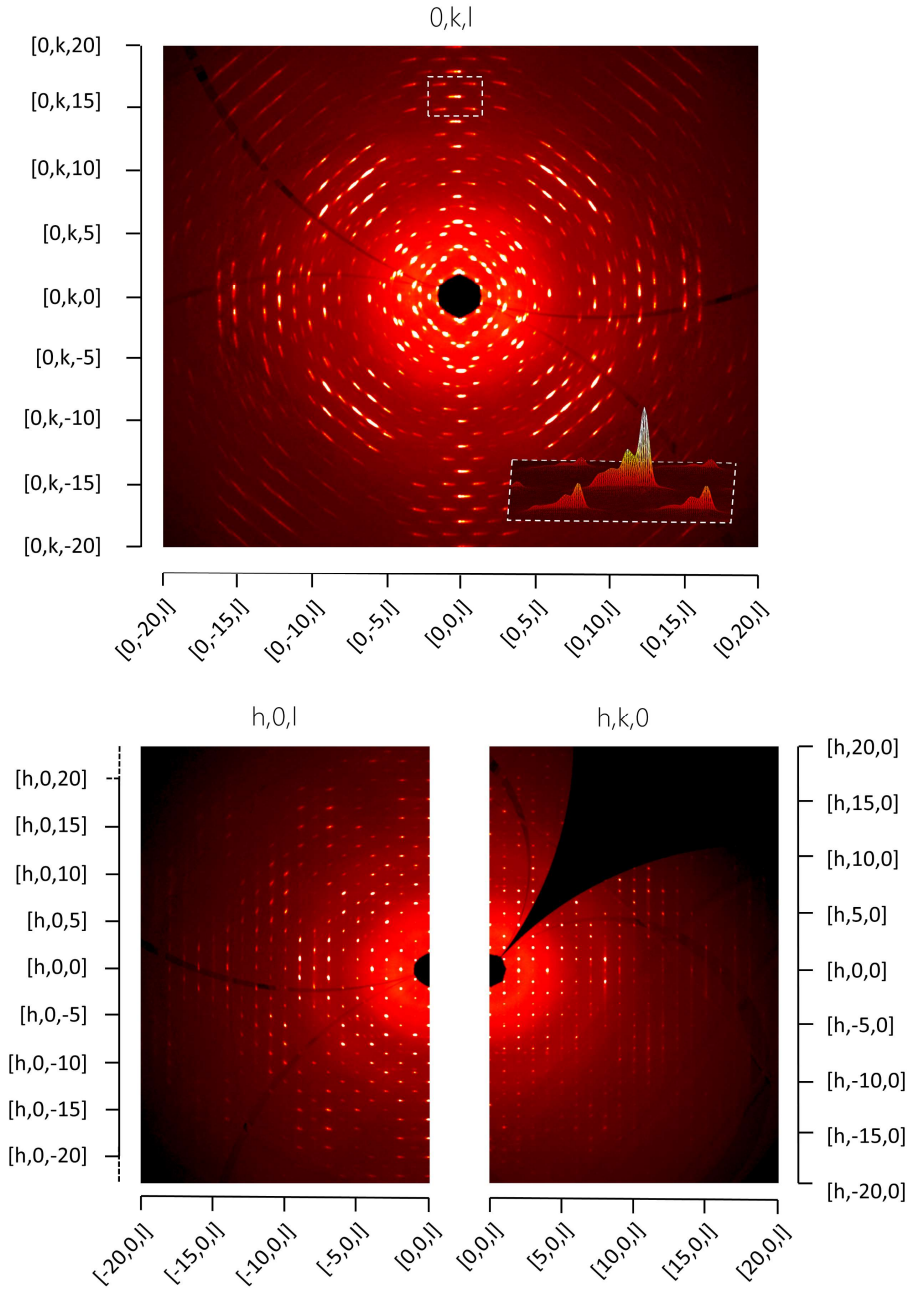

Figure 2.11. Reconstructions of the (0,k,l), (h,0,l) and (h,k,0) planes of the Co-IRMOF-9 reciprocal space elaborated by using the "Unwarp precession images" function of CrysAlisPro software[57]. The (0,k,l) plane contains a 3D plot of the above shown region (dotted line), showing the splitting of every Bragg peak into 4 signals belonging to 4 major crystalline domains.

2.4 · Co-IRMOF-9 direct synthesis attempt: CoBPDC1 and CoBPDC2

Since the structure of Co-IRMOF-9 has never been reported, its direct synthesis was attempted by replacing $Zn(NO_3)_2 \cdot 6H_2O$ with $Co(NO_3)_2 \cdot 6H_2O$ in the IRMOF-9 synthetic procedure (paragraph A.1.6, Appendix). As expected, Co-IRMOF-9 did not form and another phase was obtained as prismatic violet crystals (CoBPDC1). After the synthesis, the system was left to reach room temperature, but after less than one minute the crystals were observed to crush (Figure 2.12) yielding a mass of pink platelets (CoBPDC2).

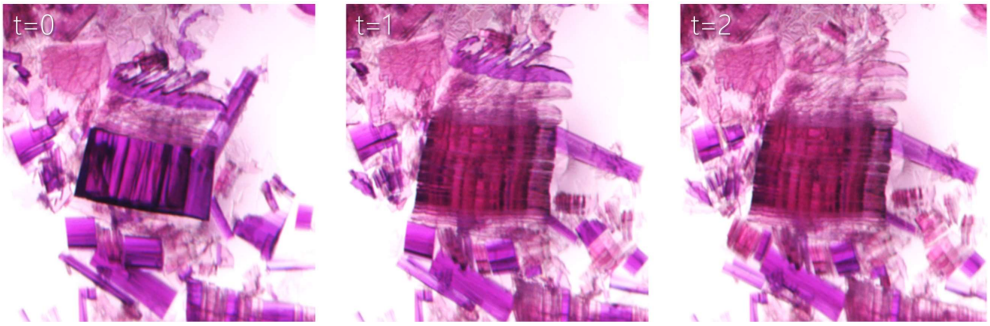

Figure 2.12. Optical microscope pictures of the CoBPDC1 crystals crushing in CoBPDC2 during the temperature decrease (t=0,1 and 2 progressively).

Structural analysis of the different crystals conducted at 353K and 100K revealed two phases. CoBPDC1 transforms reversibly into CoBPDC2 at 328K, as demonstrated by DSC analysis (DSC3, Section A.6, Appendix). Moreover, if the crystals of CoBPDC1 are removed from DMF, the transition does not occur anymore, thus suggesting that the solvent plays a determining role in the transformation.

CoBPDC1 consists of a 2D coordination polymer formed by bridging together linear trinuclear Co clusters (Figure 2.13). Both the Co pairs recognisable in the cluster are kept together by three BPDC anions forming, along the cluster axis, a 3-fold wheel. In this way, each cluster is connected to six other ones by means of six BPDCs. The central Co of the cluster features an octahedral coordination geometry, whereas the terminal ones have a pseudo tetrahedral one. This explains the violet colour as a combination of the pink and the blue colours typical for these coordinative environments when Co is involved.

The coordination bond only develops perpendicular to the Co_3 cluster axis, since every terminal metal is coordinated, in the free axial position, by a DMF molecule. The resulting layers pack together by filling the voids formed by a layer with the DMFs belonging to the

next one, and so on. The final solid voids amount to 1260.95Å^3 per unit cell, constituting 39.6% of the total volume, but these cavities are not connected with each other. Therefore, this phase cannot be considered as porous.

The situation in CoBPDC2 is significantly different, in agreement with the observed phase transition. The structure was determined by analysing a single platelet, whose diffraction data quality was found satisfactory. However, the phase revealed to be affected by merohedral twinning and this information has been integrated in the model to obtain an optimal refinement.

In this case, the building block is the same constituting CoBPDC1, the only difference being the coordination sphere of the terminal Co atoms of the Co_3 SBUs (Figure 2.14). In fact, in CoBPDC2 each atom is coordinated by two DMF molecules instead of only one.

The coordination geometry of all the Co centres is therefore octahedral, ad this justifies the pink colour of the solid. From a symmetry point of view, the transition comes with the loss of the inversion centre in the network and, consequently, in the space group, which goes from $P2_1/n$ to Pn.

Based on the structures of CoBPDC1 and CoBPDC2, it is possible to give a rationalisation of the afore mentioned phase transition, which resembles the one observed at low temperature for IRMOF-9. Indeed, the coordination number around the metals increases under a certain temperature causing the breaking of the starting solid and a symmetry decrease.

However, in the case of IRMOF-9, DMF is trapped in the voids, thus being able to trigger the phase transformation from within. In the case of CoBPDC1 the framework does not feature voids to accommodate the molecules of DMF and then the transition becomes feasible only when the crystals are in contact with the solvent.

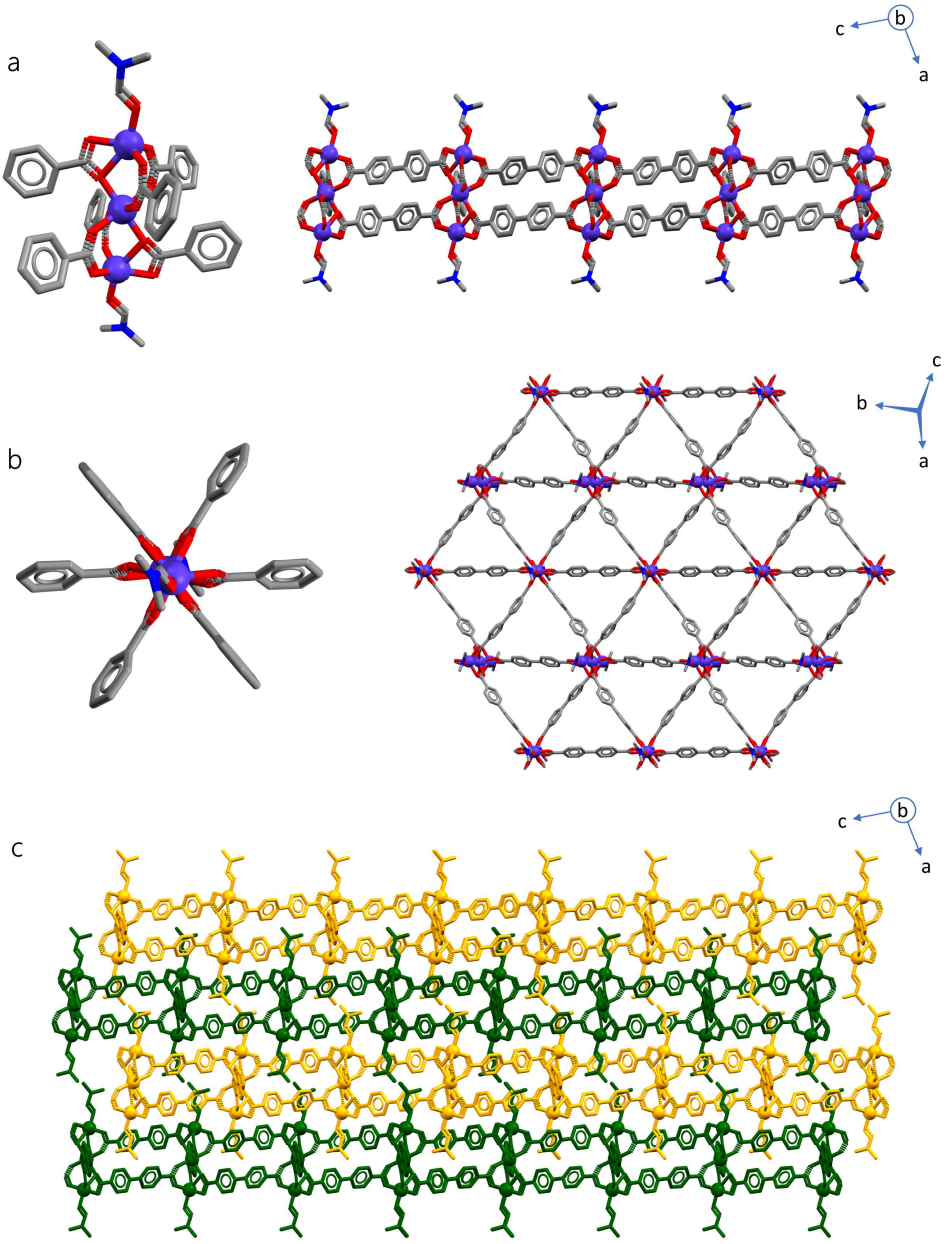

Figure 2.13. The CoBPDC1 structural features are briefly shown. From the upper left corner, the SBU with the coordinated linkers are shown perpendicularly (a) and along (b) the Co_3 axis; the hydrogen atoms are omitted and the linkers molecules halved for the sake of clarity. The resulting 2D networks are reported beside the two building block pictures. Below, the layered disposition of adjacent network planes is represented by showing neighbour planes coloured differently (c).

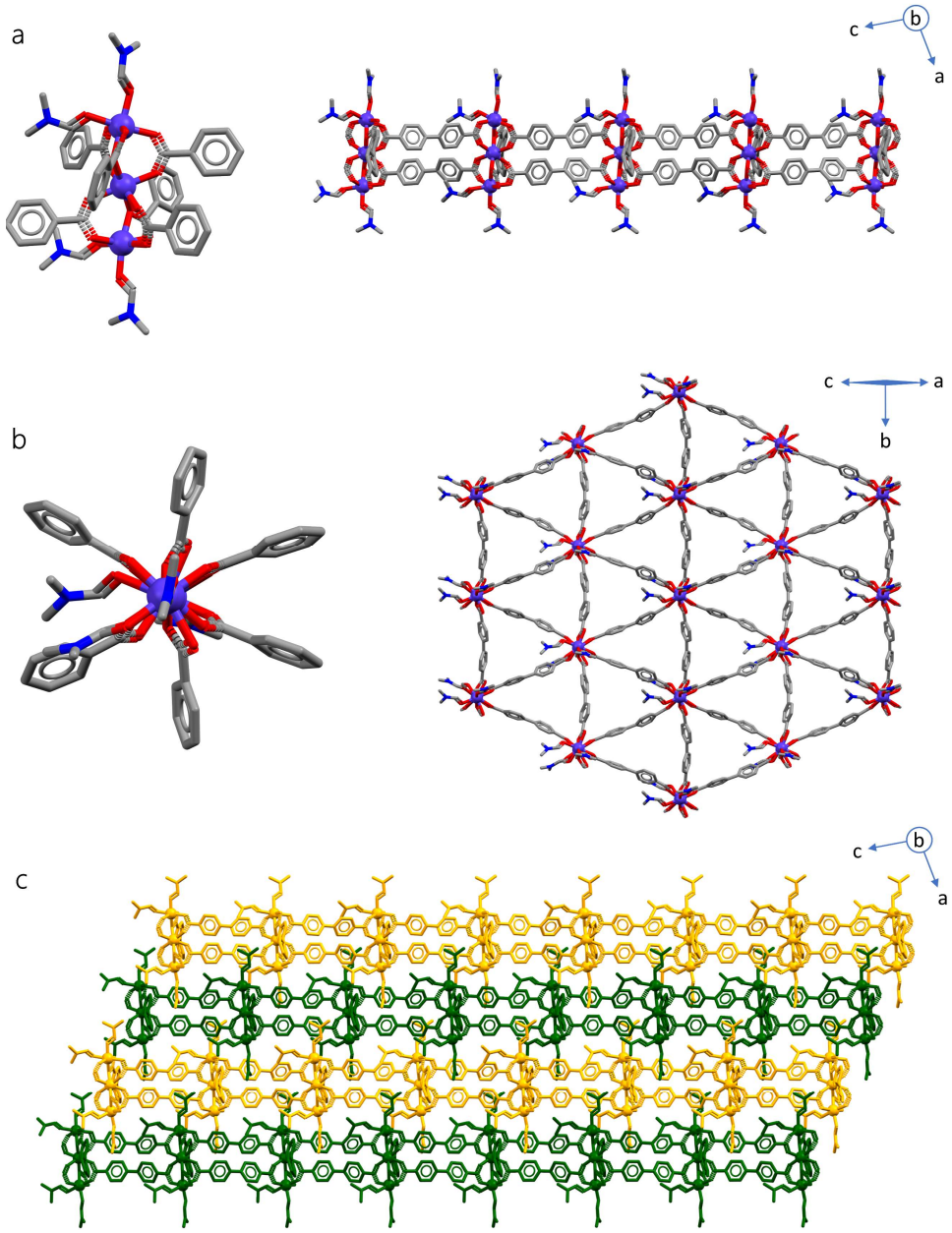

Figure 2.14. The CoBPDC2 structural features are briefly shown. From the upper left corner, the SBU with the coordinated linkers are shown perpendicularly (a) and along (b) the Co_3 axis (the hydrogen atoms are omitted and the linkers molecules halved for the sake of clarity). The resulting 2D networks are reported beside the two building block pictures. Below, the layered disposition of adjacent network planes is represented by showing neighbour planes coloured differently (c).

2.5 · Concluding remarks

The unsuccessful direct synthesis of Co-IRMOF-9 proved that this is a metastable phase. This evidence agrees with the rarity of tetrahedral Co-based SBU of the type M_4O (M=metal), very common in the case of Zn instead. Indeed, to date, only two examples of coordination polymers featuring analogue SBUs have been reported in the literature[71]. However, in these examples two different Co_4O SBUs are bridged by linear carboxylate-pyrazolate ligands, causing an alternation of O-containing and N-containing SBUs.

The transmetalation process is isomorphous, reversible and capable of reaching completeness in a relatively short time. By comparing these performances with those reported for MOF-5[46], it appears that IRMOF-9 is more prone to undergo transmetalation. In fact, in the case of MOF-5, the optimised Zn-to-Co exchange ratio does not exceed 25%, which means one metal for each SBU, and the attainment of single crystal specimens were never feasible. In a paper investigating the transmetalation phenomenon in MOFs based on Zn_4O SBUs, Brozek et al studied the importance of DMF dynamic binding through a combined experimental-computational approach[72]. Their Molecular Dynamic simulations showed, for the Zn atoms, a variable coordination number, which ranges from 4 (no DMF on the metals) to 6 (2 DMFs coordinating the metals). The authors claimed that this fluxional behaviour allows a structural flexibility which enables the cation exchange.

The phenomenon and its explanation can be transferred also to the case of the Zn-to-Co transmetalation of IRMOF-9. Its capability of exchanging completely the metal centres can be due to the bigger size of the pores and to the presence of the two mobile interpenetrated networks, which confers, at the same time, additional structural flexibility and stability. The SBU coordination distortion caused by the presence of the interpenetration might indeed result in a more labile bond of the linker molecules, therefore making the SBUs more accessible to solvent binding and cations substitutions without dramatic damages to the overall framework. Furthermore, the distortion of the linkers disposition in Co-IRMOF-9 and their peculiar type of disorder corroborates this hypothesis. All these deviations from the starting solid could indeed be attributed to a relevant hindrance present on the Zn exposed to the hollow part of the framework, where DMF molecules can establish dynamic bindings during the solid assembly.

Chapter III

Synthesis and structural analysis of TiO_x@IRMOF-9

"Any increase in knowledge anywhere
helps pave the way
for an increase in knowledge everywhere."

Isaac Asimov

"Isaac Asimov Book of Science and Nature Quotations"
1988

3.1 · MOFs and nanoparticles

In the introduction, MOFs have been presented as one outstanding class of materials in the current nanotechnology panorama. This definition was given by considering the bottom-up approach used to synthesize these solids, whose size scale can vary from nm to mm and therefore does not confer them the nanomaterial qualification by itself.
On the other hand, if we consider their porosity and the scale of the chemical reactions MOFs are used for, it is reasonable to say that these materials perform their functions at the nano-scale.
Going back to nanomaterials, MOFs can be related to this field in two ways. Firstly, their size can be tuned to the nano-region, thus yielding MOF nanoparticles (NP), which have a special potential in drug storage and in catalysis[73–76].
Moreover, MOFs can be used for the synthesis of functional NP by exploiting the solid as a precursor or a mould. In the first case, the material is usually designed with a certain composition (and, if needed, content), and its calcination is performed to obtain the final material, which can be achievable as NP[77–79]. The second use is more connected to the present work, and will be described in the following paragraph.

3.1.1 · MOFs as nanoporous moulds

The idea of exploiting the nanoconfined environment represented by MOFs cavities to synthesize nanomaterials with a pre-defined size appeared in 2008, when MOF-5 was used for the attainment of functional inorganic metal-NP such as Cu [80], Ru [81], and ZnO [80].
Later on, the list of achievable materials was extended also to Ni, Pd, Pt, Ir, Au and Ag, the main purpose being to achieve an outstanding catalytic performance in several chemical reactions such as Suzuki coupling[82], oxydation[83–85], hydrogenation[86–90] and reduction[85]. Generally, in these cases the reaction can be considered a functionalisation of the framework, since the final NP@MOF material is used without removing the NP from the cavities.
On the other hand, it is possible to conceive the porosity of a MOF as one single mould extending for the total length of the crystal. From this perspective, we can imagine of obtaining a material whose porosity is strictly related to that of the starting solid, which, in turn, can be eliminated by thermal or chemical treatment. This idea has not been particularly explored and the papers inspired to this concept are rarely found in the literature. In facts, only one paper, published in 2013 by Hall et al[91], mentions an analogue idea.

In this work, the authors described the synthesis of a TiO_2-based material made by replication of a MOF (HKUST-1 in this case). The characterisation of the final material by XRPD and electron microscopy is reported along with the gas adsorption performances, although without structural elucidation regarding the final and the intermediate products are presented.
This chapter describes the work done by adopting the idea of MOFs as potential moulds for the fabrication of a porous TiO_2 (titania) replicate. However, the focus will be the attainment of accurate structural information regarding the behaviour of the solid during the synthesis process.

3.2 · TiO_x@IRMOF-9

As already mentioned, titania was selected as target material to be grown inside IRMOF-9 because of the manifold applications this material has in photocatalysis. As a matter of facts, the performances of different titania phases in this field are known and exploited since decades[92,93]. The use of MOFs for this purpose was first proposed in 2009 by Müller et al[94], but remained rather limited in the following years, especially with respect to the structural information concerning the final phase.
In the following part, the synthesis and structural characterisation of the TiO_x@IRMOF-9 composite material is provided, aiming to gain precious insights regarding the behaviour of IRMOF-9 in this post-synthetic treatment. This kind of information is crucial whenever further procedure optimisations and extensions to other MOF systems are pursued.

3.2.1 · Synthesis and macroscopic behaviours

TiO_x@IRMOF-9 was prepared by soaking IRMOF-9 crystals in pure titanium isopropoxyde (**$Ti(iPrO)_4$**) for 30 days at room conditions (paragraph A.1.7, Appendix). This time span was selected to reasonably ensure a complete dispersion of the precursor in the solid cavities.
The as-synthesized TiO_x@IRMOF-9 does not show any apparent differences with respect to native IRMOF-9. SCXRD analyses confirmed that the crystals remained single after the treatment; the relative structure will be detailed in the following paragraphs.

By exposing this material to air, the colour of the crystals changes from white to an opaque yellowish white (Figure 3.1), as a sign that another titanium oxide based material (**TiO_xM1**) is obtained. Remarkably, TiO_xM1 exhibits interference colours, since orangish reflexes appear and fade out as the powder is rotated (Figure 3.1, b).

The overall crystal habit is retained, but not the crystallinity of the material before the exposure to moisture, since SCXRD analyses performed on TiO_xM1 showed no diffraction peak. Further XRPD analyses confirmed the crystallinity of the material, whose structural features can be related to IRMOF-9 (XRPD3, Section A.7, Appendix).

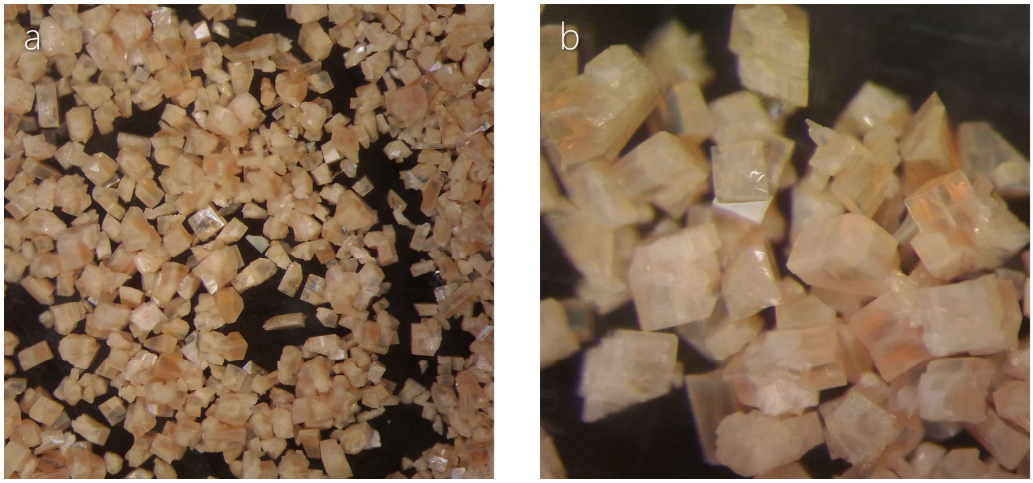

Figure 3.1. Optical microscope images of TiO_xM1. The mm-sized crystals are shown with a 10x and a 40x magnification (a and b respectively); the latter view is reported to better appreciate the orangish interference colours featured by the material in certain orientations.

3.3 · Total Scattering SCXRD analyses

To avoid the hydrolysis of $Ti(iPrO)_4$ present in the solid, TiO_x@IRMOF-9 crystals were washed with iPrOH prior to be subjected to SCXRD analyses; these were performed at 100K with synchrotron light (paragraph A.2.2, Appendix).
Six crystals in total have been analysed; all of them was confirmed as single crystalline domains. However, their structural nature has proven to be completely different with respect to native IRMOF-9, being the XRD patterns marked by the presence of strong diffuse scattering (Figure 3.2). This is a distinguishing feature of the so called **complex materials**, i.e. crystalline solids whose structures feature both an average long-range structure and a short range order distributed in the entire domain[95].

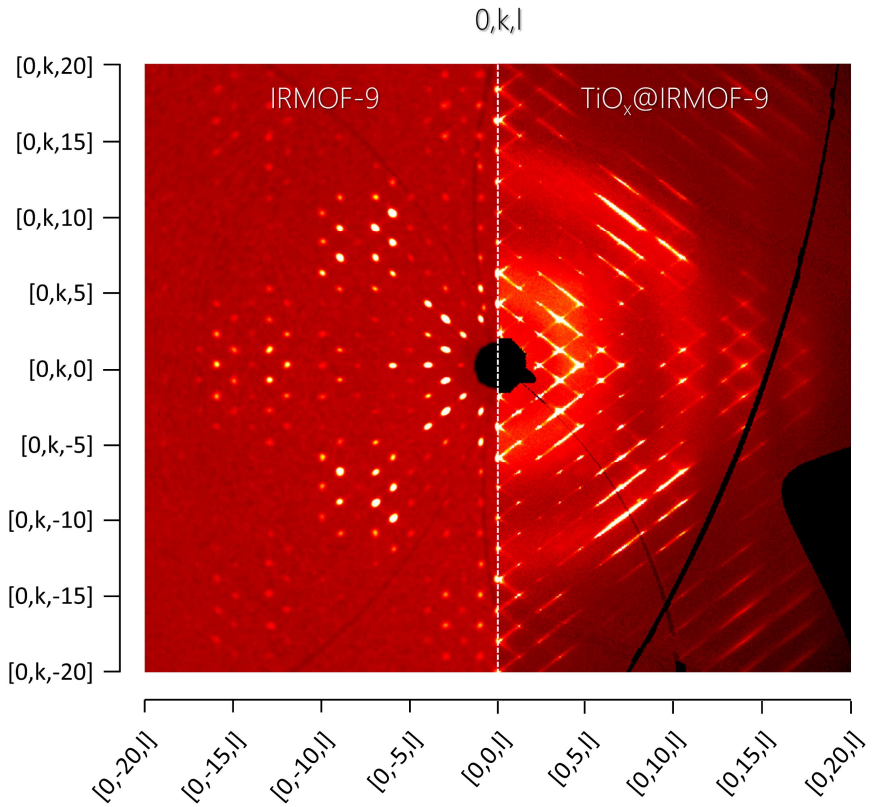

Figure 3.2. Comparison between precession images showing the reciprocal space (0,k,l) plane of native IRMOF-9 and TiO_x@IRMOF-9 (one representative sample); the presence of strong diffuse scattering passing through the Bragg peaks is clearly evident in the second phase.

This evidence clearly shows that the post-synthetic treatment introduces disorder in IRMOF-9 without remarkably affecting its crystallinity.
In such cases, the classical crystallographic approach, which only considers the coherently scattered intensities, is not able to provide an exhaustive structural description of the material. Therefore, a total scattering strategy is essential. This consists in facing the problem based on the following actions:
I) Classical structure solution by using the information contained in the Bragg reflections.
II) Qualitative evaluation of the diffuse scattered intensities.
III) Monte Carlo simulations of disordered phases aiming to reproduce in calculated XRD patterns the features observed in the experimental ones.

Although classical crystallography by itself is not sufficient to solve these kind of structural problems, it is important to underline its crucial role in extracting from Bragg intensities information relative to the disorder affecting the phase. It is true that this information is present in an "averaged" form and, moreover, the quality of the data is deteriorated by the presence of the diffuse scattering.
However, this averaged information contains potential indications on the nature of the disorder affecting the solid. In case these indications are unveiled, they constitute the bases for the interpretation of the phase complexity, which will be subsequently validated by correlating them with the diffuse scattering qualitative analysis and, in the end, tested with Monte Carlo simulations.

3.3.1 · Average structure determination

Each one of the six analysed samples has a different unit cell, always deviating from that of native IRMOF-9 (table 3.1; graph 3.1). All of them maintain the space group of the starting material (Pnnm) and, although the analyses were conducted at low temperature (100K), in no case twinning was observed, differently from the starting IRMOF-9 (paragraph 1.2.1, Chapter I).
The overall framework connectivity is retained as well as the relative disposition of the two interpenetrated networks, which feature, for the "linker embraced" SBU pairs (paragraph 1.1.1, Chapter I), an average SBU-SBU distance of 10.226±0.111Å, not significantly lower with respect to that of IRMOF-9 (10.594Å at 258K).
As for the solvent molecules, only the disordered DMF trapped between the SBUs (Figure 1.6, a, Chapter I) was clearly recognisable.

	TiO_x@IRMOF-9 Sample 1	TiO_x@IRMOF-9 Sample 2	TiO_x@IRMOF-9 Sample 3	TiO_x@IRMOF-9 Sample 4	TiO_x@IRMOF-9 Sample 5	TiO_x@IRMOF-9 Sample 6
a (Å)	17.1172(3)	17.1424(2)	17.1127(2)	17.1249(2)	17.1229(2)	17.1689(3)
b (Å)	23.3182(5)	23.0158(4)	22.3852(5)	22.2575(4)	21.8088(5)	20.4106(14)
c (Å)	25.0552(5)	25.3071(4)	25.8191(4)	25.9268(4)	26.2024(4)	27.1330(10)
V (Å³)	10000.6(3)	9984.8(3)	9890.6(3)	9882.2(3)	9784.8(3)	9508.2(8)

Table 3.1. *Cell axes and related volumes of IRMOF-9 (258K) and the six TiO_x@IRMOF-9 samples measured at 100K. The cell angles are not reported and equal to 90°, the space group being Pnnm in all cases. The samples have been organised in ascending order of deviation from the native MOF values.*

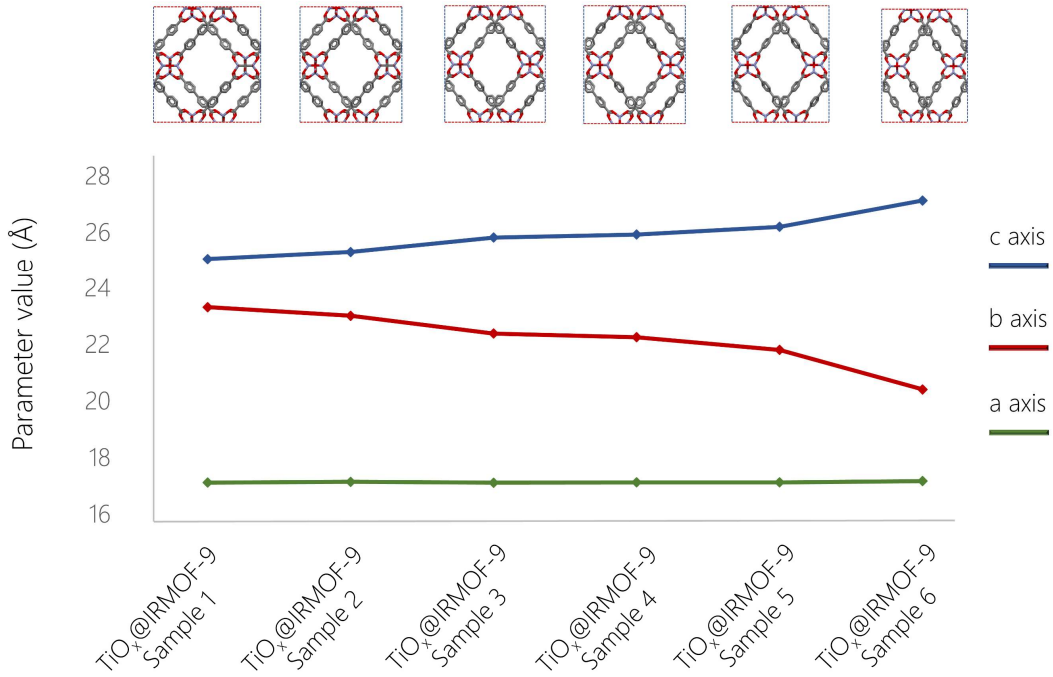

Graph 3.1. *TiO_x@IRMOF-9 cell axes values for the six analysed samples. Above, the unit cell content for each sample is displayed along the crystal axes a (the one that varies the least), to highlight the distortion of the framework. The plotted data are taken from table 3.1.*

3.3.1.1 · Framework disorder analyses

The analysis of the difference electron density maps allowed to model a peculiar type of disorder, which was found in every sample (Figure 3.3). As a matter of fact, every Zn atom of the SBU has four additional positions along the *b*+*c* and *b*-*c* crystallographic directions. Their occupancies refinement is not reliable due to the data quality; the values ranges indicatively from 0.025 to 0.05. This effect is systematically present in each sample regardless of the data resolution or the diffuse scattering intensity.

A positional disorder along the same directions and with analogue displacement length affects every linker molecule lying perpendicular to the *a* crystallographic direction (Figure 3.4-3.5). These are four out of six for each SBU, the remaining two being affected by another kind of positional disorder caused by different equilibrium positions of the rotating phenyl rings, as in the case of Co-IRMOF-9 (section 2.3, Chapter II).

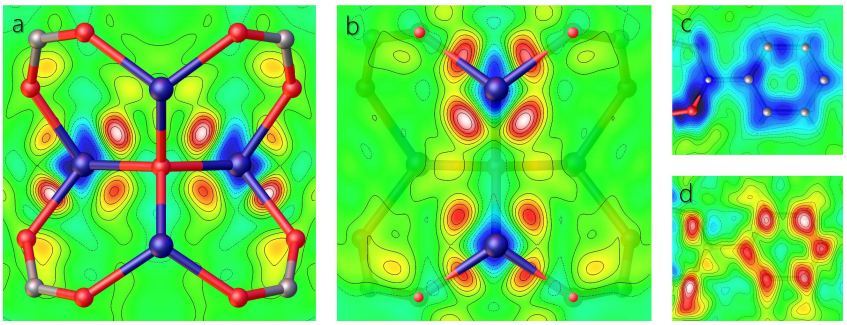

Figure 3.3. Difference electron density maps calculated and displayed by Olex2 software. Overestimated electron density (blue colour) is present where the SBUs (a and b) and linkers (c and d) are modelled, whereas underestimated electron density (red colour) can be found in the near surroundings, coherently with the presence of additional positions for both SBUs and linkers.

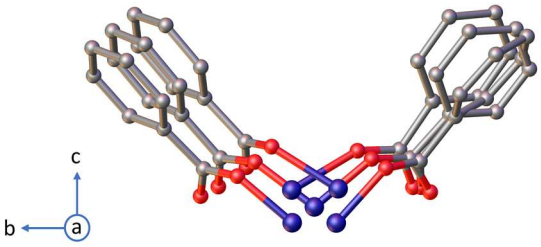

Figure 3.4. The correlation between the displacement of the linkers and that of the metal centres is highlighted; the linker molecules are halved and the hydrogen atoms are not shown for the sake of clarity.

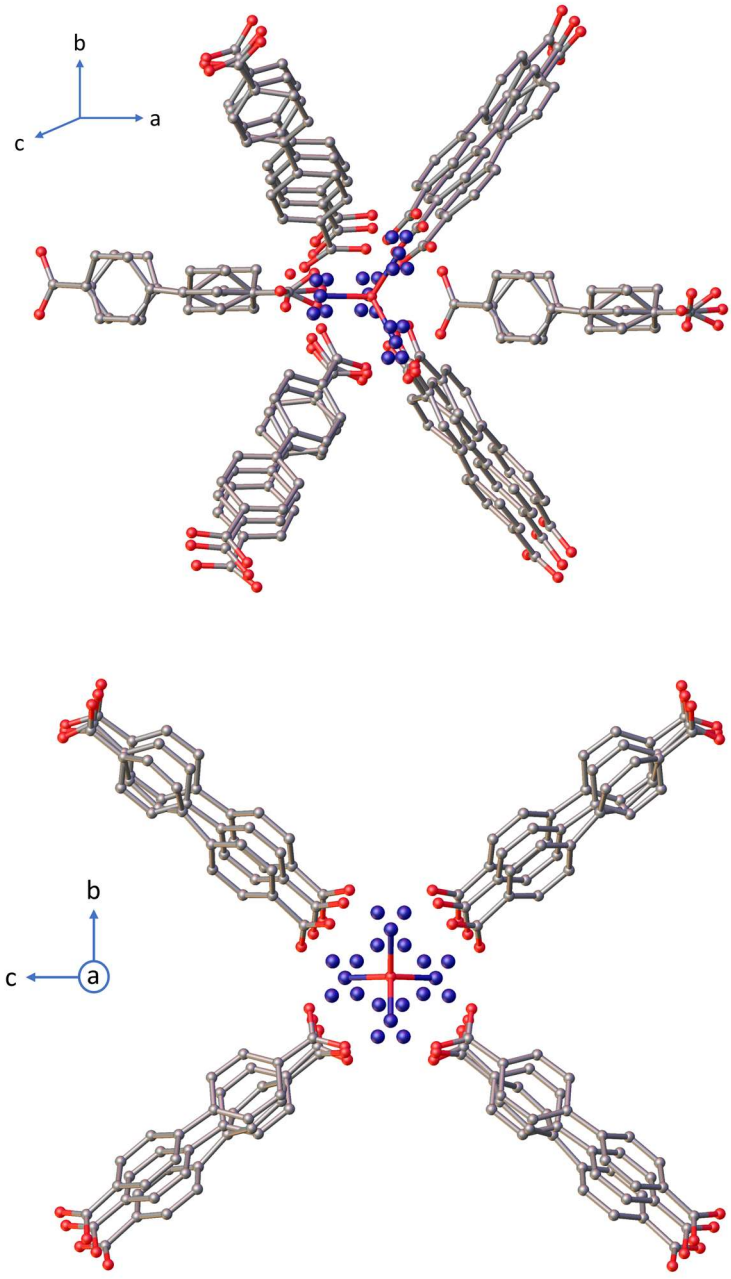

Figure 3.5. The disorder affecting the SBU and its linkers is displayed along different crystallographic directions using Olex2 software. The linker-Zn bonds and the hydrogen atoms are not shown for the sake of clarity.

None of the analysed samples afforded any information regarding the cavity content, except for one case (Sample 2 in table 3.1 and graph 3.1), in which a titanium oxo-aggregate was observed to be linked to the SBUs by means of an Ti-O-Zn bridge (Figure 3.6-3.7).
For a given occupancy value, the atoms composing this aggregate feature different thermal parameters, which increase with the distance from the oxo-bridge keeping it anchored to the SBU. Since occupancies and thermal parameters correlate to each other, a reliable refinement of the two values has not been possible. The increased thermal parameters can be due to a static disorder of the aggregate, which, in case of displacement, can occupy different positions while remaining bound to the SBU, resulting in bigger shifts for the more peripheral atoms. This disorder is probably the reason for the impossibility to model the aggregate terminal groups, which appear as a shapeless electron density likely belonging to isopropoxy groups.
The assignment of the atomic charges is not fully reliable as well, because the aggregates are incomplete and more than one form might be present in the solid. At present, a satisfying modelling of the electron density has not been possible with the available data. Moreover, the geometrical features of the Ti-oxo-aggregate are not perfectly stable during the structure refinement, and while the titanium positions do not vary, those of the μ2 bridging oxygens tend to diverge. Hence, it is possible to conclude that the structural analysis confirms the formation of a titanium oxide aggregate in the solid framework of IRMOF-9, whose structural location was made possible by the construction of a Zn-O-Ti bridge.

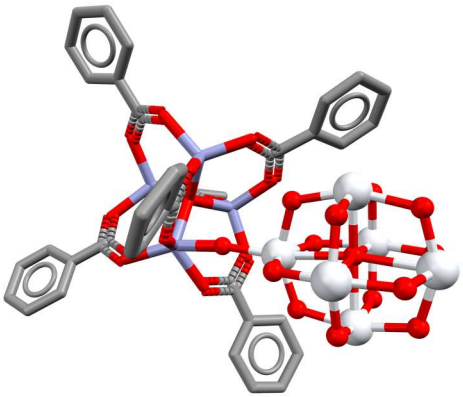

Figure 3.6. The titanium oxo-aggregate modelled inside the cavities of one TiO_x@IRMOF-9 sample; hydrogen atoms are omitted and BPDC molecules are halved for the sake of clarity. Around the Ti atoms with vacant coordinative positions residual electron densities can be found, which are consistent with the presence of isopropoxy groups, although not possible to model satisfactorily.

To our knowledge, this is the first case of a MOF successfully used for the synthesis of a metal oxo-cluster, whose attainment is only achievable in the MOF pores. Moreover, its structural features are unprecedented in titanium oxo-clusters chemistry and have been observed only in Mo [96], W [97], V [98,99], Nb and Ta [100] analogues.

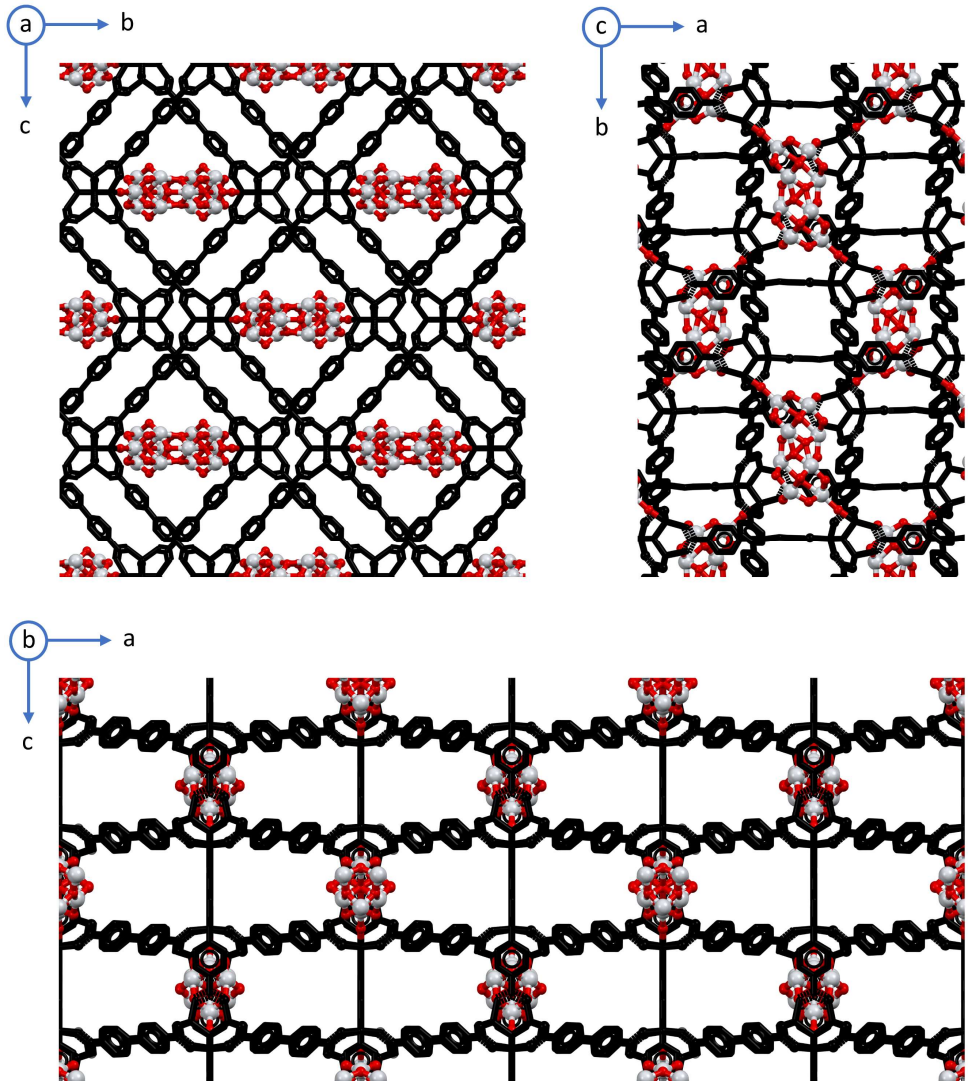

Figure 3.7. The disposition of the modelled aggregate is displayed along the a, b and c crystallographic directions. The framework is marked with a black colour to highlight the titanium oxo-aggregate, which is doubled by symmetry.

3.3.1.2 · Disorder hypotheses from Bragg analyses

The average structure analyses conducted on all six samples afforded three important pieces of information, which led to three hypotheses for the origins of the diffuse scattering found in the XRD patterns. For the sake of convenience, we will refer to these hypotheses by numerating them, following their order of appearance.

1) The noteworthy variability of the unit cell parameters, attributable to contractions and/or enlargements of the framework in a breathing-like movement, highlights the possibility that, while the observed unit cell represents the average one, differently distorted situations are present within the same crystalline domain. This would result in a positional disorder along the two axes perpendicular to the channel, i.e., *b* and *c*.

2) The positional disorder affecting SBUs and linkers in every analysed phase develops along the *b*+*c* and *b*-*c* crystallographic directions and might cause diffuse scattering.

3) The presence of the titanium oxo-clusters, whose partial presence could be discontinuously localised near to different SBUs and along the channel, might cause an occupational disorder along the *a* and *b* crystallographic directions.

3.3.2 · Diffuse scattering qualitative analyses

In order to evaluate the main qualitative features of the disorder affecting the phase, the incoherently scattered intensities have been scrutinised by analysing several slices of the reciprocal space, reconstructed by using the "unwarp" feature present in the CrysAlisPro software[57]. Since the diffuse intensities are qualitatively similar in all the analysed samples, in the following discussion the reciprocal space images of only one specimen (Sample 3 in table 3.1 and graph 3.1) are considered as representative of the general situation.

3.3.2.1 · Precession images evaluation

The (0,k,l), (h,0,l) and (h,k,0) planes have been considered to acquire a starting idea of the dimensionality and directionality of the diffuse scattered intensities.

The (0,k,l) plane (Figure 3.8) features diffuse intensities streaks along the *b**+*c** and *b**-*c** directions, generally centred on the Bragg reflections. These smears affect both directions for reflections with k:l or l:k indices ratios higher than 1 or lower than -1. When these ratios are close to 1, the intensities look broad along the *b**-*c** direction and sharp in *b**+*c** one. If they are close to -1, on the contrary, the intensities are diffuse along the *b**+*c** direction and sharp in the orthogonal one.

Overall, the diffuse scattering follows the Pmm symmetry present along this crystallographic direction, as well as the intensity modulations typical of the XRD pattern of pristine IRMOF-9. Importantly, the coherent-to-incoherent scattered intensity ratio decreases with the diffraction angle, since at very high 2θ values the Bragg contribution is hard to recognise, whereas the diffuse intensities are clearly present (Figure 3.9). This feature indicates that the disorder affecting the phase has a major positional component and a negligible occupational one.

A final remark regards the extra Bragg reflections present at low 2θ angles. These reflections, constituting ~ 14% of the total harvested by the software[57], have been successfully indexed as an additional twin minor component, whose unit cell is related to the main one by a rotation of ~124° about the -0.45 0.00 0.896 axis of the reciprocal space (-0.75 0.00 0.66 in the direct space). Since no significative geometrical correlation between the two domains has been found, and the presence of similar parasite phases affects also other samples, this feature will be considered as the consequence of the crystal break due to the fast-cooling to 100K or to the PSM itself. Therefore, no attention will be paid to this minor additional domain in the following discussion.

For layers defined by non-integer indexes the diffuse intensities are still present, although weaker with respect to the regions close to the Bragg reflections (Figure.3.8, bottom). These signals can be considered as the tails ot the strong diffuse streaks observed in the (n,k,l) planes (n= integer number).

In the (h,0,l) plane the diffuse scattering is remarkably weaker, although present mainly along the *c** direction (Figure 3.10). Again, these intensities form lines and are stronger in proximity to the Bragg reflections. The (h,k,0) plane features the same type of diffuse, this time mainly present along the *b** direction. By scanning the reciprocal space along *b** or *c** it is easy to recognise that each Bragg reflection splits into two discrete traces while going from an integer index plane to a non-integer one (Figure 3.10-3.11).

In the middle layer between two lattice planes each Bragg is spit along the vertical direction (*b** or *c** depending on the observed plane) into two evenly spaced signals. Each discrete signal joins an adjacent one while going back to the subsequent integer index layer, forming another Bragg reflection. This is caused by the fact that this reciprocal space scan sequence along *b** or *c** is slicing the diffuse "squares" present in the (n,k,l) planes. This correlates the diffuse intensities observed in the (0,k,l) plane with those of the (h,0,l) and (h,k,0) planes.

For this reason, the (0,k,l) plane can be considered representative of the main features of the diffuse scattering, and the following discussion, as well as the final simulations, will consider only this slice of the reciprocal space.

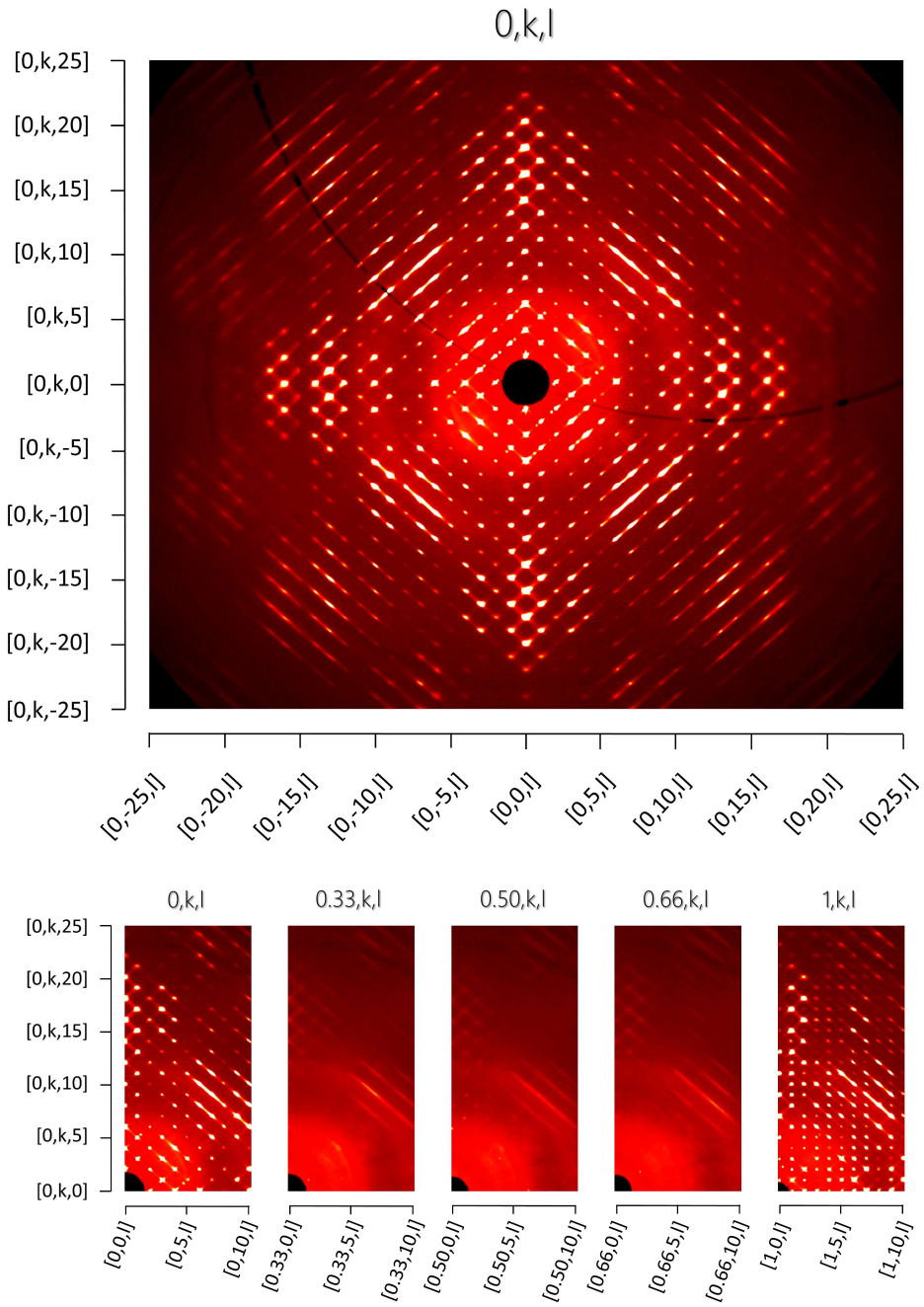

Figure 3.8. Above, reconstruction of the (0,k,l) plane of the TiO_x@IRMOF-9 reciprocal space. Below, a section of the kl region is displayed at five different h values to highlight the diffuse intensities trend between the lattice planes.

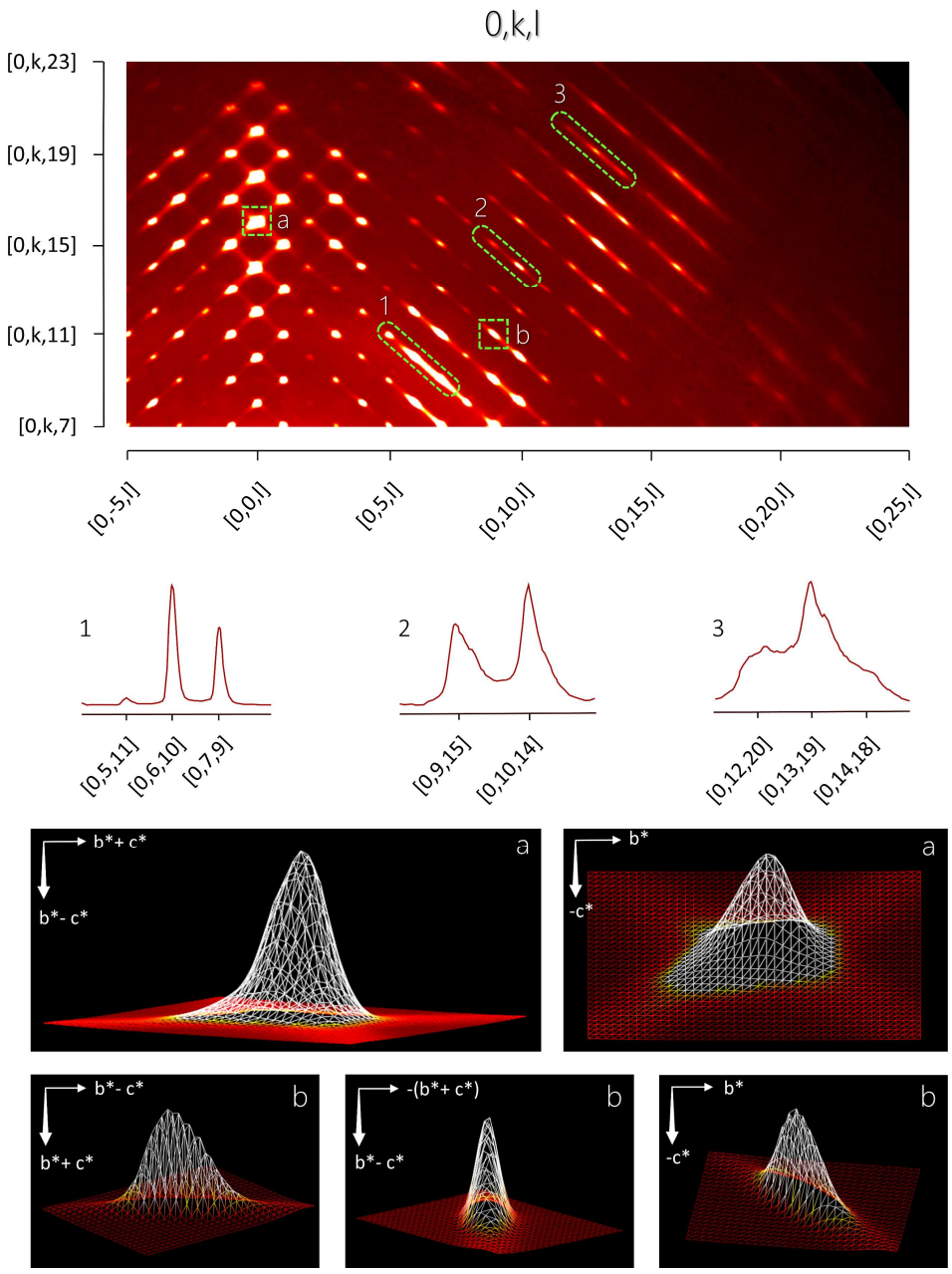

Figure 3.9. Some remarkable features of the diffuse scattering are highlighted. The directionality and anisotropic shape of the diffuse are highlighted by considering two reflections (a and b) in two different regions of the (0,k,l) plane. Below, the intensity profiles of three different regions at increasing 2θ angles (1, 2 and 3) confirms that the diffuse intensities raise while the Bragg decrease.

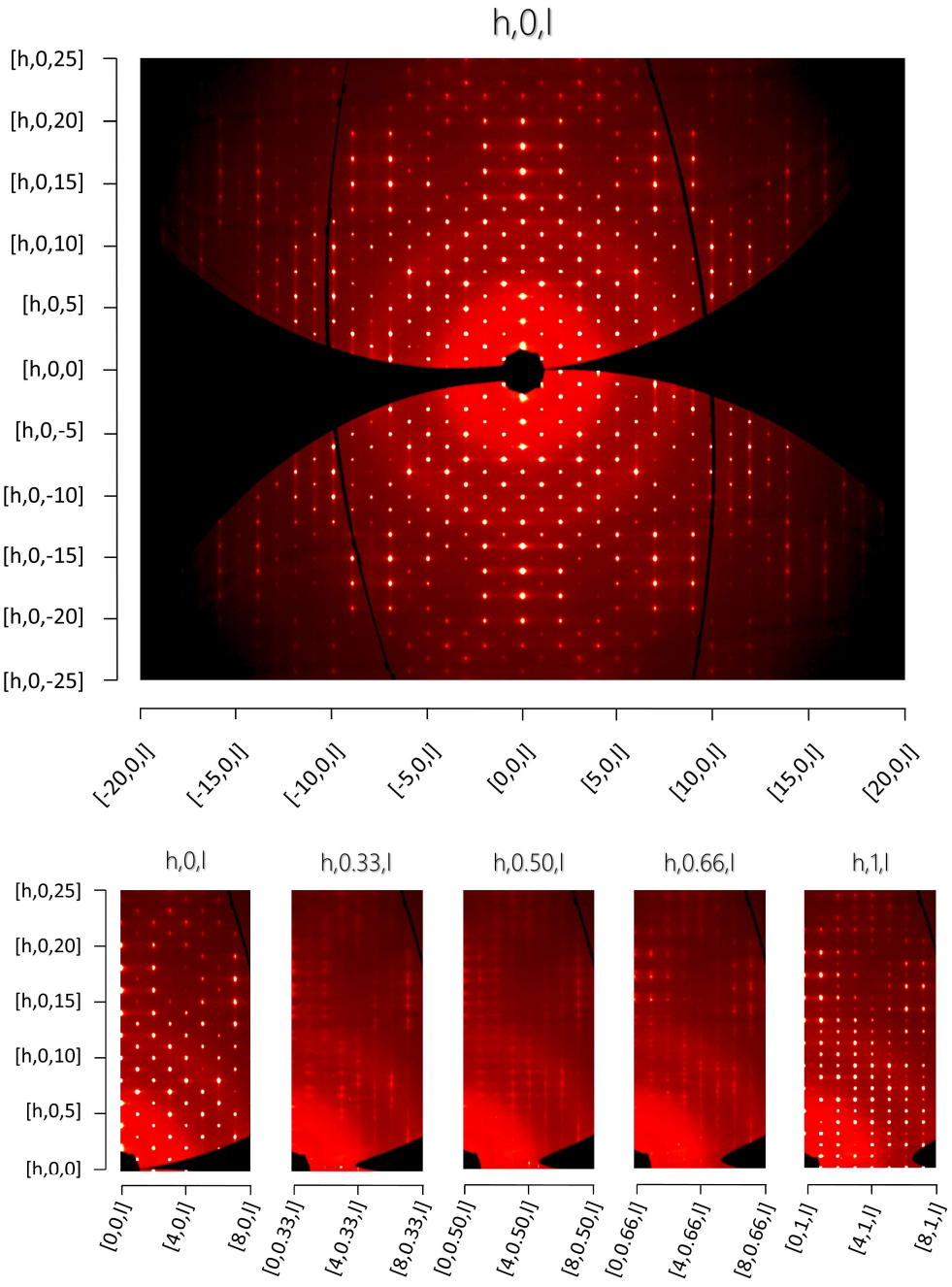

Figure 3.10. Above, reconstruction of the (h,0,l) plane of the TiO_x@IRMOF-9 reciprocal space. Below, a section of the hl region is displayed at five different k values to highlight the diffuse intensities trend between the lattice planes.

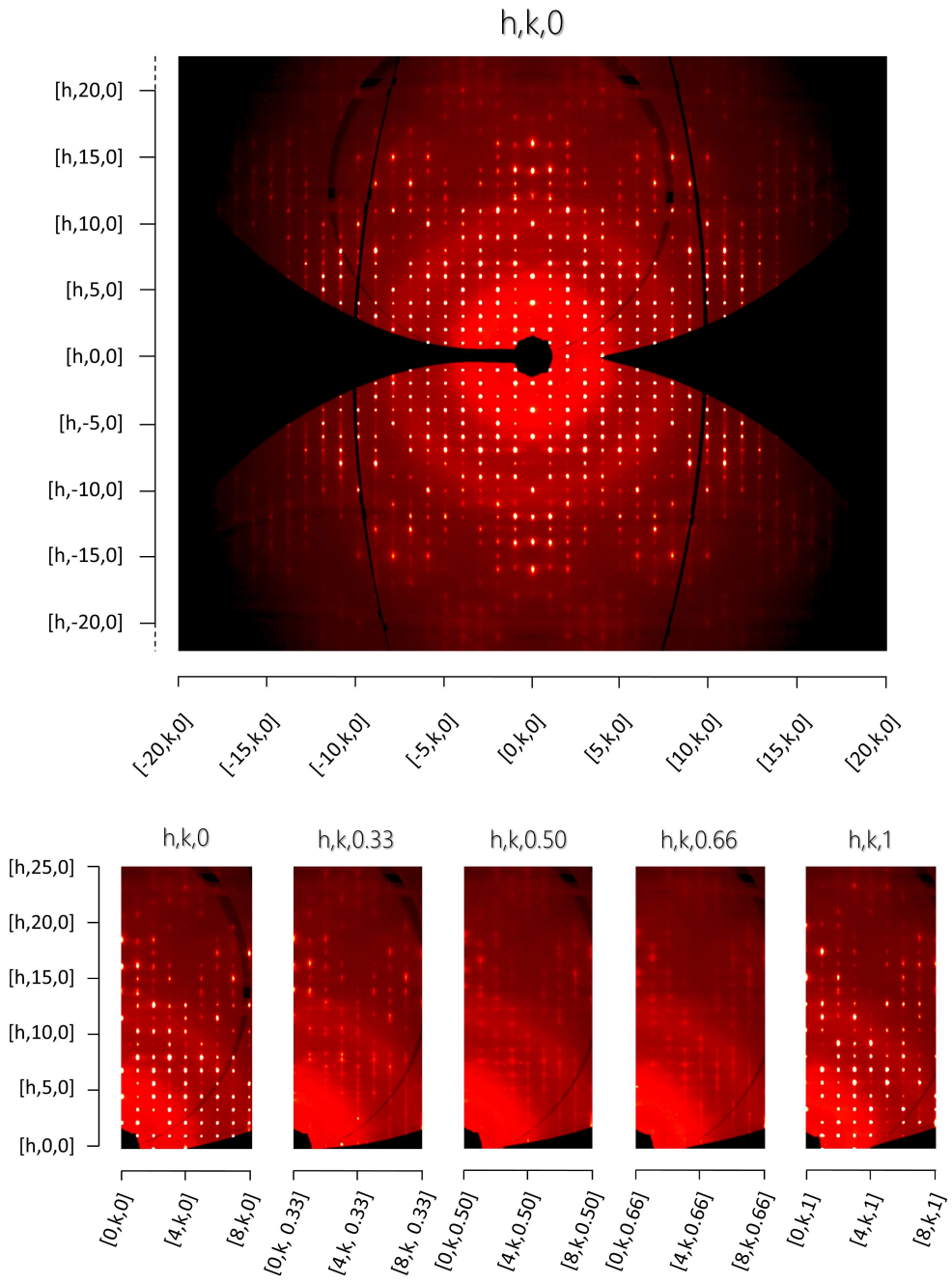

Figure 3.11. Above, reconstruction of the (h,k,0) plane of the TiO_x@IRMOF-9 reciprocal space. Below, a section of the hk region is displayed at five different l values to highlight the diffuse intensities trend between the lattice planes.

3.3.2.2 · Main information from diffuse scattering evaluation

The analyses of the precession images allowed an evaluation of the most significative features of the diffuse scattered intensities. Most importantly, the diffuse-to-Bragg intensities ratio increases with the diffraction angle, thus proving that the main disorder type in TiO_x@IRMOF-9 is positional. This suggests that the supposed contribution of the titanium oxo-cluster in this regard has a negligible weight in the occurring of the diffuse scattering observed in the sample XRD patterns. Therefore, the third hypothesis can be ignored in drawing up the candidate models for the Monte Carlo simulations.
The diffuse streaks develop in the b^* ad c^* directions of the reciprocal space, which corresponds to the *b* and *c* directions in the crystal domain. This means that the disorder affecting the phase involves the *b* and *c* crystallographic directions, but not the *a* one, consistently with the first and the second hypotheses. Moreover, the diffuse lines develop along precise lattice directions, and the main intensities are very close to the Bragg peaks, which suggests that the disorder type is strongly correlated with the average structure.

3.3.3 · Monte Carlo simulations

Monte Carlo simulations are among the most valuable tools for the study of disordered crystal structures. In this regard, the main approaches can be grouped in direct Monte Carlo (MC) and Reverse Monte Carlo (RMC)[102].
The first method consists in creating a real-space disorder model, based on realistic physical and chemical criteria. This model is described by near-neighbour interatomic or intermolecular interactions. The MC simulation then operates by creating several computed crystal samples affected by the imposed disorder, while minimising the energy of the crystal for the given set of interactions. Finally, the last step is a calculation of the disordered crystal domains diffraction patterns, which are compared with the experimental data. The near-neighbour interactions are adjusted and the disorder type adapted to minimise the difference between the calculated pattern and the experimental one. RMC methods, on the other hand, minimise the difference between the observed and calculated diffuse scattering intensities as a function of the positions and occupancies of the atomic sites in the model crystal, rather than the total energy of the crystal as it is in direct MC. In general, a RMC simulation provides one real space structure consistent with the experimental data, leaving to the operator any interpretation of the resulting structure which, in principle, might also have no physical meaning. Constraints to the variables are often implemented in the RMC scheme/algorithm to bound the solution within a region of the parameters space corresponding to chemically sensible structures.

Direct MC approach is more demanding, since it requires a previous interpretation of the diffuse intensities and the formulation of hypotheses to choose a chemically and physically sensible system as starting point. Nevertheless, this approach allows a deeper understanding of the disorder origins, which are the key to set up satisfactory simulations and solve the whole case with a critical eye.
In the present work, a direct MC approach has been adopted by using a dedicated software, namely Zurich Oak Ridge Disorder Simulation (ZODS). Its features and usage will be described in the following paragraph.

3.3.3.1 · Zurich Oak Ridge Disorder Simulation (ZODS)

ZODS[103] is a software which uses direct MC methods to compute defected phases models. The latter, in turn, will be used to calculate a diffraction pattern to be compared with the experimental one. To work properly, ZODS needs to be provided with specific information. The operator creates an input file and starts by specifying a cif file to be used as a reference phase. Then, the chemical species with their own occupation probabilities are listed and a set of alternatives (SOA) is specified. This consists in a list of the atoms or molecules (according to the atom names present in the cif file) whose presence is exclusively related to the other ones by a certain arbitrary probability.
Conceptually, the "alternatives" are the average position and occupation of the chemical species in the perfectly ordered phase, and the position and occupation of those who deviates from the average. For instance, if in a real sample we have an atom X(x,y,z) which is sometimes disordered in a secondary equilibrium position X'(x',y',z'), we include atom X(x,y,z) and an atom X'(x',y',z') in the atoms list, with their own occupation probabilities whose sum must be equal to 1. Therefore, we compile a SOA including the atom X and the atom X'. In such a manner, it is possible to specify atoms displacements and occupancies variations just by editing the mentioned parameters in the atom list and the corresponding SOA.
Once the input file contains the starting phase (the cif) and the type of disorder (described in terms of SOA), the program needs to know the interactions between the ordered and disordered chemical species. These are expressed by listing pairs of atoms among those in the atom list, and assigning an arbitrary integer number to the pair interaction energy: a negative energy is stabilising, a positive one is destabilising. In this manner, we can introduce and tune the correlations between defects to regulate the spatial distribution of their occurrence probability throughout the simulated crystal phase. This energy should not be intended in physical terms, but rather in computational ones.

A stabilising energy of this type is a value whose only role consists in indicating to the algorithm that a certain configuration created at a given MC cycle should be accepted. In case of destabilising energy, the final atomic configuration is usually rejected, although, rarely, also destabilising atomic dispositions are accepted to avoid false minima and give a more robust statistical value to the calculation outcome.
Finally, since the software is designed to compute disordered crystal domains and their diffraction patterns, the number and the size (in terms of unit cells) of these domains are specified, followed by the information regarding the simulation of their total scattering pattern (layer of the reciprocal space to be computed, intensities sampling step, etc.).
With these basic information, ZODS can create a crystal domain, insert random defects minimising the energy of the system according to the specified interactions, and provide the user with the final diffraction pattern. The subsequent work is up to the operator, who should critically examine the differences between the calculated pattern and the observed one and understand how to modify the disorder model (and the ZODS input file) towards the most fitting one.

3.3.3.2 · Simulations results for defect-free IRMOF-9

Before testing disorder models, the diffraction patterns of IRMOF-9 and some relevant modifications have been simulated to understand the origins of its typical intensity modulations (paragraph 1.1.2, Chapter I). For the sake of simplicity, since in a metal-organic phase the intensities coming from the metals dominate the diffraction pattern, only the Zn atoms have been introduced as chemical components in the ZODS input file. This approximation has been adopted in all the performed ZODS simulations.
Moreover, the simulated unit cell size has been set to 100x100x100 unit cells to ensure, for the adopted short-range correlations, a uniform defects distribution in the crystal domains.Several simulations have been performed in order to verify the effects of the intensity interferences caused by the presence of Zn atoms, which are not related by the simple translational symmetry of the crystalline phase.
The main tested effects have been the tetrahedral geometry of the Zn_4O clusters and the presence of the interpenetration of the two networks. For this purpose, in the first simulation IRMOF-9 structure has been modified by eliminating one of the two interpenetrated networks and by substituting every SBU with a Zn atom centred on the former SBU oxygen atom. The resulting diffraction pattern features no intensity modulation, and the intensities decrease with the increase of the distance from the origin of the reciprocal space, accordingly with the fall of the atomic scattering factors (Figure 3.12).

Subsequently, the effect of the SBUs shape has been tested by substituting the Zn atoms with Zn_4 tetrahedra in the previous simulation. As a result, the intensity undergoes a modulation along the b^*+c^* and b^*-c^* reciprocal space directions, and the overall intensity is clustered in square-shaped regions (Figure 3.13).

The effect of the interpenetration on the diffracted intensities is investigated by taking the original IRMOF-9 structure and substituting every SBU with a Zn atom centred in the SBU oxygen position. The resulting effect is an intensity modulation which dampen the diffracted intensities along b^*, causing stripes of Bragg reflections (Figure 3.14). The combination of the two observed effects can be recognised in the simulated pattern of IRMOF-9 (Figure 3.15), whose qualitative features concerning the intensity modulations are in good agreement with those observed in the experimental ones.

Since some of these features are also present in TiO_x@IRMOF-9 diffuse intensities, this information will be useful in the rationalisation of the disorder and its strong correlation with the average structure.

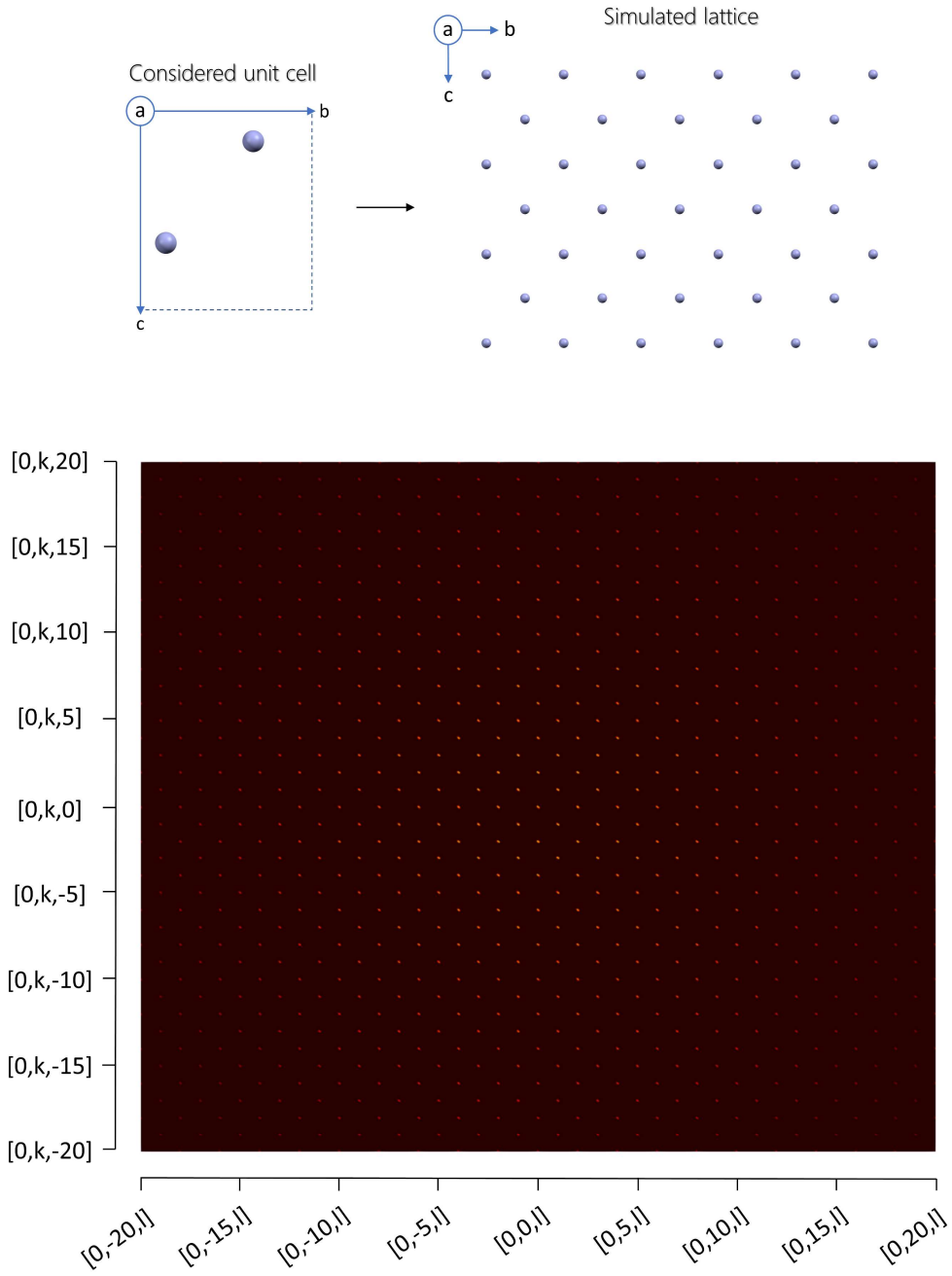

Figure 3.12. Calculated (0,k,l) plane of modified version of IRMOF-9, where only one of the two interpenetrated networks is present and every SBU is replaced by a Zn atom. Above, the considered unit cell and a fraction of the simulated lattice viewed along the a crystallographic direction.

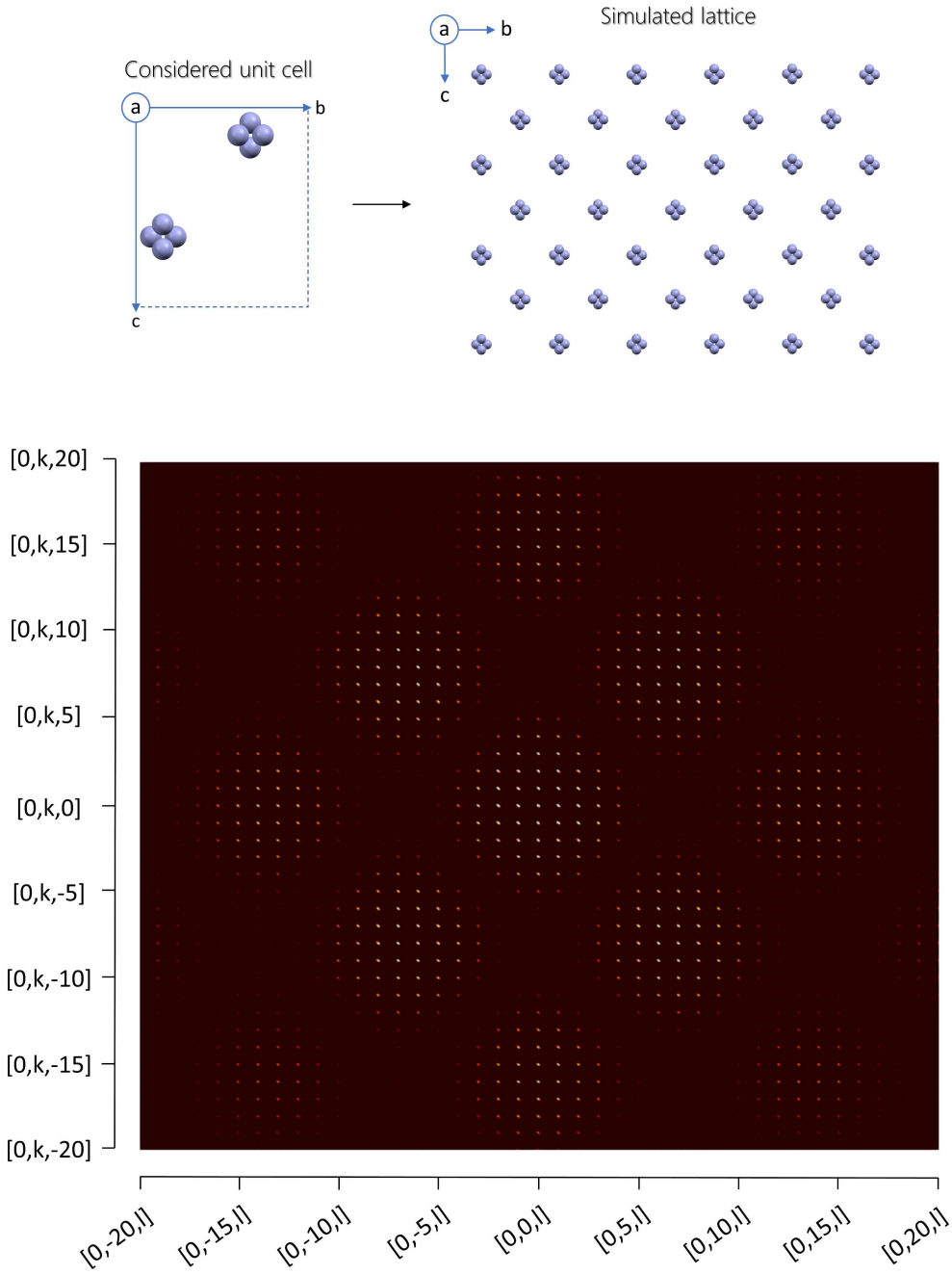

Figure 3.13. Calculated (0,k,l) plane of modified version of IRMOF-9, where only one of the two interpenetrated networks is present. Above, the considered unit cell and a fraction of the simulated lattice viewed along the a crystallographic direction.

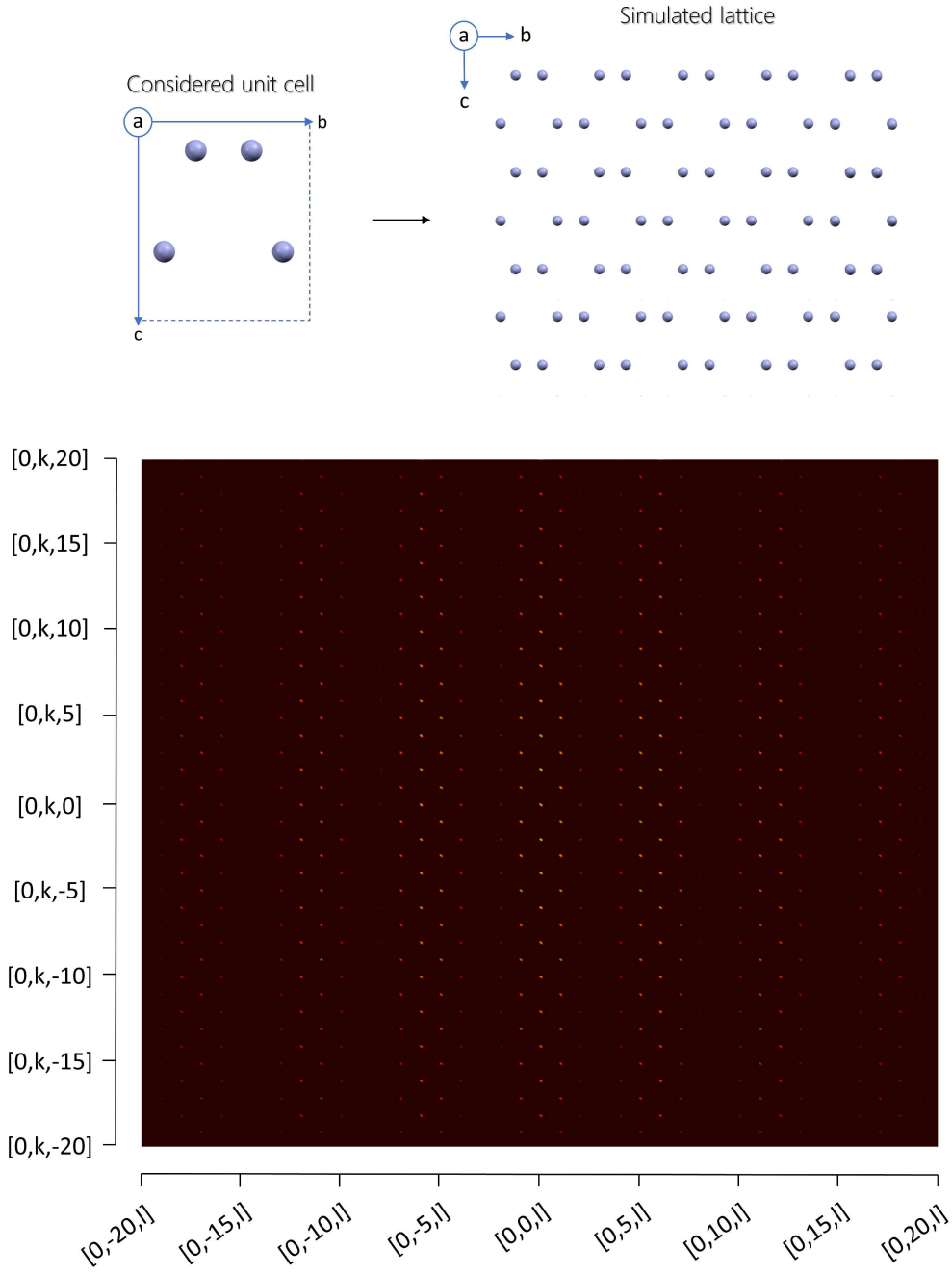

Figure 3.14. Calculated (0,k,l) plane of modified version of IRMOF-9, where every SBU is replaced by a Zn atom. Above, the considered unit cell and a fraction of the simulated lattice viewed along the a crystallographic direction.

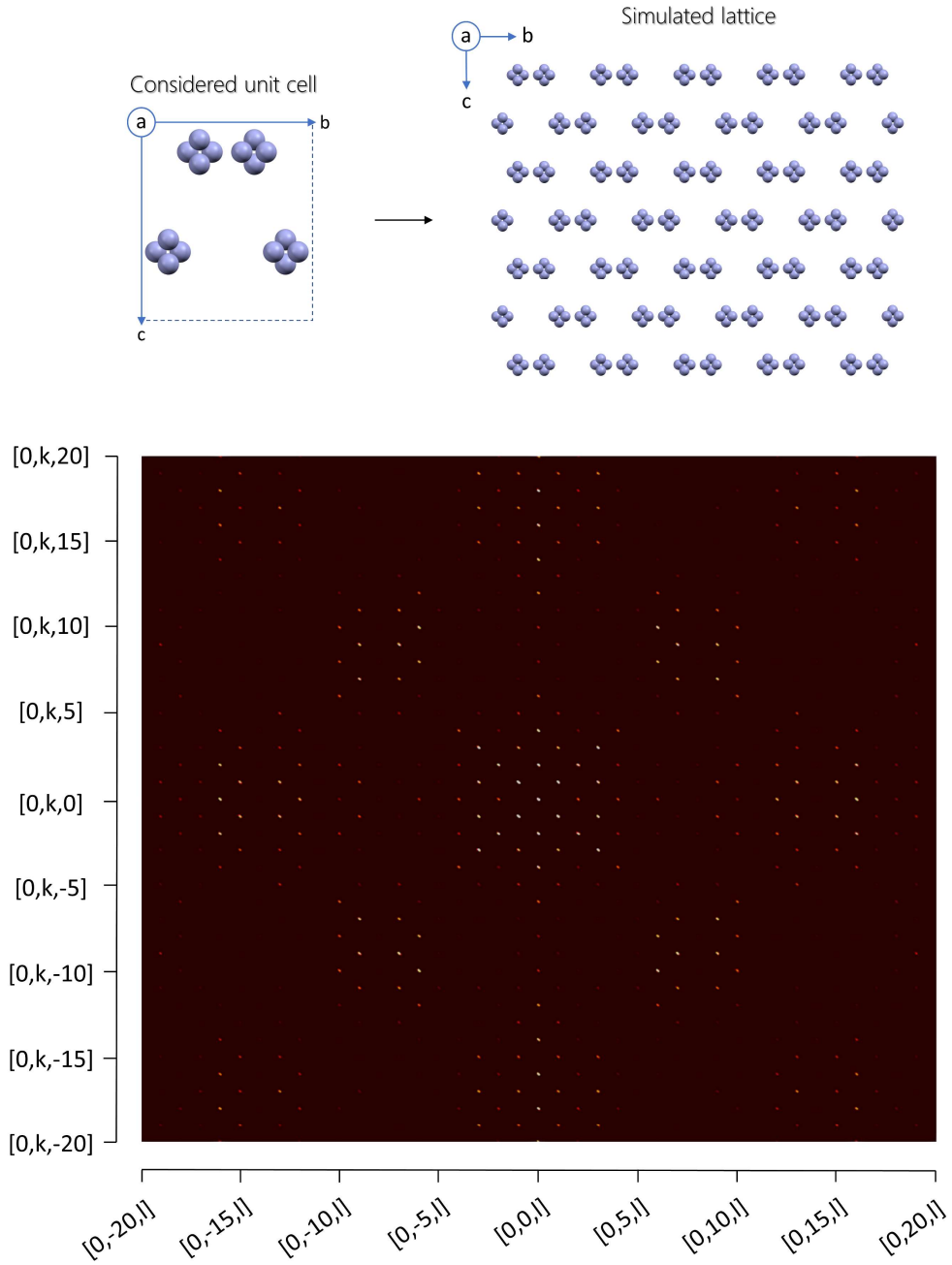

Figure 3.15. Calculated (0,k,l) plane of the reciprocal lattice of IRMOF-9 (only the SBUs are considered for the model). Above, the considered unit cell and a fraction of the simulated lattice viewed along the a crystallographic direction.

3.3.3.3 · Simulations results for TiO_x@IRMOF-9

Two disorder models have been tested, starting from the first and second hypotheses formulated in paragraph 3.3.1.2. In the following simulations, the space group symmetry is lowered from Pnnm to P1. This choice has been adopted to have more flexibility in the ZODS input file compiling and testing different degrees of correlation in the movements of the four SBUs present in the unit cell.

The first set of simulations considered the correlated movement of the networks to resemble a breathing-like deformation. For this purpose, the four different SBUs in the unit cell have been considered separately (Figure 3.16). These SBUs can be grouped into two pairs, α and β, so that each pair belongs to one of the two interpenetrating networks. Each pair forms a rhombus-shaped cavity with the ones of the same type belonging to adjacent unit cells. By defining these chemical units, it is possible to simulate the elongation or enlargement of the cavity just by instructing ZODS on the necessary correlated movement along the *b* and *c* directions of the four independent SBUs. If we define α^+ the elongation of the α rhombus and α^- its enlargement, and the analogue β^+ and β^- for the β rhombus, the resulting possible combinations are $\alpha^+\beta$, $\alpha\beta^+$, $\alpha^-\beta$, $\alpha\beta^-$, $\alpha^+\beta^+$ and $\alpha^-\beta^-$.

In the following simulations, + and – movements have been considered simultaneously because both elongations and enlargements cause the same disorder type and yield the same diffuse scattering effects. Accordingly, we will refer to these displacement types with the ± symbol. Since each SBU pair type (α or β) is symmetry equivalent with the other one, the combination $\alpha^\pm\beta$ is equal to $\alpha\beta^\pm$ and the corresponding diffraction patterns are identical. Therefore, only one of the two types of displacements will be shown and discussed.

The first simulation tests the $\alpha^\pm\beta$ type of disorder (Figure 3.17, top). The resulting diffuse scattering respects the intensity modulation due to the SBU structure, but not the one caused by the interpenetration (Figure 3.17). As a matter of facts, no vertical stripes of intensities can be found in the (0,k,l) plane and this is because the introduced disorder model does not include the peculiar correlation between the SBUs caused by the interpenetration, i.e., the relative position of the SBUs in each SBU pair. This disorder model causes the loss of such a geometry and the appearance of diffuse points between the lattice planes, together with weak diffuse lines along the *b** and *c** directions for high h:l and l:h absolute values respectively.

By introducing correlation in the SBU pairs adopting the $\alpha^\pm\beta^\pm$ displacement type, the disorder model keeps the SBU pairs unchanged and the intensity modulations present in the TiO_xIRMOF-9 experimental pattern are fairly reproduced (Figure 3.18).

Again, the diffuse intensities are localised between the Bragg spots, thus simulating a supercell of the underlying lattice. This effect can be attributed to the presence of an $\alpha^+\beta^+\alpha^-\beta^-\alpha^+\beta^+\alpha^-\beta^-$ alternation in the *b* and *c* crystallographic directions, as consequence of the +-+- correlated displacement, inherently present in the model.
By avoiding this alternation and isolating the $\alpha^+\beta^+$ and $\alpha^-\beta^-$ displacements in the crystal, the resulting diffuse intensities do not feature any distinguishable correlation, with the only exception of the intensity modulations effects (Figure 3.19).

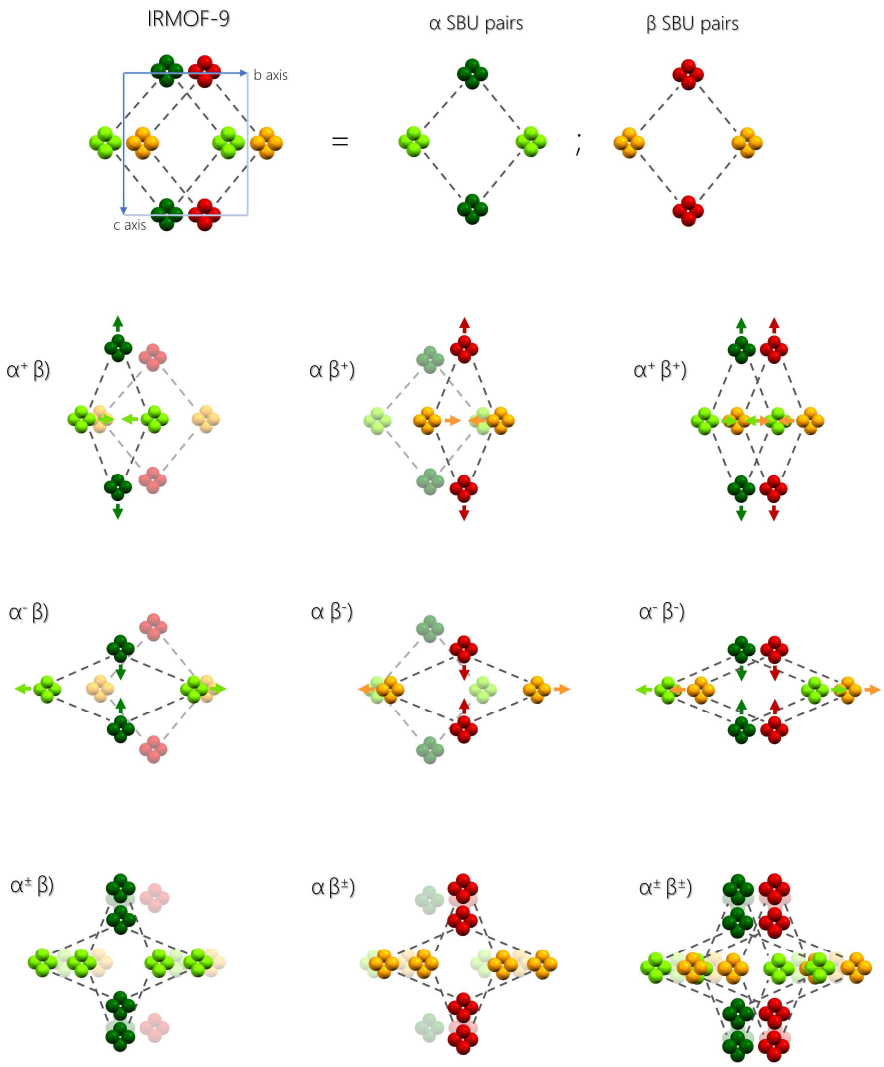

Figure 3.16. Scheme of the considered displacement types simulating the MOF breathing movement.

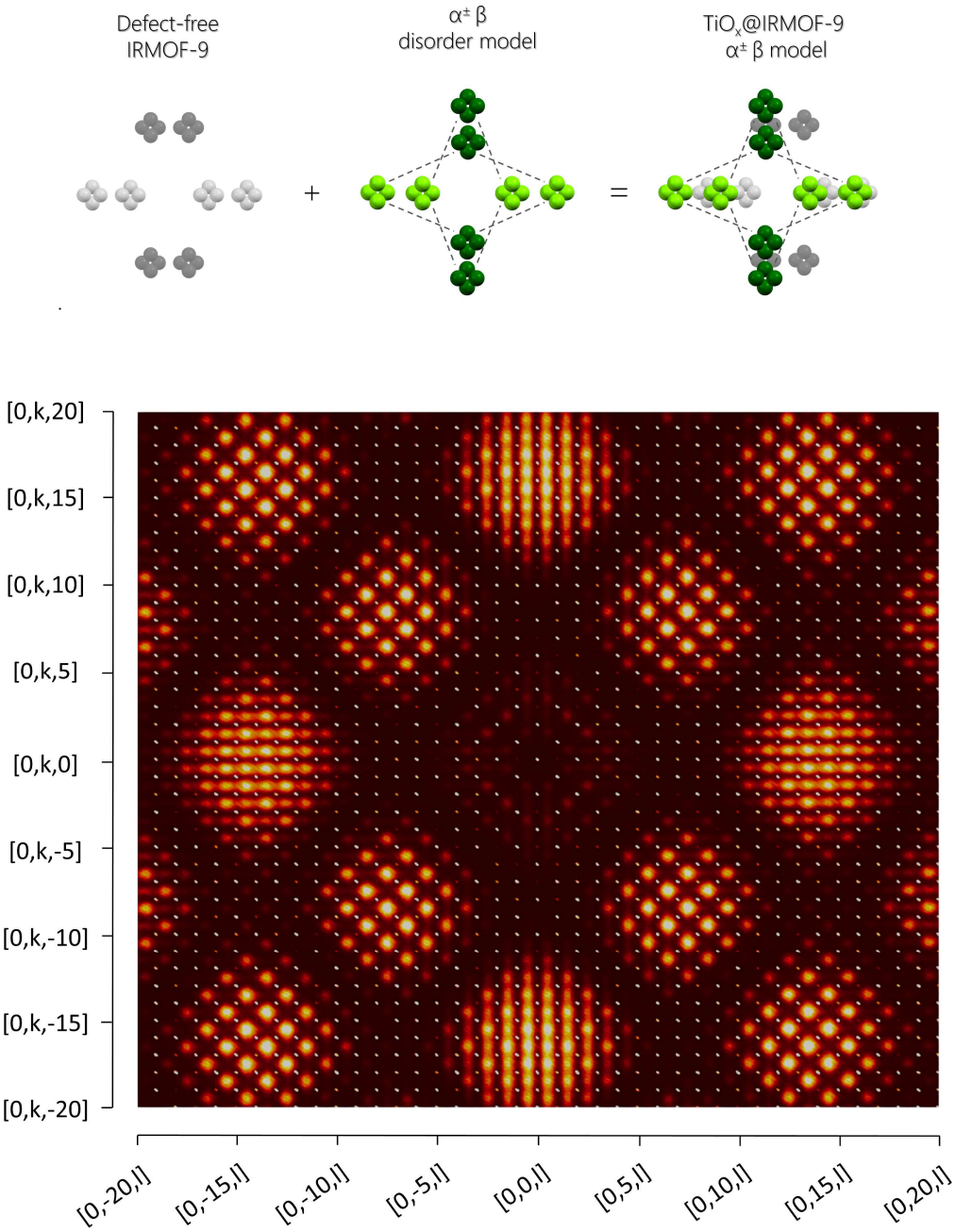

Figure 3.17. Above, the α±β disorder model is applied on the average IRMOF-9 structure, displayed in grey scale. Below, the TiO_x@IRMOF-9 α±β model simulated diffraction pattern.

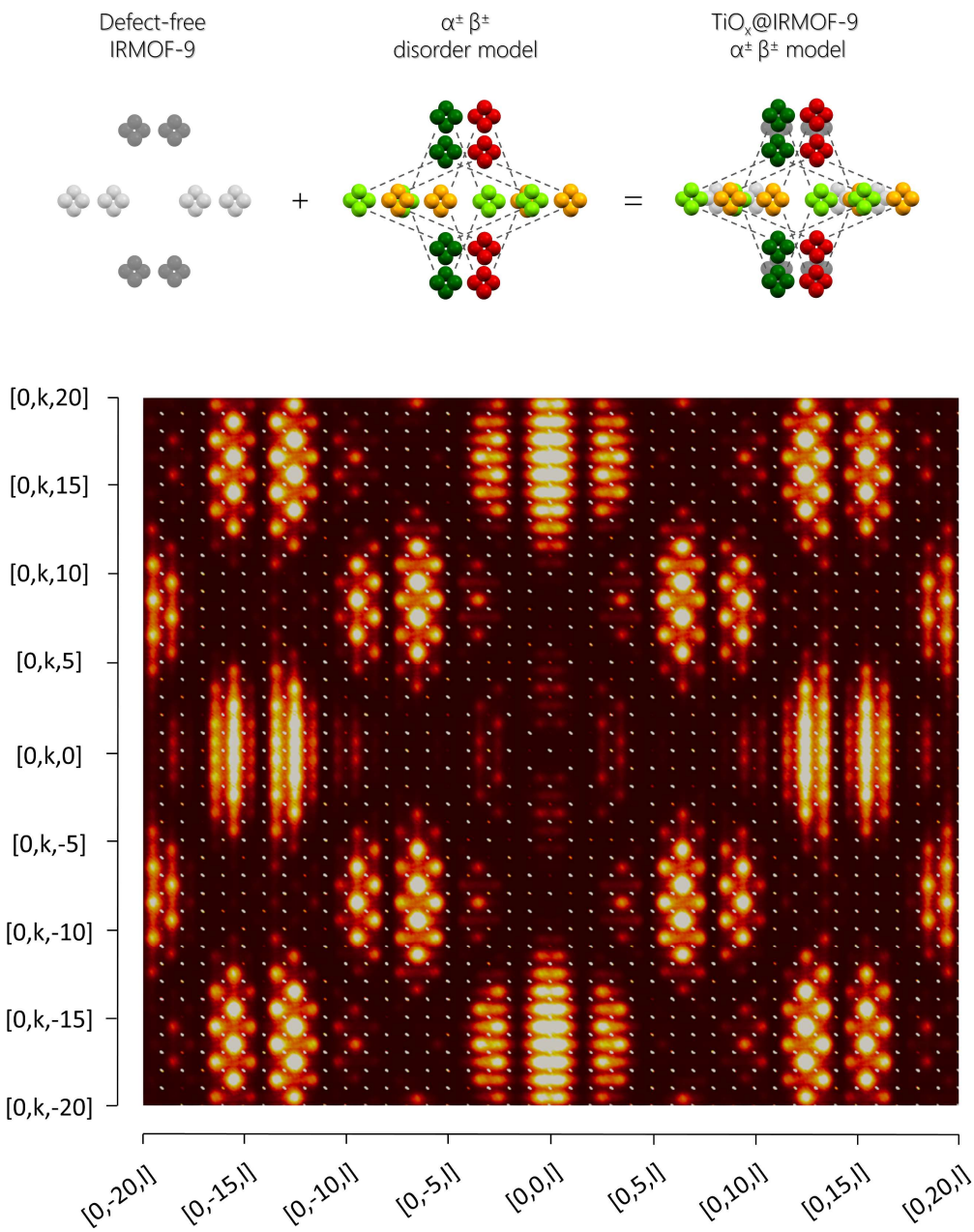

Figure 3.18. *Above, the α±β± disorder model is applied on the average IRMOF-9 structure, displayed in grey scale. Below, the TiO_x@IRMOF-9 α±β± model simulated diffraction pattern.*

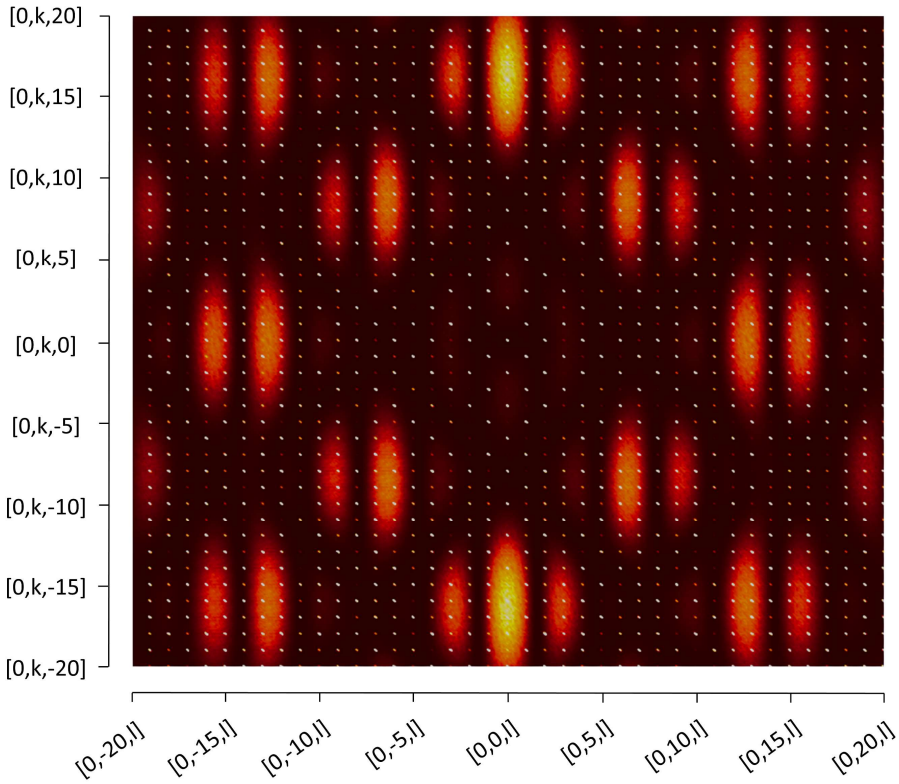

Figure 3.19. Simulation of diffraction pattern resulting from the $\alpha^{\pm}\beta^{\pm}$ disorder model, in which the $\alpha^{+}\beta^{+}$ and the $\alpha^{-}\beta^{-}$ movements are kept isolated throughout the crystalline domain.

One last simulation concerning the first disorder hypothesis considered the $\alpha^{\pm}\beta^{\pm}$ movement of only the upper-left half of the quadrangular chemical assembly (Figure 3.20, top). This test verifies the hypothesis that the cavities deform in a less-correlate way, and some coordinative bonds are broken so that the SBU pairs move without respecting the symmetry of the voids along the *a* direction. This results in diffuse lines running along the *b**-*c** direction (Figure 3.20). Although the directionality and position of the diffuse intensities reproduce qualitatively the experimental one, this is true only for two quarters of the reciprocal space and the pmm symmetry of the experimental total scattering pattern is not reproduced. By simulating the same disorder type along the two diagonals of the reciprocal space, and isolating the two events, it would be possible to have the sum of the two effects. However, this would result in diffuse crosses, which in the experimental pattern are only observed in reciprocal space zones with h:l ratios close to +0.5 and -0.5.

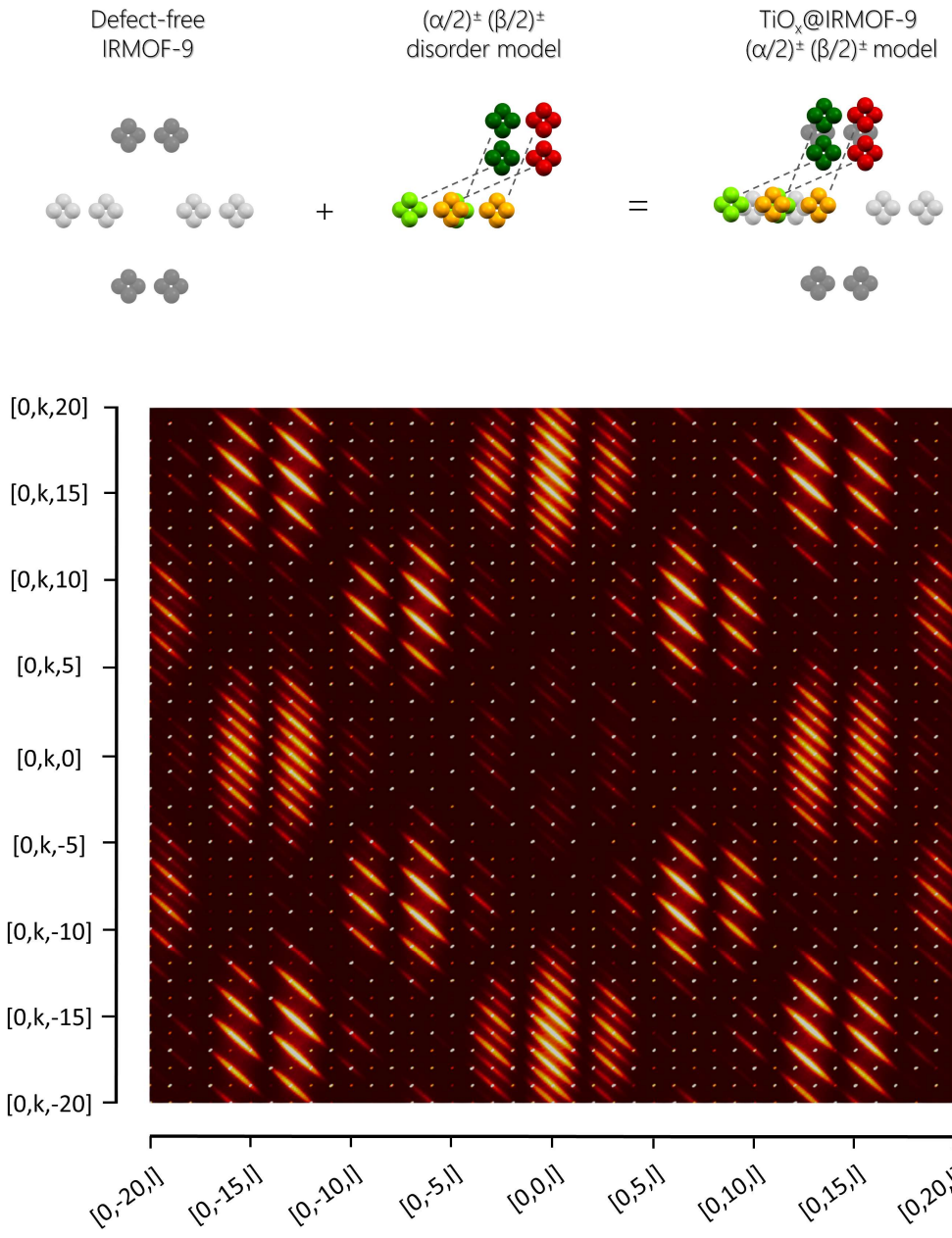

Figure 3.20. Above, the (α/2)±(β/2)± disorder model is applied on the average IRMOF-9 structure, displayed in grey scale. Below, the TiO_x@IRMOF-9 (α/2)±(β/2)± model simulated diffraction pattern.

To test the second hypothesis, which considers the framework positional disorder along *b*+*c* and *b*-*c* as the main cause for the diffuse scattering, the displacements of SBUs along these directions have been simulated. In this case, the chemical unit consists in SBUs grouped in pairs to avoid the loss of their typical intensity modulation.

Two cases have been investigated: the independent movement of the SBU pairs, and a correlated movement consisting in a rigid displacement of a SBU quartet made of two adjacent SBU pairs lying on a diagonal of the unit cell (Figure 3.21).

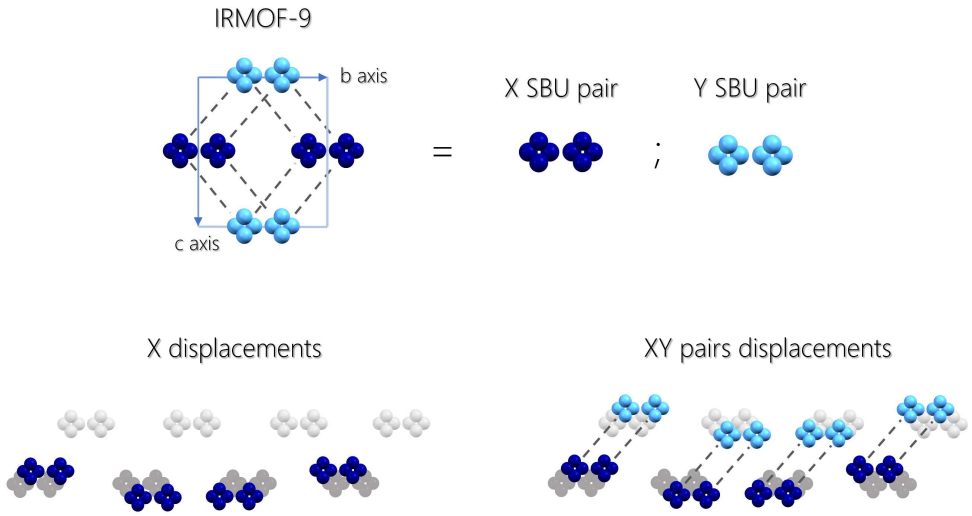

Figure 3.21. Chemical units (X and Y) and displacement types adopted to test the second hypothesis.

Not surprisingly, the correlation-free displacement of individual SBU pairs resulted in a diffraction pattern identical to that of Figure 3.19. On the contrary, the calculated pattern relative to the second case (Figure 3.22) is significantly close to the experimental TiO_xIRMOF-9 one. The diffuse lines and crosses are in the correct regions, although the diffuse intensities are still broad and not centred on the Bragg reflections.

By extending this correlation to the first-neighbours along the quartets diagonal, these quartets are paired in octuplets, and the resulting diffuse intensities are remarkably sharper, although remaining uniformly distributed along the *b**+*c** and *b**-*c** directions (Figure 3.23).

At this point, two possibilities are considered: these displacements can be equally distributed in the crystal, or they can be grouped along the *b* and *c* directions.
The first case leads to the concentration of the diffuse intensity between the Bragg reflections (Figure 3.24). This is because by creating an alternation of disordered and ordered unit cells along a certain vector, a super-cell forms in that direction.
On the other hand, if the displacements are clustered, the diffuse intensities are much closer to the experimental ones (Figure 3.25).
The final agreement (Figure 3.26) can be considered satisfactory, leaving behind mainly quantitative intensity issues and the slightly asymmetrical shape of the Bragg peaks tail, which varies from sample to sample. Overall, the model reproduces the general features of the experimental diffuse scattering, thus validating the second hypothesis.

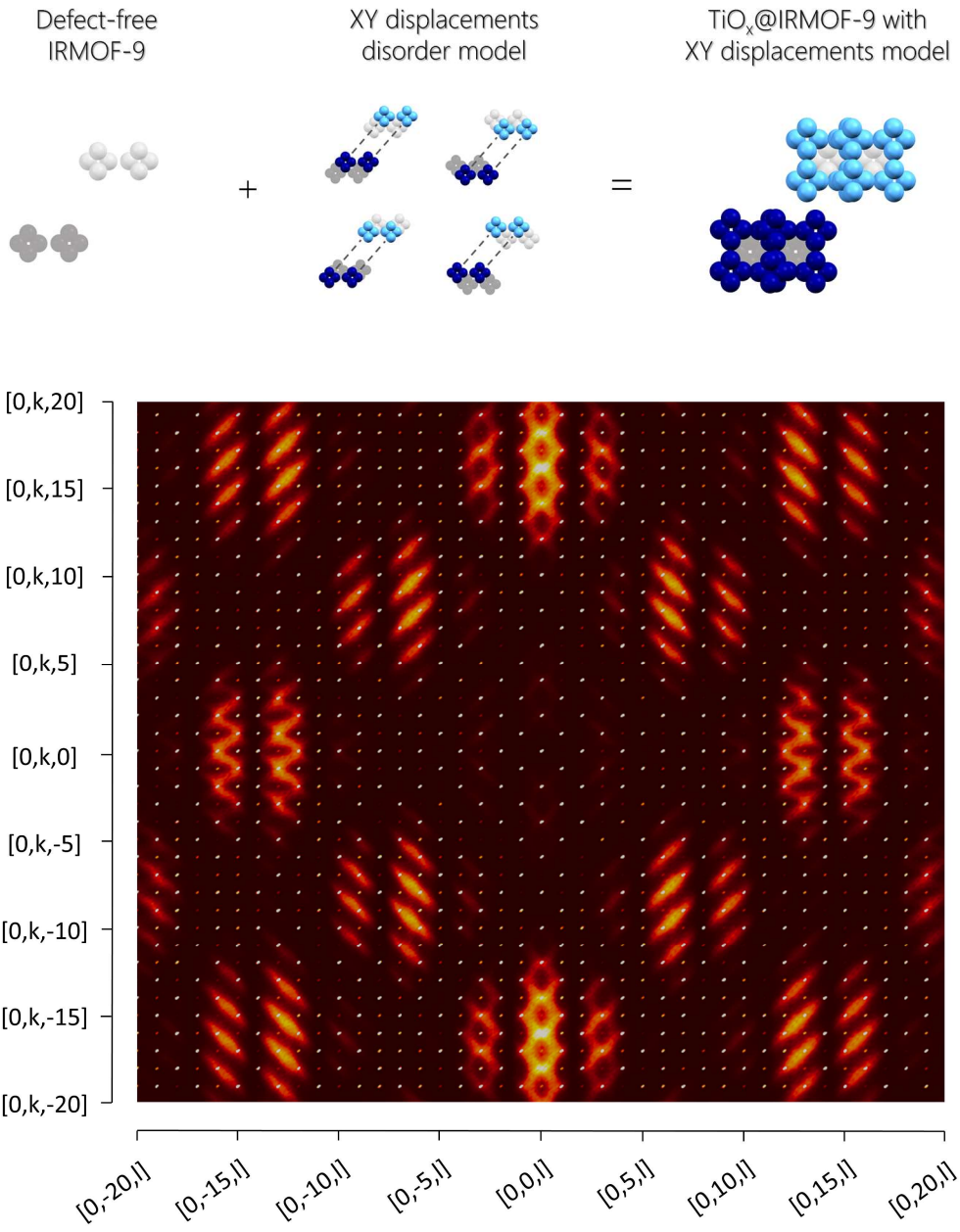

Figure 3.22. Simulation of the diffraction pattern resulting from the diagonal shift of SBU quartets. Above, the disorder model is explained; below, the resulting simulated XRD pattern is displayed.

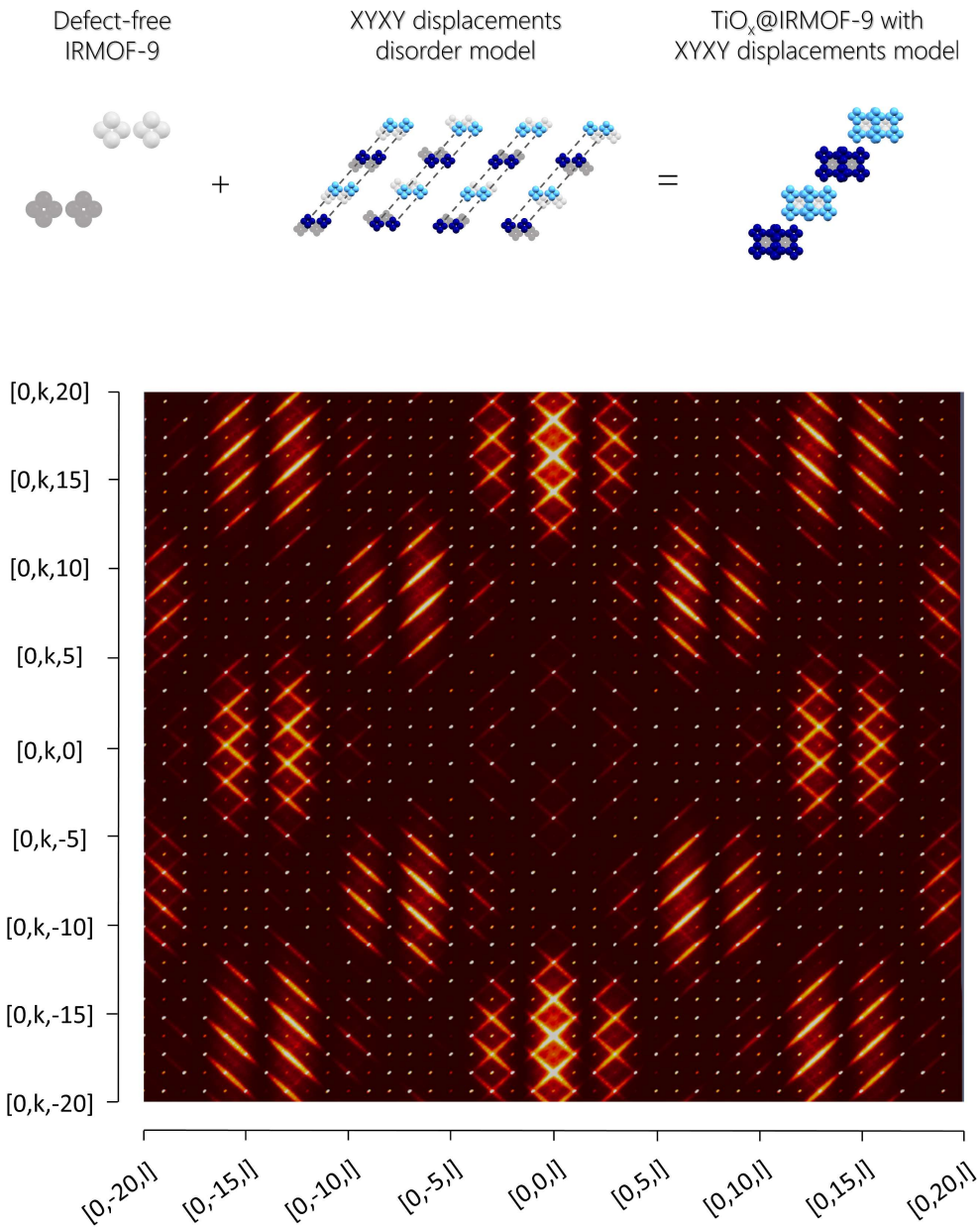

Figure 3.23. *Simulation of the diffraction pattern resulting from the diagonal shift of SBU octuplets. Above, the disorder model is explained; below, the resulting simulated XRD pattern is displayed.*

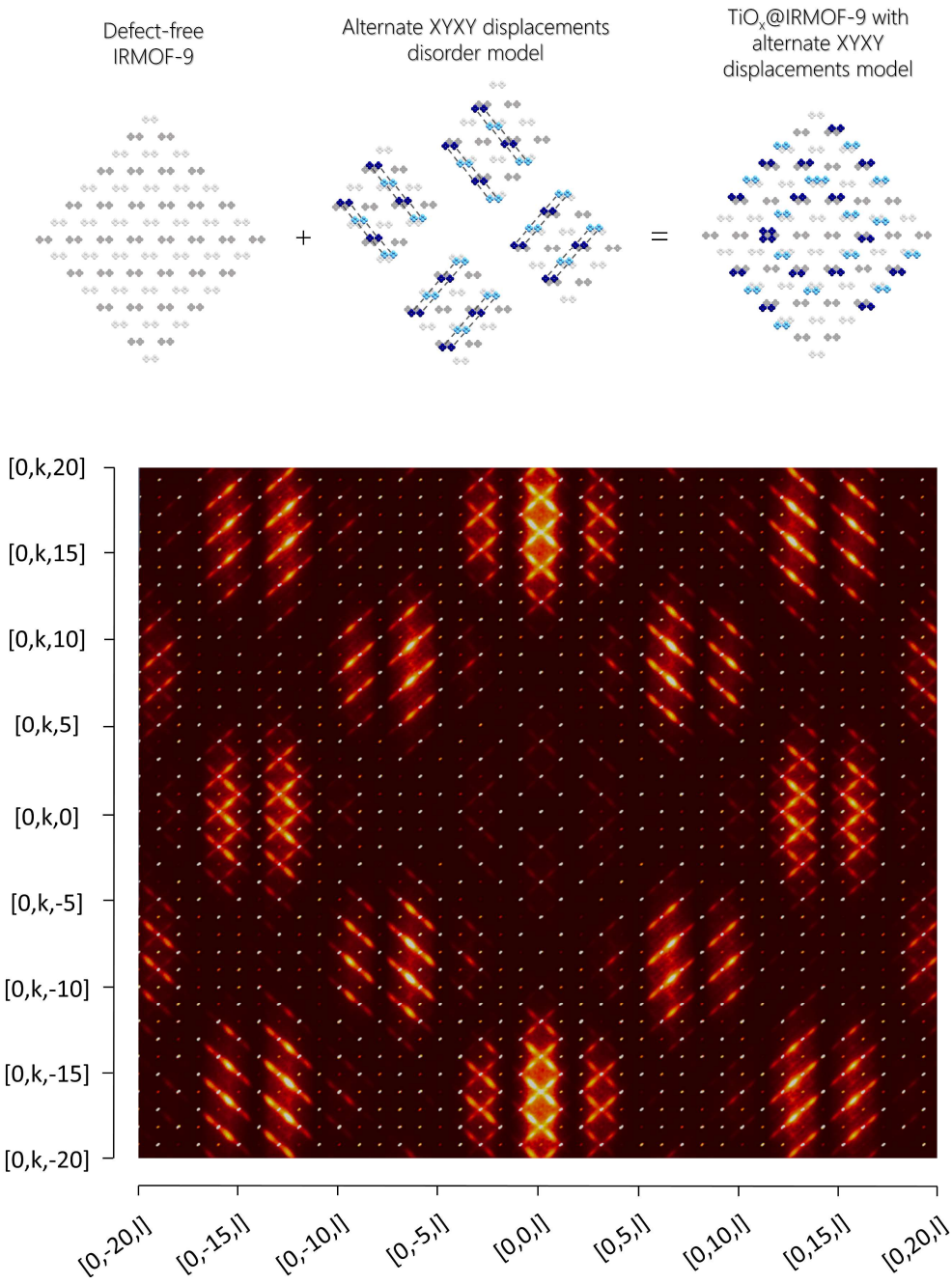

Figure 3.24. Simulation of the diffraction pattern resulting from the alternate diagonal shifts of SBU octuplets. Above, the disorder model is explained; below, the resulting simulated XRD pattern is displayed.

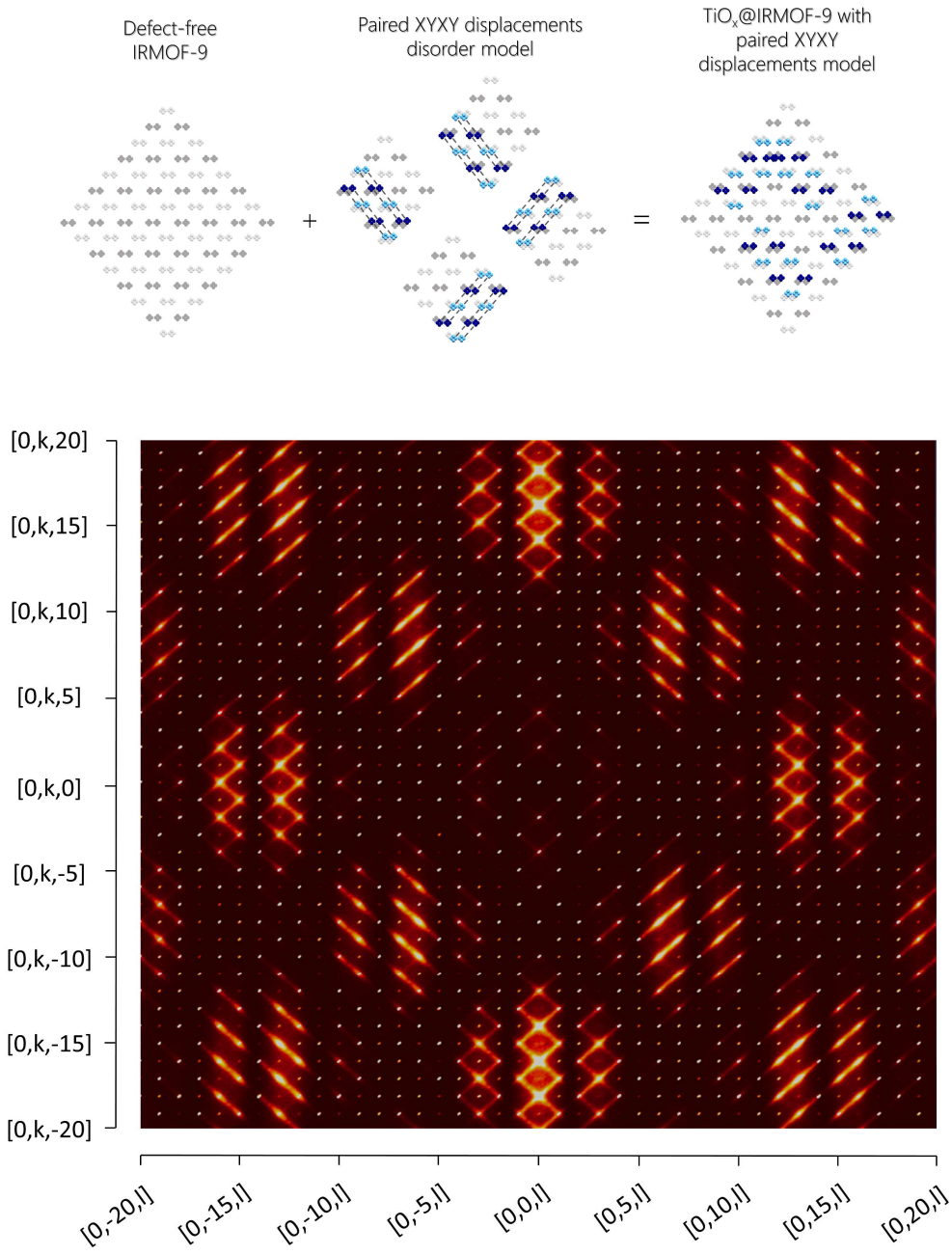

Figure 3.25. Simulation of the diffraction pattern resulting from the diagonal shifts of paired SBU octuplets. Above, the disorder model is explained; below, the resulting simulated XRD pattern is displayed.

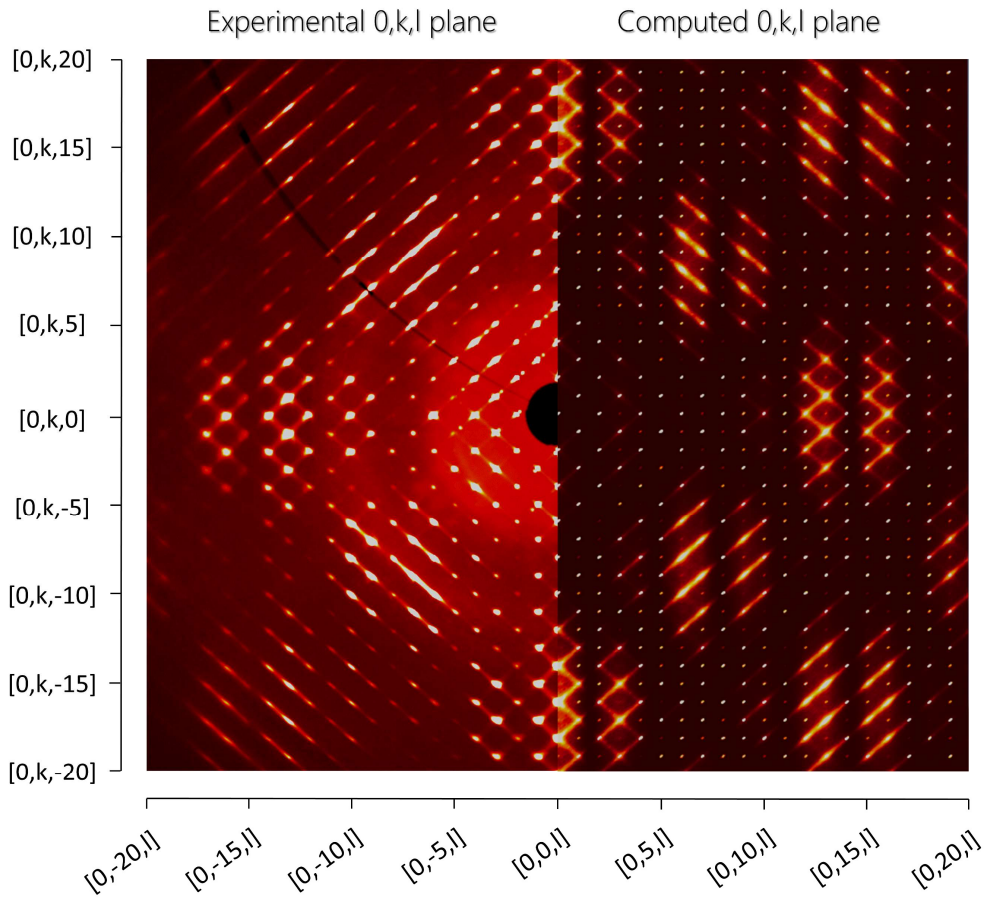

Figure 3.26. *Comparison between the TiO_x@IRMOF-9 experimental diffraction pattern and the calculated one according to the last discussed disorder model.*

3.4 · Final considerations on TiO_x@IRMOF-9 structure

The simulations suggest displacements along the *b*+*c* and *b*-*c* directions as the main type of disorder affecting TiO_x@IRMOF-9. These displacements involve parallel chains of SBU and linkers moving together towards and away from the average positions. This double direction can be deduced by the Bragg structure analysis, which showed the simultaneous presence of both displacements in every analysed sample.

The reason for these displacements remains less certain. In this regard, another important piece of information provided by the Bragg analyses is the presence of titanium oxo-clusters embedded in one of the solid phases. Their presence is likely to be found also in the other samples due to the same treatment they were subjected to.

The formation of such aggregates could have two opposite effects on the crystals.

First: the unit cells can be deformed by the growing objects, thus causing the correlated displacements at issue. On the other hand, as supposed in chapter I (paragraph 1.3), IRMOF-9 needs a coordinating solvent to keep its pores geometry, and by replacing DMF with $Ti(iPrO)_4$ this condition is not satisfied. Therefore, the cavities readily shrink, but in the meanwhile the oxo-clusters have formed and, depending on their size and position, limit this contraction.

While the first effect includes the possibility of unit cell enlargements, which are likely if growing aggregates pushes the closest SBU pairs in the cavities, the second one only considers the contraction of the cavities. Here, the first clue provided by Bragg analyses comes in useful, since the analysed TiO_x@IRMOF-9 samples unit cells are remarkably narrower than those of IRMOF-9.

From these considerations, the following scenario can be reconstructed: as IRMOF-9 crystals are soaked in $Ti(iPrO)_4$, the DMF molecules present in the solid are exchanged with $Ti(iPrO)_4$ starting from the outer layers of the crystals. As soon as the alkoxide enters in the solid, it encounters water molecules present in traces inside the channels.

The subsequent hydrolysis causes the partial growth of titanium oxo-clusters and, potentially, the formation of Ti-O-Zn bridges keeping these clusters bound to the MOF. At the same time, since DMF molecules have been replaced by $Ti(iPrO)_4$, no fluxional solvent coordination prevents the cavities from collapsing. This effect might be partially limited by the release of iPrOH due to the $Ti(iPrO)_4$ hydrolysis.

Water molecules are consumed by such a hydrolysis, and it becomes reasonable to envisage that the size of the titanium-oxo-cluster depends on the amount of water present in different areas of the framework.

Different sized aggregates oppose differently to the collapsing MOF. Moreover, this effect is not symmetrical because the aggregates do not grow floating in the middle of the cavity, but in certain regions. The cavities contraction limited by the presence of different sized oxo-aggregates causes displacements of SBU-linker-SBU units, and the position of the aggregates in each cavity causes the asymmetricity of these displacements with respect to the starting unit cell. Adjacent unit cells are affected in a domino effect, and this causes the strong correlation deduced by the diffuse scattering analyses and confirmed by ZODS simulations.

3.5 · Concluding remarks

The analysis of the crystals structural complexity afforded more than a mere understanding of the final solid structure. The acquired information underlined the importance of water traces in the starting solid or any other presence causing the partial hydrolysis of the incoming precursor. Indeed, if IRMOF-9 were deprived of this presence before the soaking treatment, the DMF-to-$Ti(iPrO)_4$ exchange would likely result in the collapse of the solid as in the cases of soaking in DCM (paragraph 1.2.2, Chapter I), and no TiO_x@IRMOF-9 material would form. This highlights the importance of a control over water concentration when this synthetic approach is used.

This amount is limited by the IRMOF-9 instability due to hydrolysis of the linker-SBU building units discussed in Chapter I (paragraph 1.2.2.1). On the other hand, by tuning the concentration of water molecules inside the MOF (e.g., by soaking in a DMF/H_2O mixture with a pre-defined ratio before the soaking in $Ti(iPrO)_4$), it might be possible to limit the hydrolysis of the precursor and thus the size of the achievable aggregate.

In principle, by following another synthetic approach, a less flexible MOF could be used. In this case it would be possible to fill its pores with $Ti(iPrO)_4$ in dry conditions without the perspective of a MOF collapse. Then, the hydrolysis should be triggered from the outside, for instance, by exposing the filled MOF to moisture. However, this approach would likely result in a partial $Ti(iPrO)_4$ conversion, since only the surface layers of the solid would be in contact with water molecules and the pores would be therefore sealed, thus preventing more water to enter in the inner regions of the crystal.

· Addendum ·

Parallel project:

Methylene blue complexes

"There is no blue without yellow and without orange,
and if you put in blue, then you must put in yellow, and orange too,
mustn't you?"

Vincent Van Gogh

"Letters to Emile Bernard"
1888

Canossa, S. et al, *Inorg. Chem.*, **2017**, 56(6), 3512-3516

a.1 · Introducing Methylene blue

Methylene blue (**MB**) is dark green salt with formula $[(C_{16}H_{18}SN_3)^+Cl^-]$ (IUPAC name: 3,7-bis(dimethylamino)-phenothiazin-5-ium chloride). Its cation, **MB⁺**, consists of three condensed six-membered rings and two terminal coplanar -NMe_2 groups. The cationic system is aromatic and the delocalisation involves 18 p^{π} electrons distributed on the whole molecule, with exception of the terminal methyl groups (Scheme a.1).

A visualisation of MB^+ molecular orbitals (MO)[104] suggests a weak σ donor for the central N atom, given that its in-plane σ lone pair lies below the frontier MO region. The LUMO is instead an accessible π* level, which affords an amidic N atom upon reduction. In this case, aromaticity is lost and the entire system is puckered, but metal coordination through the N atom is facilitated[105,106], as a consequence of the obtainment of N-H/N-R derivatives[107], which are also stable in a cationic form[108,109].

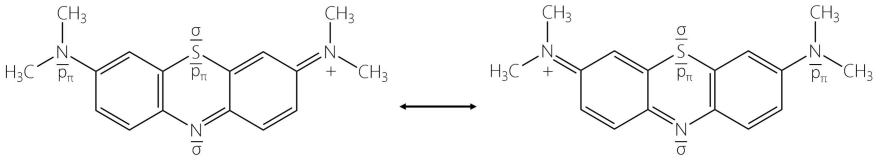

Scheme a.1. The resonant structures of MB^+ are represented highlighting the presence of the electron pairs at the heteroatoms, distinguished for their p_π or σ character.

a.1.1 · Common applications and the need for structural knowledge

Thanks to its reduction, which comes with the total loss of its intense blue colour, and to the capability of restoring its oxidation state by reacting with O_2 and oxidising agents with similar redox potentials[110], MB is widely used as an indicator. Further applications relying on its redox behaviour can be found in photocatalysis[111,112] and enzyme-catalysed redox reactions. Furthermore, MB has manifold employments in medicine, where is commonly used for the treatment of several diseases such as methemoglobinemia[113], cyanide[114,115] and carbon monoxide poisoning[115], malaria[116–118], and Alzheimer's[119].

In these fields, since transition metals are often involved in the mechanisms, a coordinative behaviour of MB could, in principle, have significant influences, although its coordination capabilities remain elusive in the literature. Moreover, the major available information regarding MB chemistry is limited to its properties in solution rather than in the solid state.

The only claimed example of a stable metal coordination has been reported by Raj et al[120], who described the crystal structure of $(MB)^+[HgCl_3]^-$, although the N···Hg distance of 2.779 Å exceeds the sum of the covalent radii as well as the average value from the Cambridge Structural Database[55].
The MB^+ coordination has also been invoked for square planar $[M(SCN)_4]^{2-}$ units (M=Co(II), Cu(II), Zn(II)) on the basis of spectroscopic data, although the change of color in the adduct seems more consistent with a redox process than metal coordination[121]. Finally, an interaction with the metal ion is proposed to occur on grafting MB over a polyurethane foam suited to sequester heavy metals. Again, no solid state characterization corroborates the feature[122].

a.2 · Synthesis of Methylene blue metal complexes

Aiming to obtain structural information regarding the solid-state interaction between MB and transition metals, several syntheses have been tackled by using MB chloride and ionic reagents of the desired metal. Given the strong tendency of MB towards aggregation by π-π stacking, its solutions rarely contain completely solvated and isolated MB ions[123]. Moreover, this strong self-interaction causes its scarce solubility in several common solvents. For these reasons, a **mechanochemical approach** (**grinding**, **kneading**) has been adopted by grinding together MB and the selected transition metal compound.
In order to push the syntheses towards the product phase, reagents have been selected so that the final product would result in a single phase featuring a single ion pair, or two phases, one of them being easily recognisable by XRPD. Thus, the performed reactions can be classified into two categories: reaction of MB chloride with metal chlorides, and with chlorometallate potassium salts. In the first case, the chloride ion coming from MB phase is expected to add to the coordination sphere of the metal centre. In the second case, the chlorometallate is already present in one of the two reactant phases, and the final product is expected to be a mixture of the product phase and KCl as by-product.
After the synthesis, the ground powder has been analysed by XRPD to confirm the outcome of the reaction and to verify its completeness. The resulting product phases have been therefore dissolved in suitable solvents and crystallisation trials by slow solvent evaporation or antisolvent-gel crystallisations have been set up to obtain single crystal specimens for SCXRD structural analyses. In cases where no single crystals have been obtained, the structure solution and refinement has been performed using the XRPD data.

In total, 16 phases containing MB and metal ions have been synthesized and characterised by XRD. Among these, two phases containing a non-transition metal (Sn) are also present. Two are the main behaviours exhibited by MB in the obtained solid phases. First, its strong typical π-π stacking, which forms dimers or pillars depending on the geometric and electronic features of the counter-anion. The second commonly found interaction is the network of H-bonds that MB forms acting mainly as donor by employing its methyl or aromatic C-H groups.

Remarkably, in two solid phases (figure a.1) MB participate in the coordination of a metal centre, together with two chloride ions. These metals are a copper(I) and a silver(I), and the two phases, **MBCu** (CCDC 1475865[55]) and **MBAg** (CCDC 1475866[55]), obtained as orangish gold needles, are isostructural and are only obtainable by mechanochemical synthesis. In facts, every attempt of their synthesis in solution failed, and NMR and Mass Spectrometry analyses did not provide any proof of these complexes presence in solution.

Another phase with identical composition, but with the presence of gold as metal species was been also obtained. However, in this case, no coordination bond is present and the phase consists in a close packing of MB^+ and $AuCl_2^-$ ions (CCDC 1481894[55]). Since the obtainment of MB metal complexes constitutes the main aim of the present work, the following discussion will focus on these two phases and the analysis of the adduct they are composed of.

Metal	Phase composition	Metal	Phase composition
Co(II)	$(MB)_2[CoCl_4]\cdot H_2O$	Sn(IV)	$(MB)_2[SnCl_6]$
Ni(II)	$(MB)_2[NiCl_4]\cdot H_2O$	Pt(II)	$(MB)_2[PtCl_4]$
Cu(I)	**$[(MB)CuCl_2]$**	Au(I)	$(MB)[AuCl_2]$
Cu(II)	$(MB)_2[CuCl_4]$	Au(III)	$(MB)[AuCl_4]$; $(MB)[AuCl_4]\cdot CH_2Cl_2$
Zn(II)	$(MB)_2[ZnCl_4]\cdot H_2O$	Hg(I)	$(MB)[HgCl_3]$; $(MB)[HgCl_3]\cdot CH_3NO_2$
Ag(I)	**$[(MB)AgCl_2]$**	Hg(II)	$(MB)_2[HgCl_4]\cdot H_2O$
Sn(II)	$(MB)_2[SnCl_4]\cdot H_2O$	La(III)	$(MB)_2[La(H_2O)_9]Cl_5\cdot 3H_2O$

Table a.1. *Summary table of the obtained and structurally determined compounds featuring MB and metal species. Among these, two coordination compounds have been obtained, indicated in bold.*

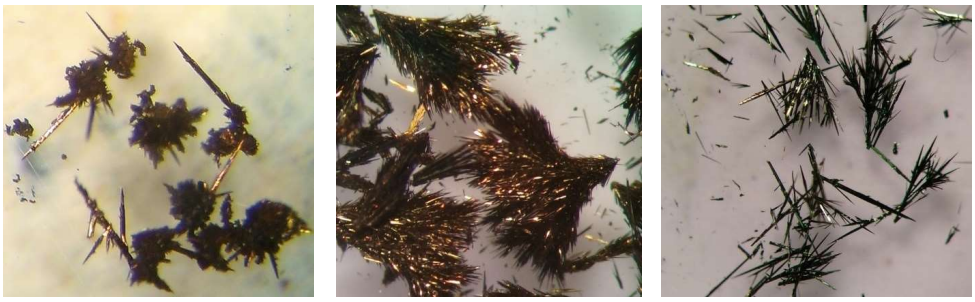

Figure a.1. From the left, crystals of [(MB)$CuCl_2$], [(MB)$AgCl_2$] and (MB)[$AuCl_2$], whose attainment is described in section A.1, Appendix.

a.3 · Structural considerations

In both complexes the metal features an approximate trigonal-planar coordination geometry, in which the ligand role is played by two chloride anions and one MB^+, which donate its lone pair present on the central aromatic N atom (Figure a.2, a).

This behaviour is rather rare for cationic ligands, which hardly form uncharged metal complexes[124–127]. The N-metal bond is corroborated by the relatively short N-Cu/Ag bond distances, which amounts to 1.987(4) and 2.329(5) Å in the case of copper and silver respectively.

The Ag coordination can be considered less effective because the N–Ag bond is larger than the sum of the covalent radii and the average value from all of the corresponding CCDC structures[55]. The point is also supported by the more open Cl–Ag–Cl angle (119.48° vs 113.73°). The corresponding τ rotation of MCl_2 about the N–M linkage has intermediate values of 75.2 and 66.8° for MBCu and MBAg, respectively (table a.2).

Another important parameter concerns the out-of-plane shift of the metal from the MB^+ plane, which is almost equivalent in the two complexes (angles 11.8° and 9.5°). However, τ influences the extended heap formed by the parallel MB^+ units in an alternating head-to-tail π-π stacking. First of all, this arrangement is offset, being each complex unit slid by a half-condensed ring. In this manner, the atoms belonging to adjacent MB do not eclipse each other. Conversely, the MCl_2 rotation shortens the contact between any Cl atom and one H–C group of one adjacent MB. This allows a network of hydrogen-bonding interactions, which provides an additional stabilisation of the heap. On the other hand, the latter cannot be pairwise equivalent, since the θ deviation favours one Cl···H–C interaction with respect to the subsequent one. This can be easily verified by considering the Cl···H

distances, which are 2.614 and 2.89 Å in the case of MBCu and 2.622 and 2.816 Å in the case of MBAg. The most important consequence is that the constituent building block of the stacking heap is not a single complex, but rather a dimer of complexes.
Based on these considerations, two are the recognisable dimers in the stacking pillar (Figure a.2, c). The stacking distances of the resulting dimers are 3.506 vs 3.403 Å and 3.485 vs 3.307 Å for MBCu and MBAg, respectively. Remarkably, the dimer with the lower stacking distance (n°1 in Figure a.2, c) is the one with larger Cl···H–C contacts. This suggests an inverse correlation between the two main supramolecular forces keeping the solid phase building block integer (π–π and hydrogen bonding).

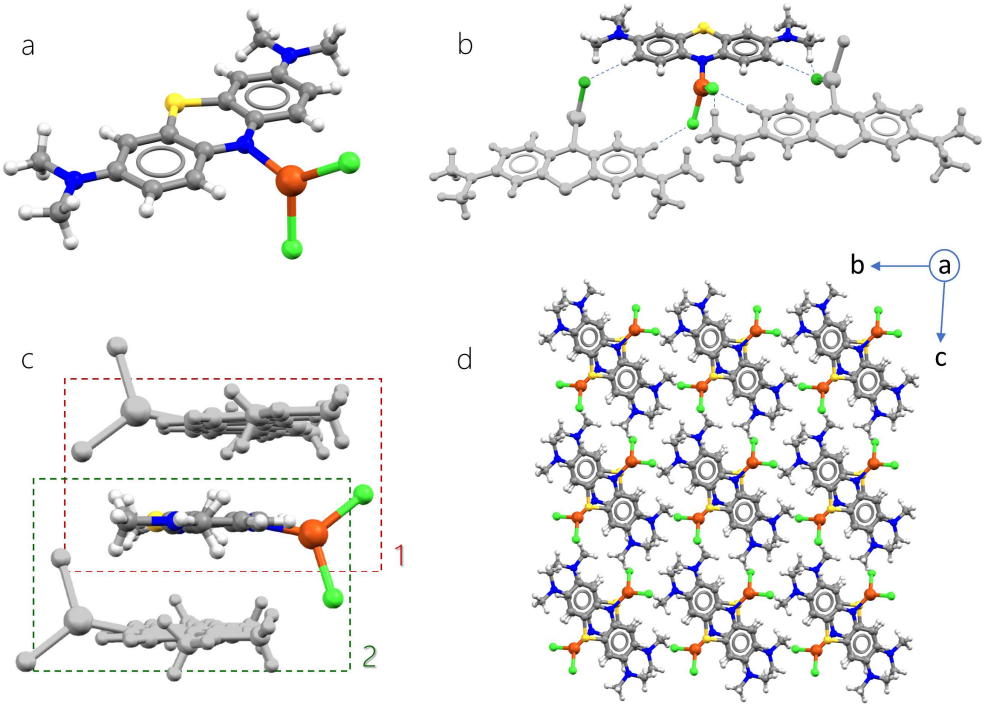

Figure a.2. Some structural features of [(MB)CuCl$_2$] phase, isostructural with [(MB)AgCl$_2$]. From the upper left corner, the [(MB)CuCl$_2$] complex unit (a) and its main supramolecular interactions (b, c) are displayed, together with the view of the crystal packing along the a crystallographic direction, along the stacking pillars axis. In (c), the two stacking dimer types are highlighted with differently coloured squares.

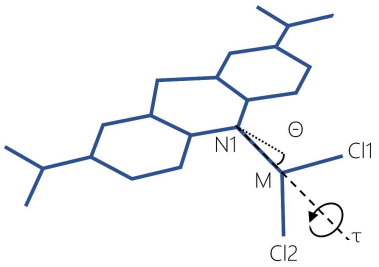

Parameter	Values for $MBCuCl_2$	Values for $MBAgCl_2$
M1-Cl1 (Å)	2.2220(5)	2.4425(19)
M1-Cl2 (Å)	2.2494(5)	2.4659(18)
N1-M1 (Å)	1.9874(13)	2.329(5)
Cl1-M1-Cl2 (°)	113.739(18)	119.48(6)
Cl1-M1-N1 (°)	129.45(4)	125.09(13)
Cl2-M1-N1 (°)	116.70(4)	15.32(13)
Θ (°)	11.8(4)	9.5(2)
τ (°)	75.2(2)	66.8(2)

Table a.2. Experimental geometric parameters of the two observed metal complexes.

a.4 · DFT calculations

DFT geometry optimisations have been performed on the two complexes, aiming to reproduce the observed coordination geometry observed in the solid state (Section A.10, Appendix).

Initially, the calculations were based on the molecular modelling of the single $[(MB)MCl_2]$ complexes (M=Cu, Ag) by adopting the B3LYP-DFT[128] method both in the gas phase and with solvation methods (CH_3Cl)[129].

Unfortunately, these optimizations resulted in a dramatic distortion of the trigonal-planar coordination geometry in the case of $[(MB)CuCl_2]$, whose N-Cu distance and Cl-Cu-Cl angle were overestimated by about +0.15 Å and +32° respectively, and the θ angle amounts to 49°.

In the case of $[(MB)AgCl_2]$, the situation is even worse since the coordinative bond is lost and the optimisation results in a $(MB)^+[AgCl_2]^-$ ion pair with a N···Ag distance of >6.0 Å and a Cl-Ag-Cl angle of 170°. This evidence corroborates the hypothesis that the supramolecular forces play a fundamental role in the occurring of the two complexes, as already supposed on the bases of spectroscopic data.

Further calculations have been performed in the solid state with the program CRYSTAL[130]. In a first attempt, the geometry optimisation has been performed on a single dimeric building block by adopting the B3LYP functional[128]. Again, unsatisfactory results were obtained, being the single complexes split in ion pairs. Thus, the dispersion correction present in the B97D functional[131] afforded an acceptable final geometry of the $[(MB)CuCl_2]$

dimer with two in-pointing N–Cu vectors, although with a θ angle of 23.8°, which shortens the Cl···H–C interactions (average value: 2.48 Å). The experimental value for θ (11°) is restored by introducing a third stacked complex and considering a trimer for the optimisation. This is true only for the middle complex, but not for the terminal ones (θ=16° and 29°). The geometry of the complex unit is acceptable (figure a.3), as well as the general arrangement of the heap, although with smaller and similar interplanar separations (3.10 and 3.06 Å).

To study this effect, likely attributable to dispersion forces, a new CRYSTAL optimization was attempted at the BLYP level. The arrangement thus obtained features a larger and more asymmetric interplanar separations of 3.41 and 3.30 Å. However, the rotation of each $CuCl_2$ fragment about the N–Cu linkage is in the opposite sense, resulting in a negative τ angle. As a consequence, the Cl–S contacts are preferentially shortened with respect to the Cl···H–C ones. This suggests a residual positive partial charge for the S atom.

The performed molecular and solid-state modelling provided useful information concerning the interaction energy between adjacent complexes. On average, attraction enthalpy is about −40 kcal·mol^{-1}, mainly due to dispersion forces. This agrees with the unsatisfactory results in the BLYP approach, where these contributions remain excluded and the interaction turns into a minor repulsion (∼+2 kcal mol^{-1}).

Therefore, π stacking overwhelms other contributions such as hydrogen-bonding or residual electrostatic attraction between differently charged counterions at different complexes, given that the components of the latter type are equally included in the two adopted functionals, although without any major evidence of their influence in the assembly of the complexes.

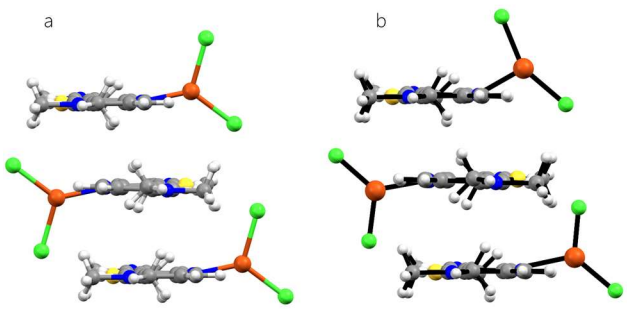

Parameter	Experimental values	Optimised values
M1-Cl1 (Å)	2.2220(5)	2.18
M1-Cl2 (Å)	2.2494(5)	2.19
N1-M1 (Å)	1.9874(13)	1.91
Cl1-M1-Cl2 (°)	113.739(18)	111.0
Cl1-M1-N1 (°)	129.45(4)	126.8
Cl2-M1-N1 (°)	116.70(4)	122.2
Θ (°)	11.8(4)	2.5
τ (°)	75.2(2)	57.6

Figure a.3. Comparison between the experimental complex trimer (a) and the DFT optimised one (b). The relative geometric parameters are reported in the table aside.

a.5 · Concluding remarks

The coordination capabilities of Methylene blue cation have been observed in the solid state for the first time. Given the manifold applications of this molecule in different areas of chemistry, medicine and biochemistry, this evidence could provide useful hints in the rationale of reaction mechanisms where MB is involved. Moreover, the reported synthetic procedure, stereochemistry and electronic underpinnings of the described systems might constitute a useful guideline in the search for other systems where MB or different analogues are associated with various metal centres.

Lastly, the reported systems constitute an unusual case of solid phases where the existence of the constituent building blocks, i.e., the metal complexes, relies on supramolecular forces rather than intramolecular bonding energies. This opposes to the common hierarchy of building blocks and supramolecular forces in molecular crystal engineering, which is based on the leading role of the constituent chemical species. These usually influence the crystal packing depending on the position and electronic features of their parts, and rule the crystal packing as consequence of their chemical structure. In the present case, on the contrary, the existence and the structure of the molecules constituting the phase are strongly dependent on the supramolecular forces holding them together in the crystal phase.

Appendix

A.1 · Synthetic procedures and post-synthetic treatments

All reagents and solvents were purchased by commercial sources and used as received. For gel preparations, an Agarose regent with the following specifications was used because of its optimal characteristics for the gel crystallisations experiments: ash≤0.25%, turbidity≤ 4 NTU (Nephelometric Turbidity Units), gel strength≥1800g·cm^{-2} (1% gel).

A.1.1 · Synthesis of IRMOF-9

100 of biphenyl-4,4'-diacrboxylate (0.41 mmol) were dissolved in 12 ml of N,N-dimethylformamide in a 15 ml glass tube placed at 383K in an oil bath. Therefore, 100 mg of $Zn(NO_3)_2 \cdot 6H_2O$ (0.37 mmol) were added to the solution. The tube was then sealed, shaken and left at 383K for 48 hours. The solution-gas interphase was kept slightly below the oil level, to limit the temperature inhomogeneities along the solution. Once the synthesis is over, the system was taken out of the oil bath and left to cool for 10-15 minutes. The crystals were then taken from the mother liquor, rinsed with N,N-dimethylformamide and preserved in the pure solvent.

A.1.2 · Soaking of IRMOF-9 in organic dyes solutions

IRMOF-9 crystals were taken and transferred in a solution prepared by dissolving 5 mg of the selected dye (Methylene blue or Rhodamine 101) in 3 ml N,N-dimethylformamide in a 5ml vial. The system is closed and left at room temperature for 14 days. After this time span, the crystals were taken and transferred in an oil droplet on a glass sleeve for the optical microscope evaluation. Each evaluated crystal was removed from solution droplets remained on its surface, cut in thirds perpendicular to its longer dimension, and the central part was rotated in order to expose the section to the observer. The pictures shown in Chapter II were captured with a 40x magnification.

A.1.3 · Synthesis of ZnBPDC1 and ZnBPDC2

The synthesis starts with the preparation of a "U" tube containing a 0.5% agarose gel. 50 mg of agarose were dissolved in 10ml H_2O at 363K. The solution thus obtained was used to fill the horizontal part of a glass "U" tube, and the system was left sealed with rubber septa for approximately 10 minutes to reach room temperature. Once the gel is formed in the glass tube, the right and left vertical chambers were filled with 1ml 0.07 mM aqueous

solution of Na_2BPDC and $Zn(NO_3)_2$ respectively, and the system was left to equilibrate by counter-diffusion. After one week, the described phases were formed and clearly recognisable.

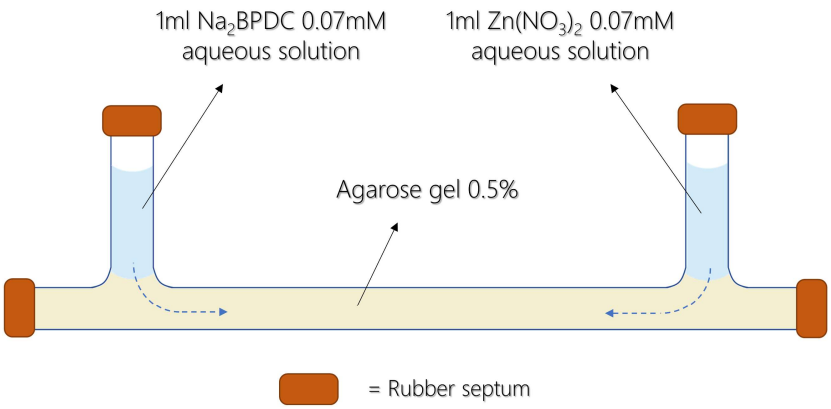

Figure A.1.1. Graphical simplification of the ZnBPDC1 and ZnBPDC2 synthetic procedure reported in paragraph A.1.3.

A.1.4 · Transmetalation of IRMOF-9 into Co-IRMOF-9

Crystals of IRMOF-9 were washed three times with fresh DMF and left in the pure solvent for 24 hours in a closed vial. Afterwards, the crystals were taken and covered with 3 ml of a 0.2 M DMF solution of anhydrous $CoCl_2$. The vial was closed and left for 30 days at room temperature; the soaking solution was changed every 7 days to push the transformation towards completeness. Then, crystals were taken out from the solution, washed three times with fresh DMF and left in 3 ml of pure solvent for 24 hours to remove residual $CoCl_2$ traces present in the pores.

A.1.5 · Transmetalation of Co-IRMOF-9 into IRMOF-9

Crystals of Co-IRMOF-9 were covered with 3 ml of a 0.2M DMF solution of $ZnCl_2$, in a closed vial. The system is kept for 30 days at 305K; the soaking solution was changed every 7 days to push the transformation towards completeness. Then, crystals were taken out, washed three times with fresh DMF and left in 3 ml of pure solvent for 24 hours to remove residual $ZnCl_2$ traces present in the pores.

A.1.6 · Synthesis of CoBPDC1

100 mg of biphenyl-4,4'-diacrboxylate (0.41 mmol) were dissolved in 12 ml of N,N-dimethylformamide in a 15 ml glass tube placed at 383K in an oil bath. Therefore, 98 mg of $Co(NO_3)_2 \cdot 6H_2O$ (0.37 mmol) were added to the solution. The tube was therefore sealed, shaken and left at 383K for 48 hours. The solution-gas interphase was kept slightly below the oil level, to limit the temperature inhomogeneities along the solution. After 24 hours, CoBPDC1 phase is present as prismatic violet crystals. The phase retains its appearance and crystallinity at room temperature only if taken from the synthesis solution and kept out of DMF contact. Otherwise, it readily decomposes in pink platelets (CoBPDC2, section 2.4, Chapter II) as soon as the temperature reaches 328K.

A.1.7 · Synthesis of TiO_x@IRMOF-9

Crystals of IRMOF-9 were quickly washed with an excess of isopropanol to remove the DMF from their surface. Afterwards, they were transferred in a vial containing 3 ml of pure titanium isopropoxide, and the system is closed and left at 298K for 30 days. A soaking time of 15 days was also tested: no distinguishable differences were recognised between samples soaked for 15 or 30 days. For the SCXRD analyses, the crystals were quickly washed with isopropanol to remove the titanium isopropoxide from their external surface, transferred in perfluoropolyether oil and rapidly placed at 100K on the diffractometer.

A.1.8 · Synthesis of $[(MB)CuCl_2]$ powder

142 mg of Methylene blue chloride pentahydrate (0.44 mmol) were put in an agate mortar, together with 44 mg CuCl (0.44 mmol). The solid powders were subsequently mixed and ground with an agate pestle for approximately 30 minutes. The mixture is yellowish green, with a metal-like shininess. After approximatively 2 hours the powder colour turned red, retaining the metallic appearance. XRPD analysis was performed. The resulting pattern (XRPD5, Section A.7) shows no signal of the starting reagent phases, but signals attributable to a new crystalline phase.

A.1.8.1 · Synthesis of $[(MB)CuCl_2]$ single crystals

Recrystallization trials of $[(MB)CuCl_2]$ have been set up using several solvents (dichlorometane, isopropanol, water, acetone, acetonitrile, nitromethane, N,N-dimethylformamide). In each case an excess of powder was put in a 15ml glass vial. Furthermore, 10 ml of solvent were added. The solution was put in an ultrasound bath for

10 min, in order to facilitate the solubilisation of the solid until the equilibrium has been reached. Afterwards, the supernatant was separated by centrifugation, and left open to crystallize by slow evaporation of the solvent. The recrystallization from N,N-dimethylformamide afforded suitable crystals for SCXRD (Figure A.4.8, section A.4). The XRPD pattern calculated from the determined structure matches the one measured on [(MB)$CuCl_2$] powder. The differences in the positions of the peaks are due to the different temperature (100K instead of 298K) at which the SCXRD analysis has been carried out with respect to the XRPD of the [(MB)$CuCl_2$] powder.

A.1.9 · Synthesis of [(MB)$AgCl_2$] powder

558 mg of methylene blue chloride pentahydrate (1.74 mmol) were put in an agate mortar, together with 250 mg AgCl (1.74 mmol). The solid powders were subsequently mixed and ground with an agate pestle for approximately 30 minutes. The resulting mixture is dark green. XRPD analysis was performed. The resulting pattern shows no signal of a new solid phase, but only the starting reagent characteristic peaks. 5 droplets of acetone were added to the ground powder to trigger the reaction, and the mixture has been ground for 10 minutes. This treatment has been repeated for three times. After the complete solvent assisted grinding treatment (30') the powder exhibits a dark red colour. XRPD analysis were performed on the powder, and the resulting pattern (XRPD6, Section A.7) shows no signal of the starting reagent phases, but signals attributable to a new crystalline phase (XRPD4, Section A.7: methylene blue pattern).

A.1.9.1 · Synthesis of [(MB)$AgCl_2$] single crystals

Recrystallization trials of [(MB)$AgCl_2$] have been set up using several solvents (dichlorometane, isopropanol, water, acetone, acetonitrile, nitromethane, N,N-dimethylformamide). In each case an excess of powder was put in a 15ml glass vial. Furthermore, 10 ml of solvent were added. The solution was put in an ultrasound bath for 10 min, in order to facilitate the solubilisation of the solid until the equilibrium is reached. Afterwards, the supernatant was separated by centrifugation, and left open to crystallize by slow evaporation of the solvent. The recrystallization from acetonitrile afforded suitable crystals for SCXRD (Figure A.4.8, section A.4). The XRPD pattern calculated from the determined structure matches the one measured on [(MB)$AgCl_2$] product. The differences in the positions of the peaks are due to the different temperature (100K instead of 298K) at which the single crystal XRD analysis was carried out with respect to the XRPD.

A.2 · Instrumental details

A.2.1. · SCXRD data collections (laboratory sources)

XRD data of phases **IRMOF-9**, **ZnBPDC1**, **ZnBPDC2**, **CoBPDC1** and **CoBPDC2** were acquired using a Bruker D8 Venture diffractometer, equipped with a Kryoflex II low termperature device, a CMOS Photon 100 detector, and a Mo High brilliance microsource (Incoatec) working at 50KV and 1Ma. The data have been processed using the APEX3 software[132], and corrected for adsorption using SADABS[133]. Measured crystals were prepared under inert conditions immersed in perfluoropolyether as protecting oil for manipulation. Suitable crystals were mounted on MiTeGen Micromounts™ and used for data collection.

A.2.2 · SCXRD data collections (synchrotron sources)

Synchrotron XRD data of phases **IRMOF-9LT**, **Co-IRMOF-9**, **IRMOF-9 (iPrOH)**, **IRMOF-9 (DCM)** and **TiO_x@IRMOF-9** have been measured at the XRD1 Beamline of the ELETTRA Synchrotron facility[134] using a 0.7Å monochromatic radiation and a Dectris Pilatus 2M detector (CMOS hybrid-pixel technology) operating in single-photon-counting mode. All the data collections were performed at 100K if not otherwise specified (Co-IRMOF-9, 258K). The collected data have been processed using the CrysAlisPro software[57].

A.2.3 · XRPD data collections (laboratory sources)

Powder X-ray diffraction data have been collected on a Thermo ARL X'TRA X-Ray diffractometer with Si-Li detector, using Cu-K_α radiation at 40kV and 40mA and working in a Bragg-Brentano geometry. All measurements were performed at room temperature.

A.2.4 · XRPD data collections (synchrotron sources)

Powder XRD data on IRMOF-9 and Co-IRMOF-9 showed in Chapter II were collected at the XRD1 beamline at the ELETTRA Synchrotron facility (XRD1 beamline[134], see paragraph A.2.2). Diffraction data were collected using a monochromatic 0.7 Å wavelength at 298K. For this purpose, a glass capillary (0.5mm diameter) was filled with pure N,N-dimethylformamide and crystals of IRMOF-9 or Co-IRMOF-9 were introduced and left to settle. Afterwards, the capillary was mounted on the goniometer, centred in the X-ray beam pathway and diffraction data has been collected while rotating the capillary. The final powder pattern was reconstructed from the acquired diffraction rings by using the XDS software. Powder

XRD data on TiO_xM1 were collected at the MS-Powder beamline at the Swiss Light Source facility[135] (Paul Scherrer Institute). Diffraction data were collected by a Mythen II detector using a monochromatic 0.5636 Å wavelength at 298K and a Debye-Scherrer geometry. The sample was prepared in a 0.3mm glass capillary.

A.2.5 · DSC analyses

DSC analyses on **IRMOF-9**, **Co-IRMOF-9** and **CoBPDC1** were performed on a PerkinElmer DSC6000 with Intracooler 6P cooling device and N_2 purging gas. Crystals were analysed in a DMF droplet to avoid their decomposition due to their instability to moisture. For this reason, no quantitative information is pursued regarding the transformations. The samples were placed in a 50 µL aluminium pan and a temperature ramp was applied from in the range of interest, with a cooling/heating rate of 5°C/min. A control experiment on pure DMF showed no remarkable signals.

A.2.6 · ICP-OES analyses

ICP-OES analyses were performed with a ULTIMA 2 instrument HORIBA (Jobin Yvon, Longjumeau, France) in radial configuration, with a JY 2501 monochromator calibrated against carbon lines. The optical path was continuously purged with nitrogen (2 l/min). Calibration was performed with standard solutions 10% of HNO_3 on six different metal concentration levels, ranging from 0.05 $mg{\cdot}L^{-1}$ to 10 $mg{\cdot}L^{-1}$. No significant spectral interferences were detected. Data acquisition and processing were performed using the ICP JY v 5.4.2 software (Jobin Yvon). Each solid is dried under vacuum at r.t. A certain amount of it is therefore digested in 10 mL of HNO_3 65% overnight. After digestion, the ligand remains insoluble, appearing as a white precipitate. The metal containing solution is therefore separated with a centrifuge, and then 0.77 mL of the solution is diluted with deionized water to obtain 25 mL of a 3ppm metal solution in 2% HNO_3.

A.2.7 · SEM analyses

SEM Analyses were performed on an Environmental Scanning Microscope Quanta™ 250 FEG (FEI, Hillsboro, OR) equipped with an energy dispersion detector (EDS) QUANTAX XFlash® 6|30 for X-ray microanalysis (Bruker Nano GmbH, Berlin, Germany). Analyses were performed in low vacuum mode at a working pressure of 70 Pa. Morphologic analyses were obtained detecting the signal of secondary electrons using a Large Field Detector (LFD) and 5 kV tension. For the X-ray microanalyses the working tension was set at 20 kV.

A.3 · Additional crystallographic information

All structure solutions were performed by using SHELXT program[136] integrated in the OLEX2 software[48], using the intrinsic phasing method for the solution of the phase problem. For the structure refinements, the SHELXL[137] program was used with least square method.

A.3.1 · Crystallographic reports

IRMOF-9LT

Empirical formula	$C_{48}H_{38}N_2O_{15}Zn_4$
Formula weight	1144.28
Temperature/K	100.0
Crystal system	monoclinic
Space group	$P2_1/n$
a/Å	17.1224(9)
b/Å	21.412(2)
c/Å	26.6098(11)
β/°	95.149(4)
Volume/Å^3	9716.6(13)
Z	4
ρ_{calc}g/cm^3	0.782
μ/mm^{-1}	1.009
F(000)	2320.0
Radiation	Synchrotron (λ = 0.700)
2Θ range for data collection/°	3.006 to 51.888
Index ranges	-21 ≤ h ≤ 21, -26 ≤ k ≤ 26, -33 ≤ l ≤ 33
Reflections collected	56856

Independent reflections	56856 [R_{int} = 0.0783, R_{sigma} = 0.0644]
Data/restraints/parameters	56856/149/485
Goodness-of-fit on F^2	1.722
Final R indexes [I>=2σ (I)]	R_1 = 0.1773, wR_2 = 0.4604
Final R indexes [all data]	R_1 = 0.2454, wR_2 = 0.5025
Largest diff. peak/hole / e $Å^{-3}$	2.60/-1.85

The analysed specimen is twinned (four main domains, two major ones). The percentages of the total harvested reflections belonging to each domain are:
Domain 1: 45.0%
Domain 2: 44.4%
Domain 3: 27.0%
Domain 4: 28.1%

These domains are related by the following operations:
Rot(UB1, UB2) = -179.9515° about (0.99 0.00 -0.14) in reciprocal space, (1.00 0.00 0.00) in direct space;
Rot(UB1, UB3) = 4.9793° about (-0.09 1.00 -0.01) in reciprocal space, (-0.14 0.99 -0.01) in direct space;
Rot(UB1, UB4) = 179.9675° about (-0.03 0.00 1.00) in reciprocal space, (0.07 0.01 1.00) in direct space;
Rot(UB2, UB3) = 179.3945° about (1.00 0.00 -0.07) in reciprocal space, (1.00 0.00 0.03) in direct space;
Rot(UB2, UB4) = -174.6829° about (0.00 1.00 -0.01) in reciprocal space, (0.00 1.00 0.00) in direct space;
Rot(UB3, UB4) = -179.9898° about (-0.05 0.00 1.00) in reciprocal space, (0.00 0.00 1.00) in direct space;

The best refinement was obtained after the integration of the reflections belonging to the two major domains (1 and 2).

IRMOF-9 (298K)

Empirical formula	$CH_{13.75}N_{0.25}O_{6.75}Zn_2$
Formula weight	517.32
Temperature/K	298.0
Crystal system	orthorhombic
Space group	Pnnm
a/Å	17.134(3)
b/Å	22.456(5)
c/Å	25.957(5)
Volume/$Å^3$	9988(3)
Z	8
$\rho_{calc}g/cm^3$	0.688
μ/mm^{-1}	0.977
F(000)	2080.0
Radiation	MoKα (λ = 0.71073)
2Θ range for data collection/°	4.334 to 43.932
Index ranges	$-18 \leq h \leq 17$, $-23 \leq k \leq 23$, $-27 \leq l \leq 27$
Reflections collected	56261
Independent reflections	6267 [R_{int} = 0.0996, R_{sigma} = 0.0534]
Data/restraints/parameters	6267/75/300
Goodness-of-fit on F^2	1.019
Final R indexes [I>=2σ (I)]	R_1 = 0.0618, wR_2 = 0.1766
Final R indexes [all data]	R_1 = 0.0843, wR_2 = 0.2012
Largest diff. peak/hole / e $Å^{-3}$	0.94/-0.66

Solvent mask volume: 6664.1$Å^3$. Electron count: 117.9

IRMOF-9 (iPrOH)

Empirical formula	$C_{54}H_{56}O_{17}Zn_4$
Formula weight	1238.46
Temperature/K	100
Crystal system	monoclinic
Space group	$P2_1/n$
a/Å	22.0643(4)
b/Å	17.1852(2)
c/Å	26.1140(3)
β/°	90.7490(10)
Volume/Å^3	9901.0(2)
Z	4
ρ_{calc}g/cm^3	0.831
μ/mm^{-1}	0.994
F(000)	2544.0
Radiation	Synchrotron (λ = 0.700)
2Θ range for data collection/°	2.958 to 60
Index ranges	-31 ≤ h ≤ 31, -24 ≤ k ≤ 24, -37 ≤ l ≤ 37
Reflections collected	127262
Independent reflections	24617 [R_{int} = 0.1641, R_{sigma} = 0.0857]
Data/restraints/parameters	24617/3/584
Goodness-of-fit on F^2	1.020
Final R indexes [I>=2σ (I)]	R_1 = 0.1098, wR_2 = 0.2932
Final R indexes [all data]	R_1 = 0.1176, wR_2 = 0.3033
Largest diff. peak/hole / e Å^{-3}	1.76/-1.60

Solvent mask volume: 5253.1 Å^3. Electron count: 592.6

The analysed specimen is twinned (two domains). The two phases are related by a Rot(UB1, UB2) = -179.9972° around the (0.00, 0.00, 1.00) vector in the reciprocal space, (0.00, -0.01, 1.00) in the direct space. The best refinement was obtained by integrating only one of the two domains.

ZnBPDC2

Empirical formula	$C_{14}H_{14}O_7Zn_{0.55}$
Formula weight	315.36
Temperature/K	100.0
Crystal system	orthorhombic
Space group	Ima2
a/Å	6.5350(6)
b/Å	30.295(3)
c/Å	7.1459(9)
Volume/Å^3	1414.7(3)
Z	4
ρ_{calc}g/cm^3	1.481
μ/mm^{-1}	0.996
F(000)	625.0
Radiation	MoKα (λ = 0.71073)
2Θ range for data collection/°	5.378 to 52.858
Index ranges	-7 ≤ h ≤ 8, -37 ≤ k ≤ 37, -8 ≤ l ≤ 8
Reflections collected	14046
Independent reflections	1574 [R_{int} = 0.0547, R_{sigma} = 0.0289]
Data/restraints/parameters	1574/1/122
Goodness-of-fit on F^2	1.195
Final R indexes [I>=2σ (I)]	R_1 = 0.0494, wR_2 = 0.1242
Final R indexes [all data]	R_1 = 0.0637, wR_2 = 0.1353
Largest diff. peak/hole / e Å^{-3}	0.42/-0.44
Flack parameter	0.003(6)

The phase is affected by merohedral twinning (Law: (-1.0, 0.0, 0.0; 0.0, 1.0, 0.0; 0.0, 0.0, -1.0); BASF: 0.53(5).), and by occupational disorder involving the Zn atom, whose occupancy is 0.55. Protonated BPDC are likely present. The additional protons were not included in the model.

Co-IRMOF-9

Empirical formula	$C_{21}H_{12}Co_2O_{6.5}$
Formula weight	485.50
Temperature/K	258
Crystal system	orthorhombic
Space group	Pnnm
a/Å	17.1291(4)
b/Å	21.8862(5)
c/Å	26.2493(7)
Volume/$Å^3$	9840.6(4)
Z	8
$\rho_{calc}g/cm^3$	0.655
μ/mm^{-1}	0.664
F(000)	1947.0
Radiation	Synchrotron (λ = 0.700)
2Θ range for data collection/°	2.974 to 45.766
Index ranges	-19 ≤ h ≤ 19, -24 ≤ k ≤ 24, -29 ≤ l ≤ 29
Reflections collected	86881
Independent reflections	7232 [R_{int} = 0.1168, R_{sigma} = 0.0527]
Data/restraints/parameters	7232/15/269
Goodness-of-fit on F^2	2.077
Final R indexes [I>=2σ (I)]	R_1 = 0.1637, wR_2 = 0.4529
Final R indexes [all data]	R_1 = 0.1784, wR_2 = 0.4741
Largest diff. peak/hole / e $Å^{-3}$	1.75/-1.14

CoBPDC1

Empirical formula	$C_{24}H_{19}Co_{1.5}NO_7$
Formula weight	521.80
Temperature/K	353.0
Crystal system	monoclinic
Space group	$P2_1/n$
a/Å	11.0222(14)
b/Å	15.1754(19)
c/Å	19.331(3)
β/°	100.256(4)
Volume/Å^3	3181.7(7)
Z	4
ρ_{calc}g/cm^3	1.089
μ/mm^{-1}	0.823
F(000)	1066.0
Radiation	MoKα (λ = 0.71073)
2Θ range for data collection/°	4.616 to 49.422
Index ranges	-12 ≤ h ≤ 12, -17 ≤ k ≤ 17, -22 ≤ l ≤ 22
Reflections collected	39837
Independent reflections	5397 [R_{int} = 0.0574, R_{sigma} = 0.0306]
Data/restraints/parameters	5397/0/302
Goodness-of-fit on F^2	1.033
Final R indexes [I>=2σ (I)]	R_1 = 0.0395, wR_2 = 0.0892
Final R indexes [all data]	R_1 = 0.0508, wR_2 = 0.0937
Largest diff. peak/hole / e Å^{-3}	0.40/-0.34

Solvent mask volume: 1234.8Å^3. Electron count: 211.3

CoBPDC2

Empirical formula	$C_{63}H_{73}Co_3N_7O_{19}$
Formula weight	1409.07
Temperature/K	100.0
Crystal system	monoclinic
Space group	Pn
a/Å	13.1391(7)
b/Å	13.3582(6)
c/Å	19.7524(10)
β/°	106.272(2)
Volume/Å^3	3328.0(3)
Z	2
ρ_{calc}g/cm^3	1.406
μ/mm^{-1}	0.815
F(000)	1466.0
Radiation	MoKα (λ = 0.71073)
2Θ range for data collection/°	4.296 to 52.74
Index ranges	-16 ≤ h ≤ 16, -16 ≤ k ≤ 16, -24 ≤ l ≤ 24
Reflections collected	135826
Independent reflections	13622 [R_{int} = 0.0585, R_{sigma} = 0.0283]
Data/restraints/parameters	13622/2/844
Goodness-of-fit on F^2	1.025
Final R indexes [I>=2σ (I)]	R_1 = 0.0268, wR_2 = 0.0601
Final R indexes [all data]	R_1 = 0.0342, wR_2 = 0.0635
Largest diff. peak/hole / e Å^{-3}	0.34/-0.37
Flack parameter	0.007(3)

The phase is affected by merohedral twinning; twinning law: (-1.0, 0.0, 0.0, 0.0, -1.0, 0.0, 0.0, 0.0, -1.0); BASF: 0.344(11).

TiO_x@IRMOF-9 (Sample 1)

Empirical formula	$C_{21}H_{12}O_{6.5}Zn_2$
Formula weight	499.1
Temperature/K	100
Crystal system	orthorhombic
Space group	Pnnm
a/Å	17.1172(3)
b/Å	23.3182(5)
c/Å	25.0552(5)
Volume/Å^3	10000.6(3)
Z	8
ρ_{calc}g/cm^3	0.660
μ/mm^{-1}	0.922
F(000)	1992.0
Radiation	Synchrotron (λ = 0.700)
2Θ range for data collection/°	3.202 to 55.634
Index ranges	-22 ≤ h ≤ 22, -30 ≤ k ≤ 30, -33 ≤ l ≤ 33
Reflections collected	147465
Independent reflections	12683 [R_{int} = 0.1110, R_{sigma} = 0.0365]
Data/restraints/parameters	12683/9/303
Goodness-of-fit on F^2	1.279
Final R indexes [I>=2σ (I)]	R_1 = 0.1171, wR_2 = 0.3524
Final R indexes [all data]	R_1 = 0.1427, wR_2 = 0.3730
Largest diff. peak/hole / e Å^{-3}	1.20/-0.97

Solvent mask volume: 6765.0Å^3. Electron count: 1329.3.

TiO_x@IRMOF-9 (Sample 2)

Empirical formula	$C_{21}H_{12}O_{8.2}Ti_{0.6}Zn_2$
Formula weight	554.99
Temperature/K	100
Crystal system	orthorhombic
Space group	Pnnm
a/Å	17.1424(2)
b/Å	23.0158(4)
c/Å	25.3071(4)
Volume/Å^3	9984.8(3)
Z	8
ρ_{calc}g/cm^3	0.738
μ/mm^{-1}	1.032
F(000)	2214.0
Radiation	Synchrotron (λ = 0.700)
2Θ range for data collection/°	3.17 to 48.63
Index ranges	-18 ≤ h ≤ 18, -27 ≤ k ≤ 27, -29 ≤ l ≤ 29
Reflections collected	106487
Independent reflections	8459 [R_{int} = 0.0942, R_{sigma} = 0.0348]
Data/restraints/parameters	8459/2/309
Goodness-of-fit on F^2	1.265
Final R indexes [I>=2σ (I)]	R_1 = 0.0911, wR_2 = 0.3035
Final R indexes [all data]	R_1 = 0.1050, wR_2 = 0.3200
Largest diff. peak/hole / e Å^{-3}	0.83/-0.74

Solvent mask volume: 5885.5Å^3. Electron count: 199.5.

TiO_x@IRMOF-9 (Sample 3)

Empirical formula	$C_{21}H_{12}O_{6.5}Zn_2$
Formula weight	499.1
Temperature/K	100
Crystal system	orthorhombic
Space group	Pnnm
a/Å	17.1127(2)
b/Å	22.3852(5)
c/Å	25.8191(4)
Volume/Å^3	9890.6(3)
Z	8
ρ_{calc}g/cm^3	0.668
μ/mm^{-1}	0.984
F(000)	1992.0
Radiation	Synchrotron (λ = 0.700)
2Θ range for data collection/°	3.108 to 54.068
Index ranges	-20 ≤ h ≤ 20, -29 ≤ k ≤ 29, -33 ≤ l ≤ 33
Reflections collected	132531
Independent reflections	11013 [R_{int} = 0.0485, R_{sigma} = 0.0163]
Data/restraints/parameters	11013/465/317
Goodness-of-fit on F^2	1.063
Final R indexes [I>=2σ (I)]	R_1 = 0.0860, wR_2 = 0.2644
Final R indexes [all data]	R_1 = 0.1029, wR_2 = 0.2960
Largest diff. peak/hole / e Å^{-3}	0.99/-0.69

Solvent mask volume: 6070.5Å^3. Electron count: 832.3.

TiO_x@IRMOF-9 (Sample 4)

Empirical formula	$C_{21}H_{12}O_{6.5}Zn_2$
Formula weight	499.1
Temperature/K	100
Crystal system	orthorhombic
Space group	Pnnm
a/Å	17.1249(2)
b/Å	22.2575(4)
c/Å	25.9268(4)
Volume/$Å^3$	9882.2(3)
Z	8
$\rho_{calc}g/cm^3$	0.664
μ/mm^{-1}	0.939
F(000)	1979.0
Radiation	Synchrotron (λ = 0.700)
2Θ range for data collection/°	3.094 to 59.998
Index ranges	-24 ≤ h ≤ 24, -31 ≤ k ≤ 31, -37 ≤ l ≤ 37
Reflections collected	179678
Independent reflections	15395 [R_{int} = 0.0600, R_{sigma} = 0.0244]
Data/restraints/parameters	15395/97/328
Goodness-of-fit on F^2	1.091
Final R indexes [I>=2σ (I)]	R_1 = 0.0825, wR_2 = 0.2919
Final R indexes [all data]	R_1 = 0.1000, wR_2 = 0.3149
Largest diff. peak/hole / e $Å^{-3}$	0.89/-1.07

Solvent mask volume: 6169.2$Å^3$. Electron count: 966.7.

TiO_x@IRMOF-9 (Sample 5)

Empirical formula	$C_{21}H_{12}O_{6.5}Zn_2$
Formula weight	499.1
Temperature/K	100
Crystal system	orthorhombic
Space group	Pnnm
a/Å	17.1229(2)
b/Å	21.8088(5)
c/Å	26.2024(4)
Volume/Å^3	9784.8(3)
Z	8
ρ_{calc}g/cm^3	0.675
μ/mm^{-1}	0.944
F(000)	1993.0
Crystal size/mm^3	0.5 × 0.5 × 0.35
Radiation	Synchrotron (λ = 0.700)
2Θ range for data collection/°	3.348 to 59.994
Index ranges	-23 ≤ h ≤ 23, -30 ≤ k ≤ 30, -37 ≤ l ≤ 37
Reflections collected	167612
Independent reflections	14954 [R_{int} = 0.0616, R_{sigma} = 0.0229]
Data/restraints/parameters	14954/20/337
Goodness-of-fit on F^2	1.347
Final R indexes [I>=2σ (I)]	R_1 = 0.0935, wR_2 = 0.3338
Final R indexes [all data]	R_1 = 0.1071, wR_2 = 0.3515
Largest diff. peak/hole / e Å^{-3}	1.21/-0.75

Solvent mask volume: 5993.6Å^3. Electron count: 1113.2.

TiO_x@IRMOF-9 (Sample 6)

Empirical formula	$C_{21}H_{12}O_{6.5}Zn_2$
Formula weight	499.1
Temperature/K	100
Crystal system	orthorhombic
Space group	Pnnm
a/Å	17.1689(3)
b/Å	20.4106(14)
c/Å	27.1330(10)
Volume/Å^3	9508.2(8)
Z	8
ρ_{calc}g/cm^3	0.658
μ/mm^{-1}	0.983
F(000)	1883.0
Radiation	Synchrotron (λ = 0.700)
2Θ range for data collection/°	3.392 to 45.768
Index ranges	-19 ≤ h ≤ 19, -22 ≤ k ≤ 22, -30 ≤ l ≤ 30
Reflections collected	85477
Independent reflections	7001 [R_{int} = 0.1942, R_{sigma} = 0.0677]
Data/restraints/parameters	7001/12/336
Goodness-of-fit on F^2	1.595
Final R indexes [I>=2σ (I)]	R_1 = 0.1183, wR_2 = 0.3805
Final R indexes [all data]	R_1 = 0.1290, wR_2 = 0.4027
Largest diff. peak/hole / e Å^{-3}	1.45/-0.57

Solvent mask volume: 6164.4Å^3. Electron count: 642.5.

MBCu

Empirical formula	$C_{16}H_{18}Cl_2CuN_3S$
Formula weight	418.83
Temperature/K	100.0
Crystal system	triclinic
Space group	P-1
a/Å	7.7053(3)
b/Å	9.9702(7)
c/Å	11.2564(8)
α/°	86.236(6)
β/°	71.670(6)
γ/°	80.892(5)
Volume/Å^3	810.41(9)
Z	2
ρ_{calc}g/cm^3	1.716
μ/mm^{-1}	1.750
F(000)	428.0
Radiation	Synchrotron (λ = 0.700)
2Θ range for data collection/°	3.754 to 59.986
Index ranges	-10 ≤ h ≤ 10, -13 ≤ k ≤ 14, 0 ≤ l ≤ 16
Reflections collected	15861
Independent reflections	4726 [R_{int} = 0.0486, R_{sigma} = 0.0378]
Data/restraints/parameters	4726/0/212
Goodness-of-fit on F^2	1.099
Final R indexes [I>=2σ (I)]	R_1 = 0.0296, wR_2 = 0.0818
Final R indexes [all data]	R_1 = 0.0312, wR_2 = 0.0827
Largest diff. peak/hole / e Å^{-3}	0.56/-0.74

MBAg

Empirical formula	$C_{16}H_{18}AgCl_2N_3S$
Formula weight	463.16
Temperature/K	100
Crystal system	triclinic
Space group	P-1
a/Å	7.4140(3)
b/Å	10.4698(7)
c/Å	11.3141(6)
α/°	85.905(5)
β/°	74.720(5)
γ/°	78.665(5)
Volume/Å^3	830.48(8)
Z	2
ρ_{calc}g/cm^3	1.852
μ/mm^{-1}	1.601
F(000)	464.0
Radiation	Synchrotron (λ = 0.700)
2Θ range for data collection/°	3.676 to 55.632
Index ranges	-9 ≤ h ≤ 9, -13 ≤ k ≤ 13, -15 ≤ l ≤ 15
Reflections collected	11779
Independent reflections	3460 [R_{int} = 0.0579, R_{sigma} = 0.0476]
Data/restraints/parameters	3460/0/212
Goodness-of-fit on F^2	1.061
Final R indexes [I>=2σ (I)]	R_1 = 0.0662, wR_2 = 0.1876
Final R indexes [all data]	R_1 = 0.0742, wR_2 = 0.1927
Largest diff. peak/hole / e Å^{-3}	1.53/-1.26

The analysed specimen is twinned (two domains). The two phases are related by a Rot(UB1, UB2) = -179.9876° around the (0.00, 0.71, 0.71) vector in the reciprocal space, (-0.43, 0.68, 0.60) in the direct space. The best refinement was obtained by integrating only one of the two domains.

A.3.2 · IRMOF-9 voids calculations

For the calculations of solid phases voids volume and the computation of internal surface areas, the function "Display voids" of the Mercury software[56] has been used. A probe radius of 1.2Å and a grid of 0.2Å have been selected; the calculations were performed using the "contact surface" method.

In case of disordered structures, only the most ordered fraction of the phase has been considered and the additional atomic positions removed.

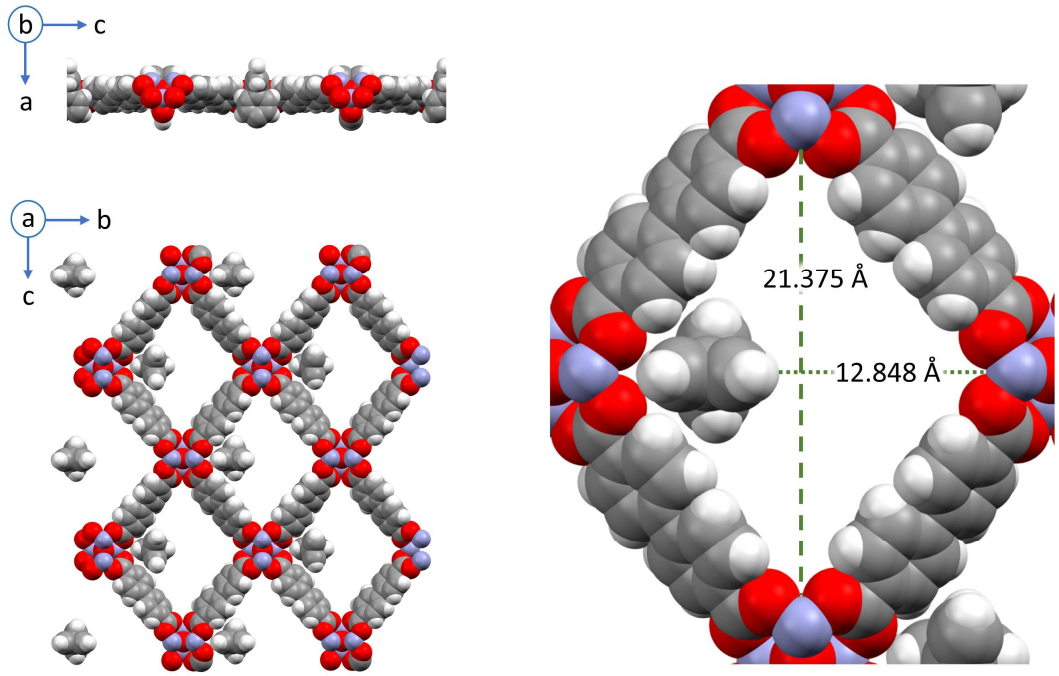

Figure A.3.2. Details on the IRMOF-9 void dimensions calculations performed using the Mercury software[56]. On the left, the considered layer of the unit cell is displayed perpendicular and along the channel axis (above and below respectively). On the right, a magnification shows the cavity considered dimensions. Atom-Atom measurements were carried out, and the Van der Waals radii of the atoms at issue have been therefore subtracted.

A.4 · Optical microscopy images

In the following pictures, different region in the "U" tube gel crystallisaiton experiment (paragraph A.1.3, Appendix) are shown. In the upper part, the sections of the tube; a red circle marks the region where the image has been captured.

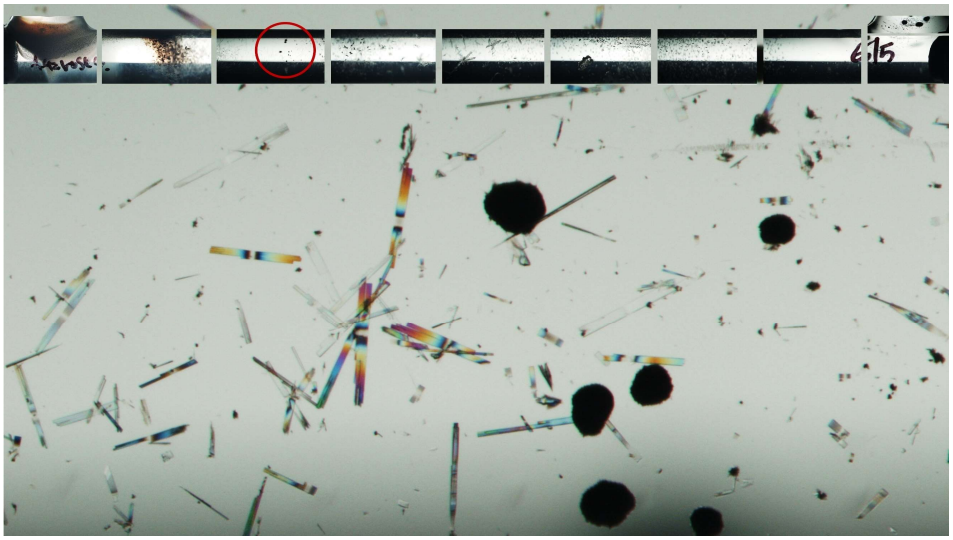

Figure A.4.1. Rectangular crystals of ZnBPDC2.

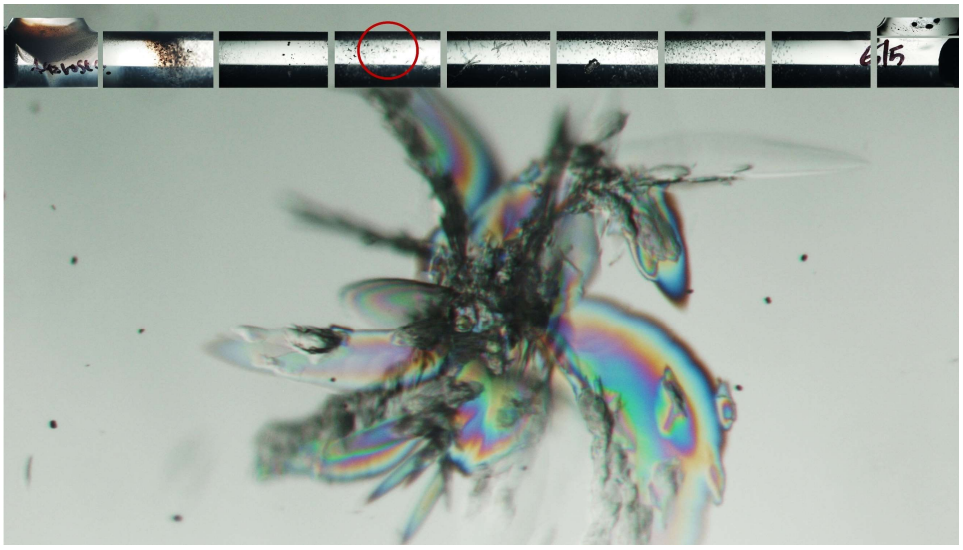

Figure A.4.2. Irregular crystals of ZnBPDC1.

Figure A.4.3. Parallelogramic crystals of ZnBPDC1.

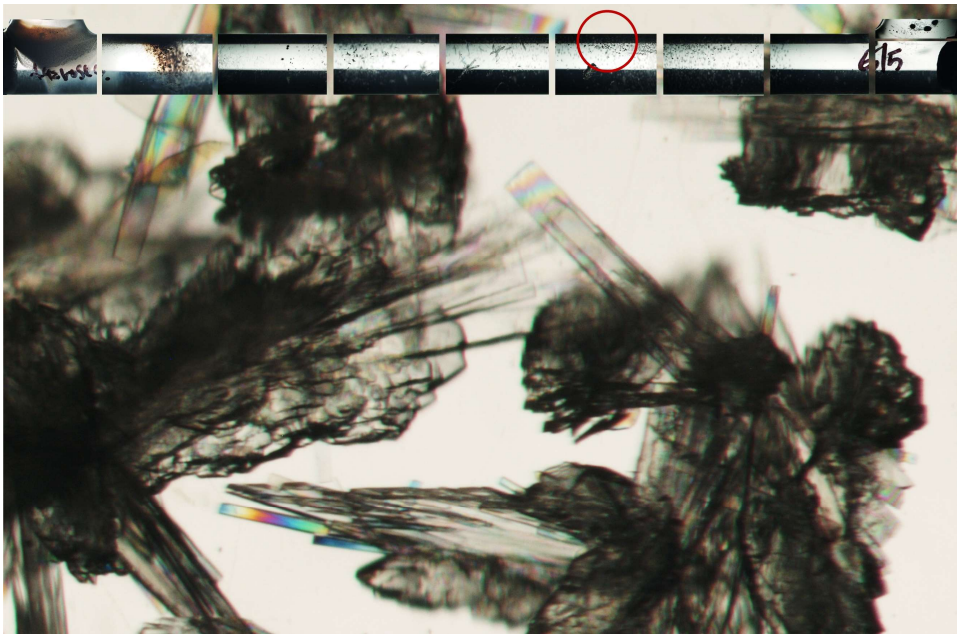

Figure A.4.4. Rectangular crystals of ZnBPDC2 grown on aggregates of ZnBPDC1 crystals.

Figure A.4.5. Aggregated and isolated crystals of ZnBPDC2.

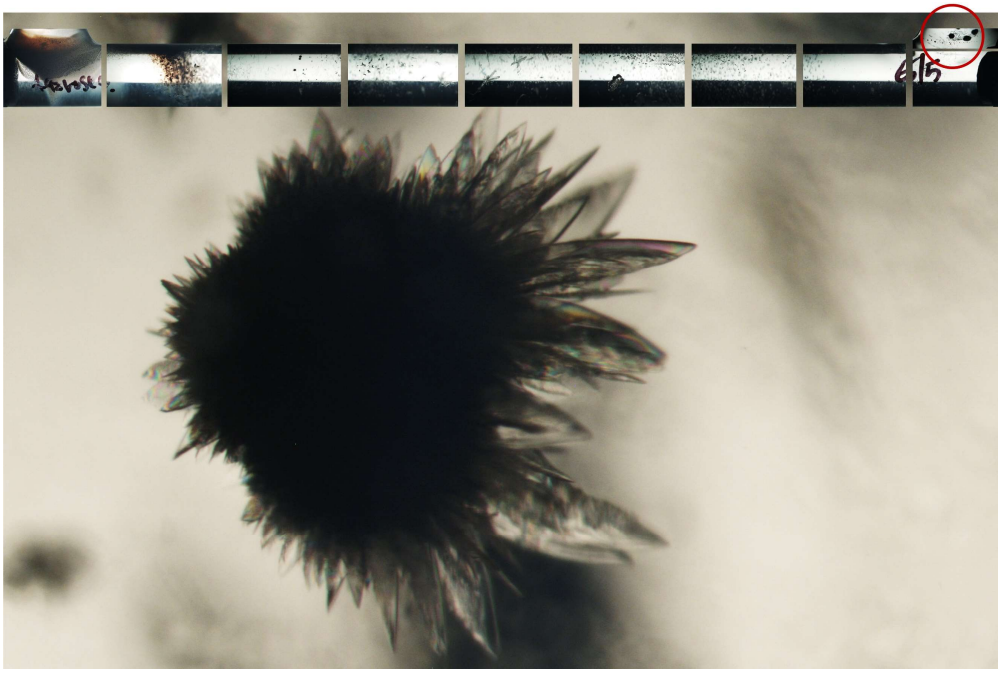

Figure A.4.6. Aggregate of ZnBPDC1 crystals.

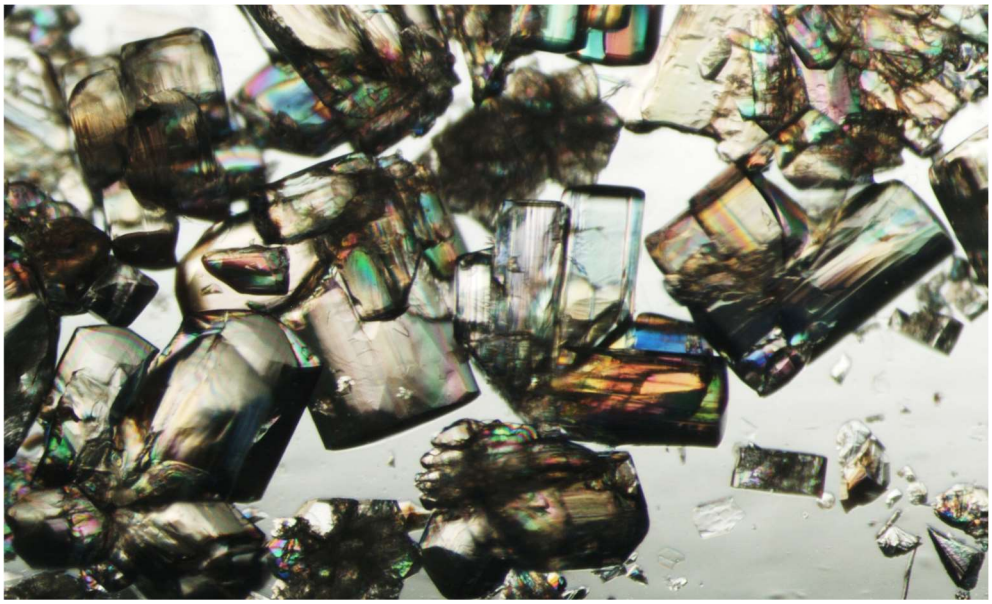

Figure A.4.7. Crystals of IRMOF-9 after soaking in $Ti(iPrO)_4$, showing no remarkable difference with respect to untreated IRMOF-9 crystals. The colours are due to the polarisation of the light.

A.5 · SEM additional data

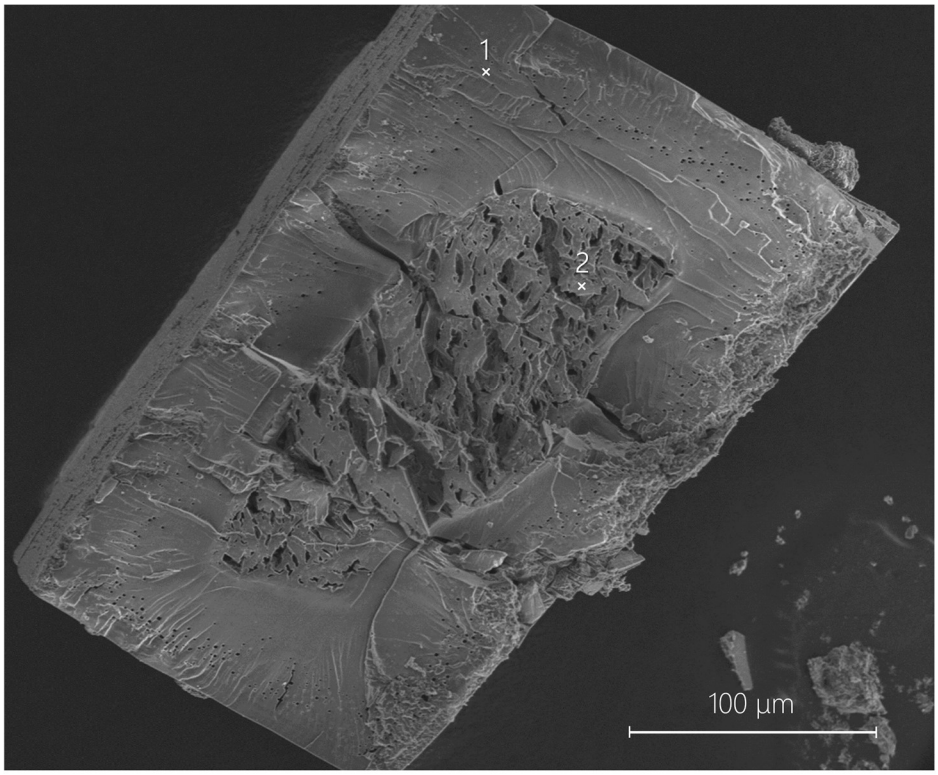

SEM1. *ESEM micrograph of the cut crystal used to perform elemental composition analyses (IRMOF-9 after 7 days of soaking in a 0.2M $CoCl_2$ DMF solution at 305K). The points where the microanalyses were performed are reported in white (1 and 2).*

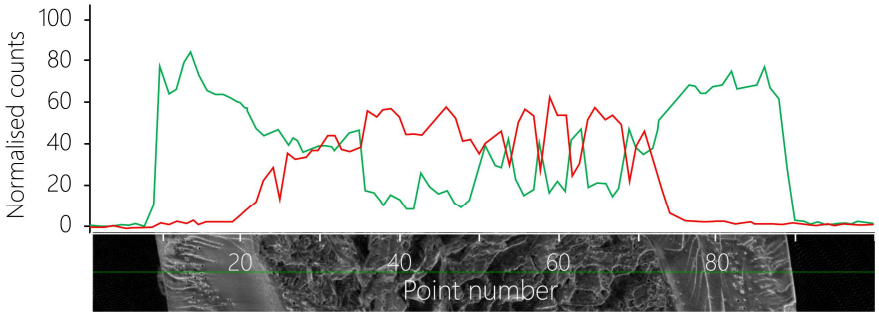

EDX1. *Plot of the linear atomic emission scan performed along the longer dimension of the crystal shown in SEM1. The signals of Zn and Co are marked with a green and a red colour respectively.*

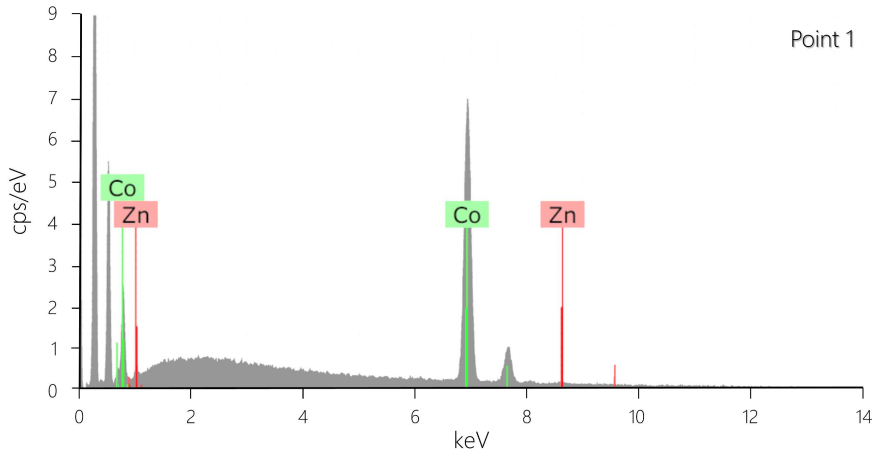

EDX2. *Atomic emission spectrum for point 1, shown in SEM1.*

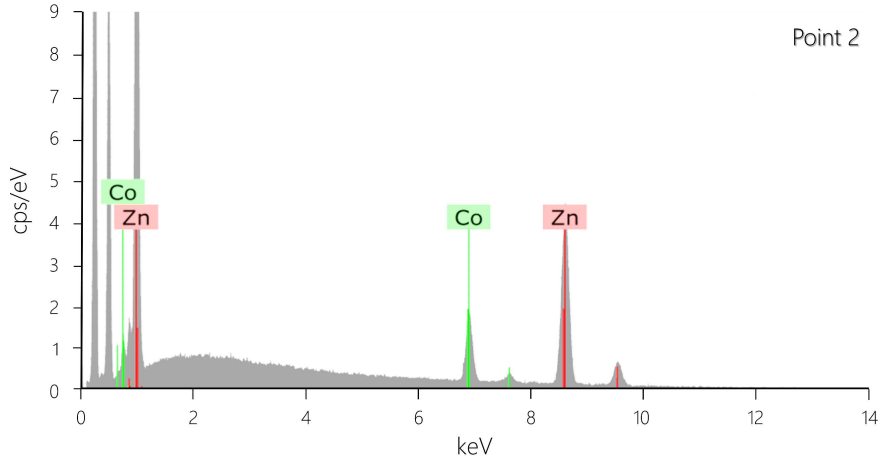

EDX3. *Atomic emission spectrum for point 2, shown in SEM1.*

	Point 1	Point 2
Zn atomic %	0.4	84.6
Co atomic %	99.6	15.4
Zn at. %/Co at. %	0.004	5.0

EDX Table 1. *Values of Zn to Co ratio (between atomic %) in points shown in Figure SEM1; other identified elements in the spectra were used for only deconvolution in standard-less PB-ZAF quantification.*

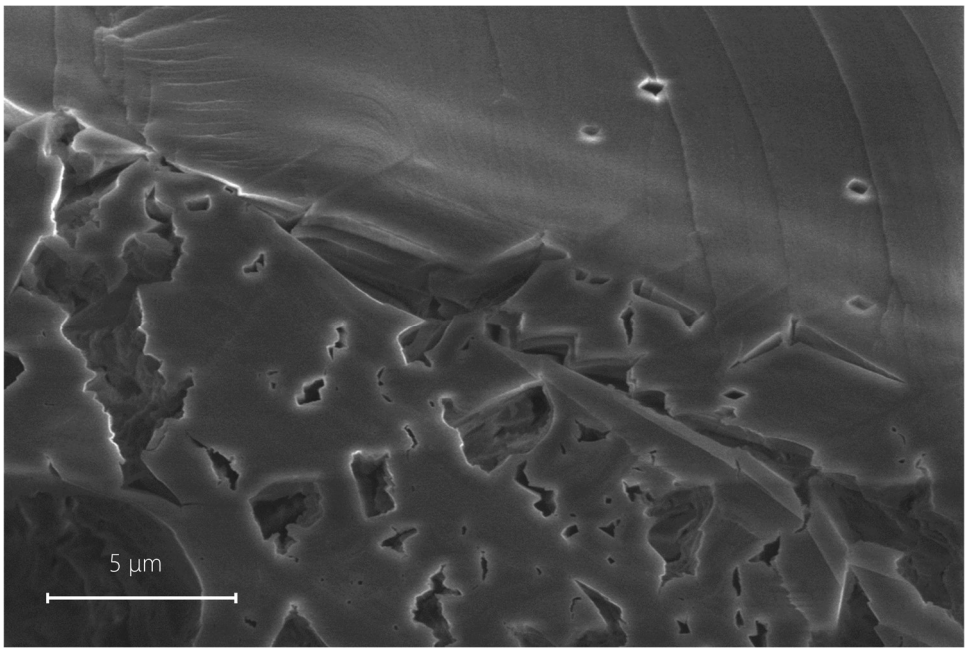

SEM2. *ESEM micrograph of a selected region of the sample shown in SEM1, highlighting the different morphologies of Co-IRMOF-9 (upper part) and not completely transmetalated IRMOF-9 (lower part).*

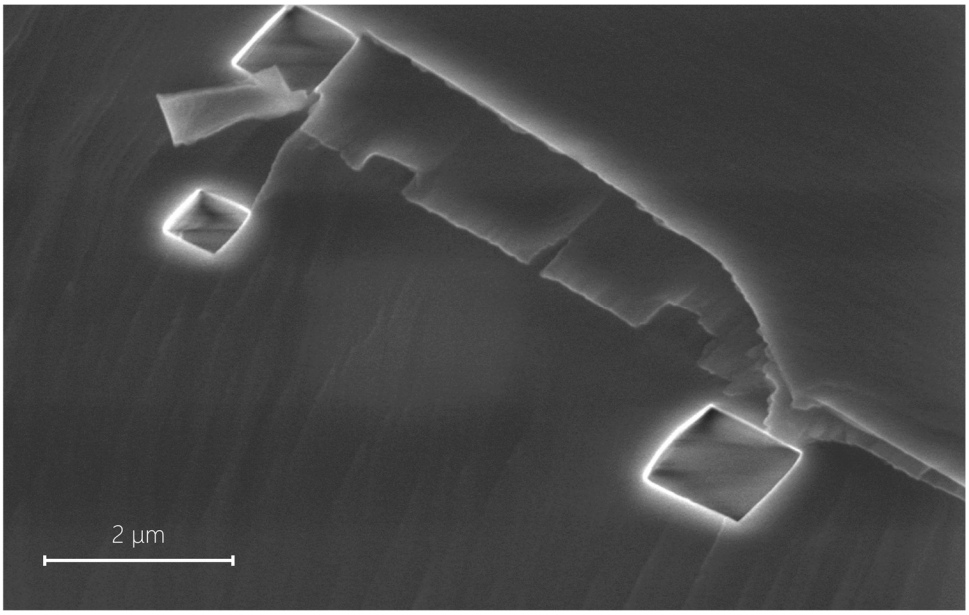

SEM3. *ESEM micrograph of a selected region of the sample shown in SEM1, highlighting the µm-sized holes present in the inner section of the crystal.*

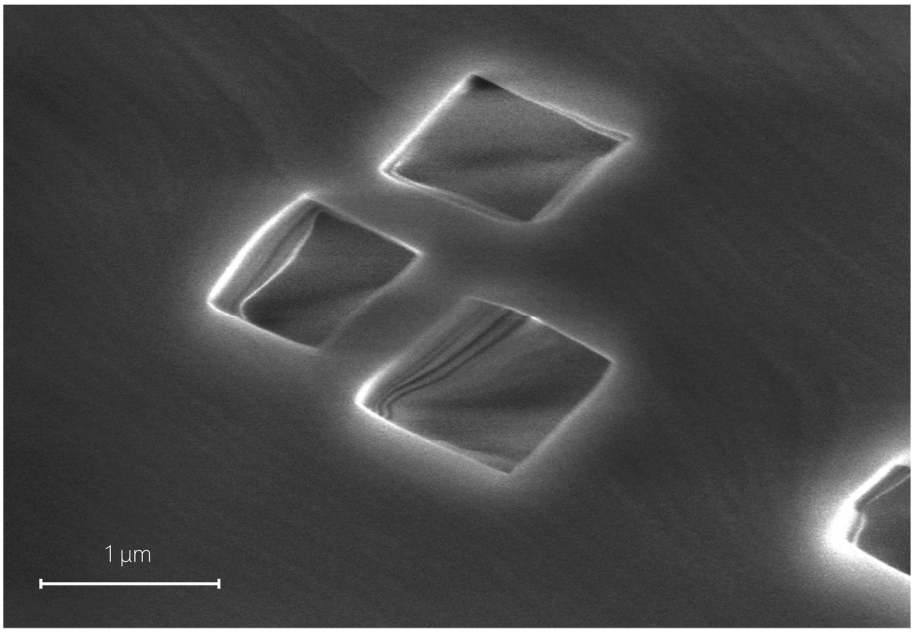

SEM4. *ESEM micrograph of a selected region of the sample shown in SEM1, highlighting the µm-sized holes present in the inner section of the crystal.*

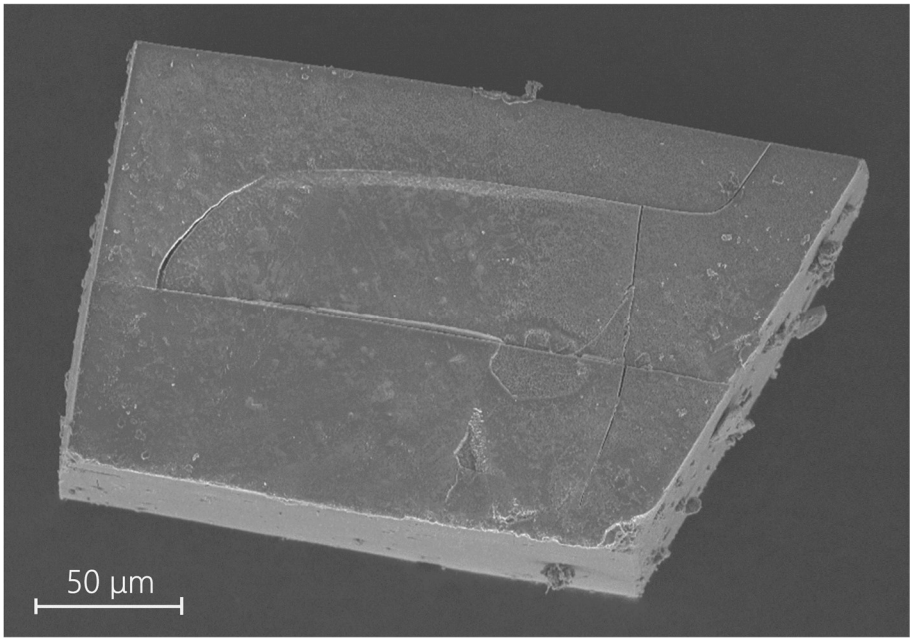

SEM5. *ESEM image of the external surface of an IRMOF-9 crystal.*

A.6 · DSC profiles

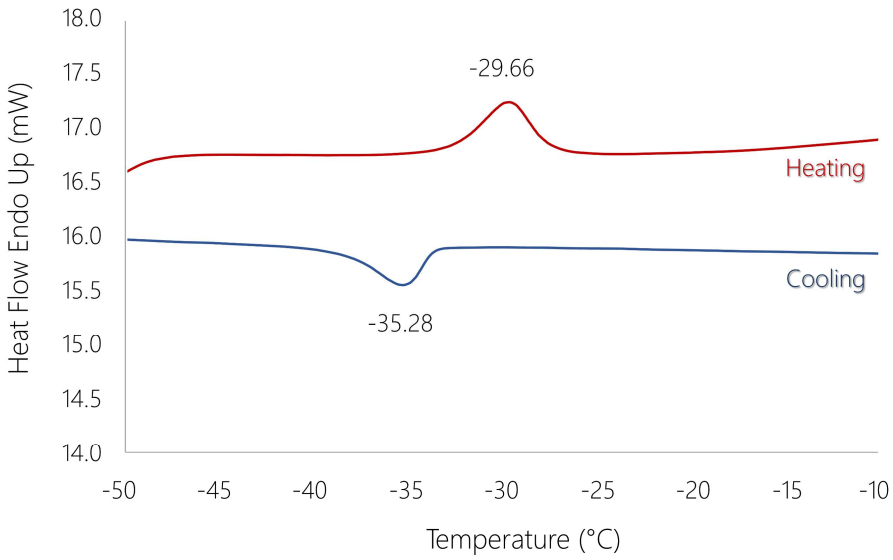

DSC1. *Thermal profile of IRMOF-9*

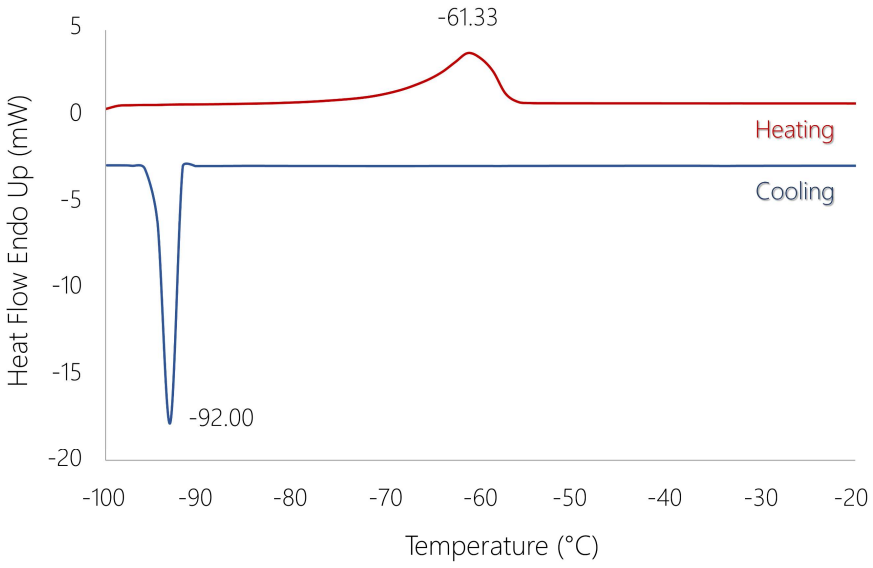

DSC2. *Thermal profile of Co-IRMOF-9*

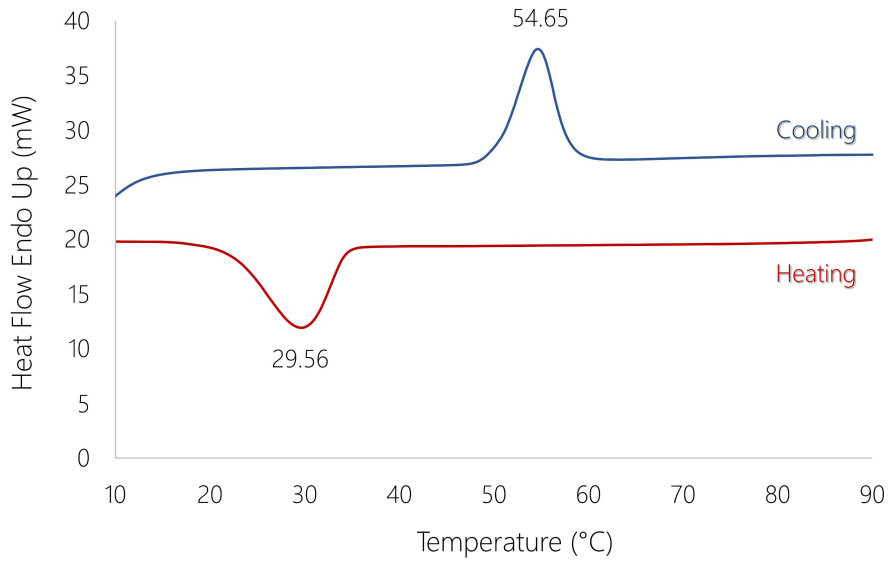

DSC3. *Thermal profile of CoBPDC1 and CoBPDC2.*

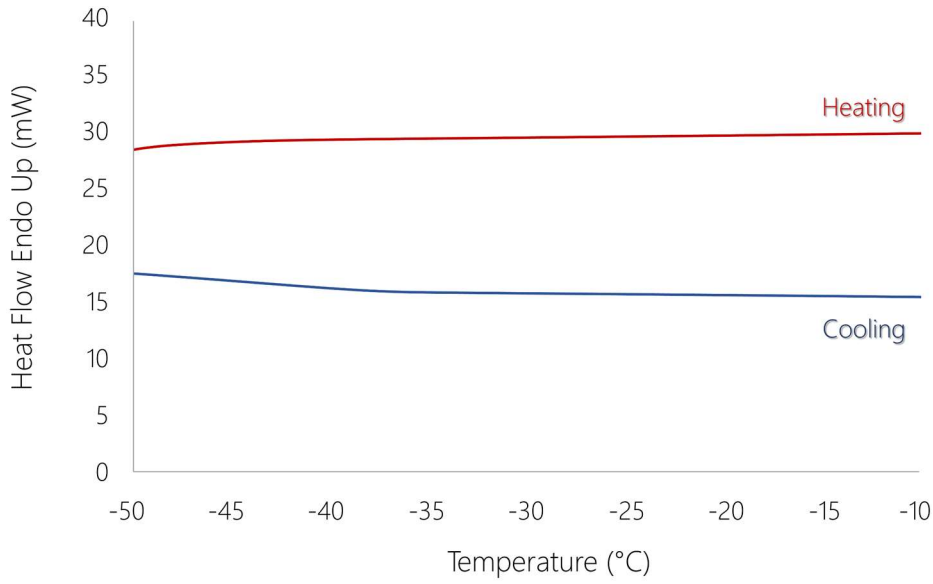

DSC4. *Thermal profile of IRMOF-9 after soaking in isopropanol.*

A.7 · XRPD patterns

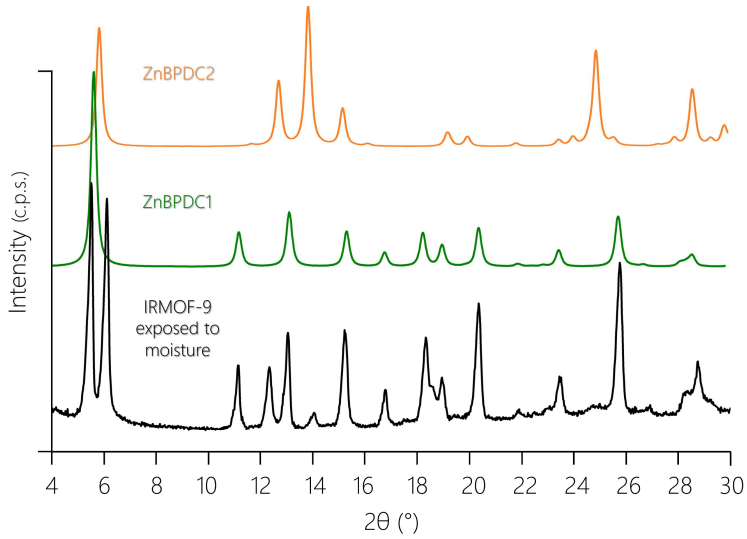

XRPD1. *Stacked XRD patterns of IRMOF-9 (measured) after the degradation due to moisture (black), and the two Zn-BPDC phases synthesized in water (green and orange, patterns are calculated from SCXRD data using the Mercury software[56]). ZnBPDC1 structure is taken from the published data (data collection at 296K); ZnBPDC2 structure has been determined at 100K.*

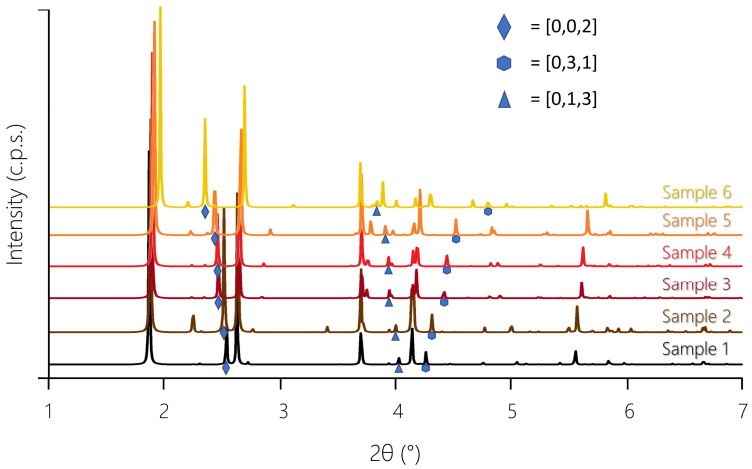

XRPD2. *Stacked simulated patterns of the six TiO_x@IRMOF-9 analysed samples. The shift of three distinctive reflections highlighted in XRPD2 is clearly recognisable.*

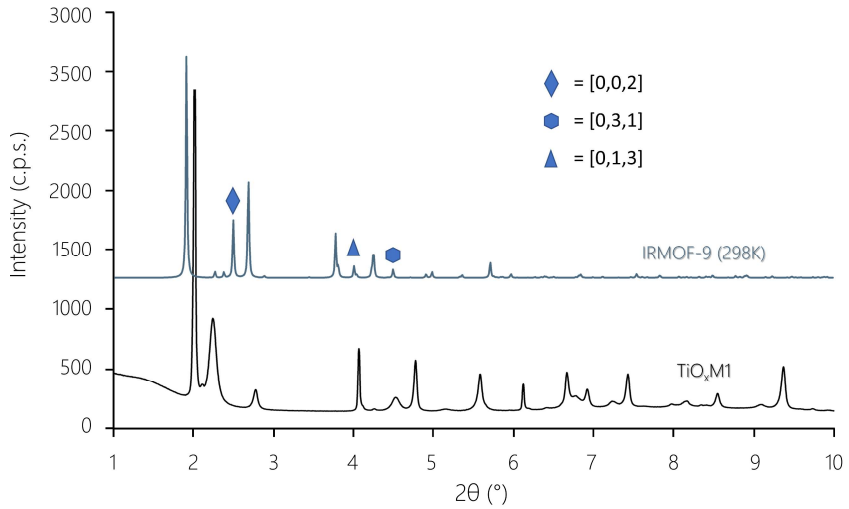

XRPD3. *Measured XRPD pattern of TiO_xM1 and simulated pattern of IRMOF-9 at 298K (black and grey-blue line respectively). Strong differences in the peak width at half maximum between different reflections can be recognised in the measured pattern. For IRMOF-9, three reflections have been highlighted, which are likely to shift dramatically with the strong cell variations seen after the treatment (affecting mainly the b and c crystallographic axis of the unit cell). The simultaneous presence of different unit cells among different crystal domains of the bulk, as seen in the case of TiO_x@IRMOF-9 (paragraph 3.3.1, chapter III), could lead to the broadening of only certain class of reflections, while keeping sharp the other ones.*

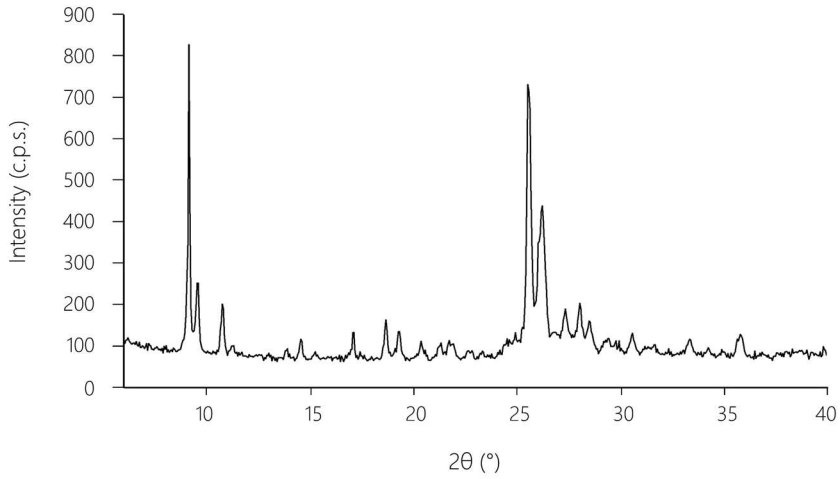

XRPD4. *Methylene blue chloride pentahydrate XRD pattern*

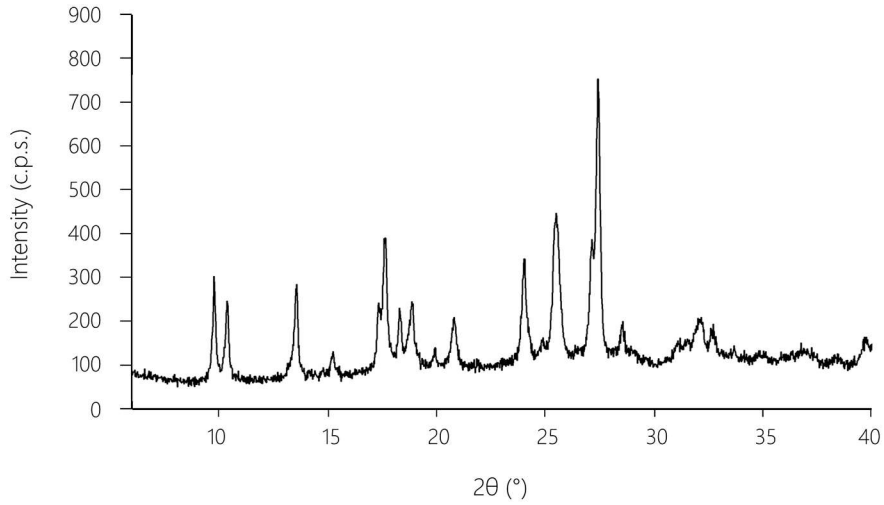

XRPD5. *XRD pattern of [(MB)$CuCl_2$] after the mechanochemical synthesis.*

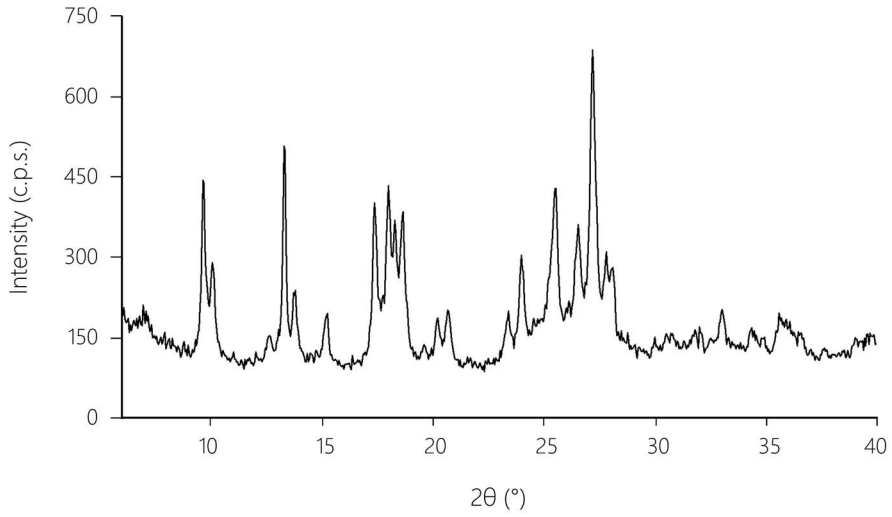

XRPD6. *XRD pattern of [(MB)$AgCl_2$] after the mechanochemical synthesis.*

A.8 · ICP-OES additional data

Soaking time (days)	Zn concentration (mg/l)	Co concentration (mg/l)
1	1.36 ± 0.03	0.91 ± 0.01
2	0.917 ± 0.002	1.318 ± 0.003
3	0.79 ± 0.02	1.48 ± 0.02
4	0.47 ± 0.01	1.77 ± 0.01
7	0.08 ± 0.003	2.03 ± 0.01
10	0	2.29 ± 0.02
14	0	2.54 ± 0.03

Table A.8.1. Zn and Co concentration measured by ICP-OES analyses on sample of IRMOF-9 at different soaking time (Soaking conditions: 0.2 M $CoCl_2$ solution at 305 K).

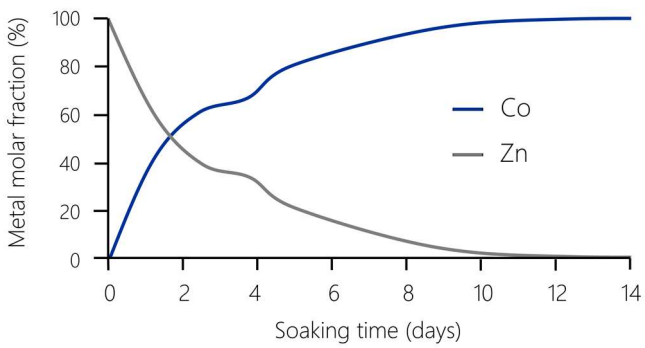

Graph A.8.1. Zn and Co composition trend during the transmetalation process. The treatment has been carried out at 305K to speed up the transformation. The plotted values are taken from Table ICP1.

A.9 · Computational details

DFT calculations on the methylene blue complexes were initially carried out with the Gaussian 09 package[138] at B97D[131] and B3LYP[128] level of theory. The experimental trigonal planar coordination was observed only for Cu^+ ion with a geometry quite different compared to the crystallographic one. The scarce capability of these DFT calculations to reproduce the experimental structures is further corroborated in the Ag^+ species, since the metal is linearly bound by two chlorides, as occurs for the Au^+ ion, while the MB^+ cation lies unbound in close proximity forming an ionic pair. In the gold case, the usage of the Douglas-Kroll-Hess calculations (DKH)[139] to account for 2nd order scalar relativistic effects did not improve the situation with respect to standard DFT methods.
Optimised structures were tested to be minima based through the vibrational frequencies calculations even though the chemical nature is invariably questionable. Some calculations were based on the CPCM model[129,140] for the CH_2Cl_2 solvent, the same used in the experiments. The effective Stuttgart/Dresden core potential (SDD)[141] was adopted for the metals, while for all the other atomic species the basis set was 6-31G, with the addition of the polarisation functions (d,p). Solid state calculations with CRYSTAL[130] were performed using the B97D and BLYP functionals. The POB triple-zeta valence with polarisation basis set has been used for all the atomic species.

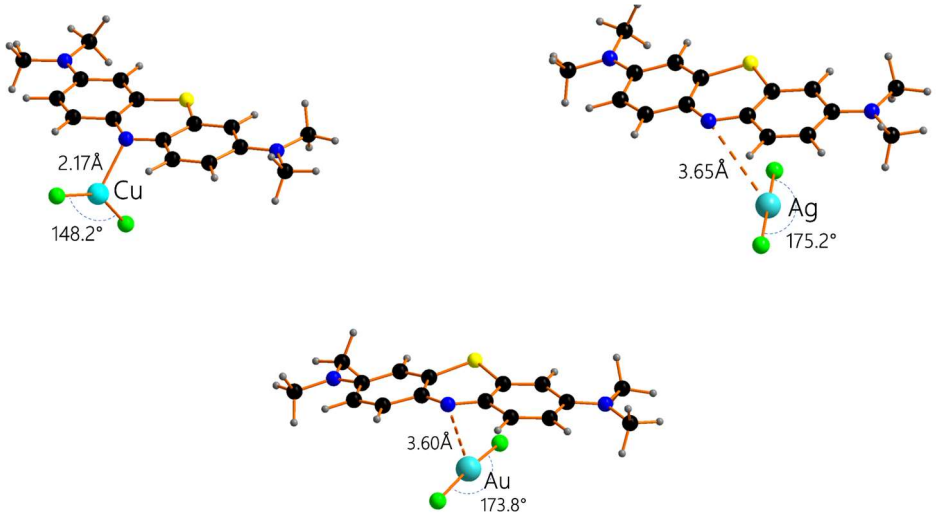

Figure A.10. Geometry optimisation results for [(MB)CuCl$_2$], [(MB)AgCl$_2$] and (MB)[AuCl$_2$] systems performed with Gaussian09 software.

A.10 · Software list

SCXRD data processing

- APEX3 version 2016.1-0[132]
- CrysAlisPro version 1.171.38.43[57]

Crystal structure solution and refinement from SCXRD

- Olex2 version 1.2 © OlexSys Ltd. 2004 – 2017[48]

XRPD data processing and structure solution

- DASH Software version 3.3.6[142]
- EXPO2014 version 1.16.09[143]

Crystal structure analysis and graphics

- Mercury CSD version 3.9[56]

Structural literature research

- ConQuest version 1.19[144]

XRPD and DSC patterns graphics

- OriginPro 8 SR0 version 8.0724 (B724)

Monte Carlo simulations

- Zurich Oak Ridge Disorder Simulation[103]

Total scattering patterns graphics

- ParaView version 5.3.0[145]

DFT calculations

- Gaussian 09[138]
- CRYSTAL14[130]

Bibliography

1 R. P. Feynman, *Eng. Sci.*, 1960, **23**, 22–36.
2 A. Desiraju, Gautam R.; Vittal, Jagadese J.; Ramanan, *Crystal Engineering: a Textbook*, World Scientific Publishing Co. Pte. Ltd., 2011.
3 S. R. Batten, N. R. Champness, X.-M. Chen, J. Garcia-Martinez, S. Kitagawa, L. Öhrström, M. O'Keeffe, M. Paik Suh and J. Reedijk, *Pure Appl. Chem.*, 2013, **85**, 1715–1724.
4 S. R. Batten, N. R. Champness, X.-M. Chen, J. Garcia-Martinez, S. Kitagawa, L. Öhrström, M. O'Keeffe, M. P. Suh and J. Reedijk, *CrystEngComm*, 2012, **14**, 3001.
5 M. O. Keeffe, M. A. Peskov, S. J. Ramsden and O. M. Yaghi, *Acc. Chem. Res.*, 2008, **41**, 1782–1789.
6 H. Li, M. Eddaoudi, M. O'Keeffe and O. M. Yaghi, *Nature*, 1999, **402**, 276–279.
7 H. Furukawa and O. M. Yaghi, *J. Am. Chem. Soc.*, 2009, **131**, 8875–8883.
8 M. Fujita, S. Washizu, K. Ogura and Y. J. Kwon, *J. Am. Chem. Soc.*, 1994, **116**, 1151–1152.
9 S. S. Y. Chui, S. M. F. Lo, J. P. H. Charmant, a G. Orpen and I. D. Williams, *Science (80-.).*, 1999, **283**, 1148–1150.
10 A. Phan, A. U. Czaja, F. Gandara, C. B. Knobler and O. M. Yaghi, *Inorg. Chem.*, 2011, **50**, 7388–7390.
11 K. S. Suslick, P. Bhyrappa, J. H. Chou, M. E. Kosal, S. Nakagaki, D. W. Smithenry and S. R. Wilson, *Acc. Chem. Res.*, 2005, **38**, 283–291.
12 F. G. Cirujano, E. López-Maya, M. Rodriguez-Albelo, E. Barea, J. A. R. Navarro and D. E. De Vos, *ChemCatChem*, , DOI:10.1002/cctc.201700784.
13 W. Wang, X. Xu, W. Zhou and Z. Shao, *Adv. Sci.*, , DOI:10.1002/advs.201600371.
14 H. Furukawa, K. E. Cordova, M. O'Keeffe and O. M. Yaghi, *Science*, 2013, **9**, 1230444.
15 W. Steffen, J. Grinevald, P. Crutzen and J. McNeill, *Philos. Trans. R. Soc. A Math. Phys. Eng. Sci.*, 2011, **369**, 842–867.
16 P. J. Crutzen, *Nature*, 2002, **415**, 23–23.
17 https://climate.nasa.gov/.
18 https://climate.nasa.gov/vital-signs/carbon-dioxide/.
19 A. Schoedel, Z. Ji and O. M. Yaghi, *Nat. Energy*, 2016, **1**, 16034.
20 J. W. Maina, C. Pozo-Gonzalo, L. Kong, J. Schütz, M. Hill and L. F. Dumée, *Mater. Horiz.*, 2017, **4**, 345–361.
21 J. Goldsmith, A. G. Wong-Foy, M. J. Cafarella and D. J. Siegel, *Chem. Mater.*, 2013, **25**, 3373–3382.
22 D. A. Gómez-Gualdrón, Y. J. Colón, X. Zhang, T. C. Wang, Y.-S. Chen, J. T. Hupp, T. Yildirim, O. K. Farha, J. Zhang and R. Q. Snurr, *Energy Environ. Sci.*, 2016, **9**, 3279–3289.
23 I. Erucar and S. Keskin, *J. Mater. Chem. B*, , DOI:10.1039/C7TB01764B.
24 R. C. Huxford, J. Della Rocca and W. Lin, *Curr. Opin. Chem. Biol.*, 2010, **14**, 262–268.
25 S. Keskin, K. Seda and S. Kızılel, *Ind.Eng.Chem.Res.*, 2010, **50**, 1799–1812.
26 I. Erucar and S. Keskin, *Ind. Eng. Chem. Res.*, 2016, **55**, 1929–1939.
27 M. C. Bernini, D. Fairen-Jimenez, M. Pasinetti, A. J. Ramirez-Pastor and R. Q. Snurr, *J. Mater. Chem. B*, 2014, **2**, 766.
28 L. L. Tan, H. Li, Y. Zhou, Y. Zhang, X. Feng, B. Wang and Y. W. Yang, *Small*, 2015, **11**, 3807–3813.
29 L. M. Hayes, C. E. Knapp, K. Y. Nathoo, N. J. Press, D. A. Tocher and C. J. Carmalt, *Cryst.*

Growth Des., 2016, **16**, 3465–3472.
30 M. Hoshino, A. Khutia, H. Xing, Y. Inokuma and M. Fujita, *IUCrJ*, 2016, **3**, 139–151.
31 S. Lee, E. A. Kapustin and O. M. Yaghi, *Science (80-.).*, 2016, **353**, 808–811.
32 L. E. Kreno, K. Leong, O. K. Farha, M. Allendorf, D. Van Richard P. and J. T. Hupp, *Chem. Rev. (Washington, DC, United States)*, 2012, **112**, 1105–1125.
33 Z. Z. Lu, R. Zhang, Y. Z. Li, Z. J. Guo and H. G. Zheng, *J. Am. Chem. Soc.*, 2011, **133**, 4172–4174.
34 F. Drache, V. Bon, I. Senkovska, M. Adam, A. Eychmüller and S. Kaskel, *Eur. J. Inorg. Chem.*, 2016, **2016**, 4483–4489.
35 L. Beauvais, M. Shores and J. Long, *J. Am. Chem. Soc.*, 2000, **8**, 2763–2772.
36 I. Stassen, B. Bueken, H. Reinsch, J. F. M. Oudenhoven, D. Wouters, J. Hajek, V. Van Speybroeck, N. Stock, P. M. Vereecken, R. Van Schaijk, D. De Vos and R. Ameloot, *Chem. Sci.*, 2016, **7**, 5827–5832.
37 S. Pramanik, C. Zheng, X. Zhang, T. J. Emge and J. Li, *J. Am. Chem. Soc.*, 2011, 133, 4153–4155.
38 F. P. Doty, C. A. Bauer, A. J. Skulan, P. G. Grant and M. D. Allendorf, *Adv. Mater.*, 2009, **21**, 95–101.
39 R. Vaidhyanathan, D. Bradshaw, J. N. Rebilly, J. P. Barrio, J. A. Gould, N. G. Berry and M. J. Rosseinsky, *Angew. Chemie - Int. Ed.*, 2006, **45**, 6495–6499.
40 N. a Rakow and K. S. Suslick, *Nature*, 2000, **406**, 710–713.
41 J. A. Gustafson and C. E. Wilmer, *J. Phys. Chem. C*, 2017, acs.jpcc.6b09740.
42 Z. Wang and S. M. Cohen, *Chem. Soc. Rev.*, 2009, **38**, 1315.
43 S. M. Cohen, *Chem. Rev.*, 2012, **112**, 970–1000.
44 M. Lalonde, W. Bury, O. Karagiaridi, Z. Brown, J. T. Hupp and O. K. Farha, *J. Mater. Chem. A*, 2013, **1**, 5453.
45 X.-J. Wang, P.-Z. Li, L. Liu, Q. Zhang, P. Borah, J. D. Wong, X. X. Chan, G. Rakesh, Y. Li and Y. Zhao, *Chem. Commun.*, 2012, **48**, 10286.
46 J. A. Botas, G. Calleja, M. Sánchez-Sánchez and M. G. Orcajo, *Langmuir*, 2010, **26**, 5300–5303.
47 A. L. Spek, *Acta Crystallogr. Sect. D Biol. Crystallogr.*, 2009, **65**, 148–155.
48 O. V. Dolomanov, L. J. Bourhis, R. J. Gildea, J. A. K. Howard and H. Puschmann, *J. Appl. Crystallogr.*, 2009, **42**, 339–341.
49 D. S. Sholl and R. P. Lively, *J. Phys. Chem. Lett.*, 2015, **6**, 3437–3444.
50 C. A. Trickett, K. J. Gagnon, S. Lee, F. Gándara, H. B. Bürgi and O. M. Yaghi, *Angew. Chemie - Int. Ed.*, 2015, **54**, 11162–11167.
51 A. K. Cheetham, T. D. Bennett, F.-X. Coudert and A. L. Goodwin, *Dalt. Trans.*, 2016, **45**, 4113–4126.
52 Z. Fang, B. Bueken, D. E. De Vos and R. A. Fischer, *Angew. Chemie - Int. Ed.*, 2015, **54**, 7234–7254.
53 M. Eddaoudi, J. Kim, N. Rosi, D. Vodak, J. Wachter, M. O'Keeffe and O. M. Yaghi, *Science*, 2002, **295**, 469–472.
54 S. A. Sapchenko, D. N. Dybtsev, D. G. Samsonenko and V. P. Fedin, *New J. Chem.*, 2010, **34**, 2445.
55 Cambridge Structural Database System, Version 5.37; Cambridge Crystallographic Data Centre, Cambridge, U.K.
56 C. F. Macrae, P. R. Edgington, P. McCabe, E. Pidcock, G. P. Shields, R. Taylor, M. Towler and J. Van De Streek, *J. Appl. Crystallogr.*, 2006, **39**, 453–457.

57 CrysAlisPro Software, Version 1.171.38.43, , Rigaku Oxford Diffraction, (2017), Oxford, UK.
58 P. Guo, D. Dutta, A. G. Wong-Foy, D. W. Gidley and A. J. Matzger, *J. Am. Chem. Soc.*, 2015, **137**, 2651–2657.
59 X. Y. Liu, S. J. Pai and S. S. Han, *J. Phys. Chem. C*, 2017, **121**, 7312–7318.
60 S. Rizzato, M. Moret, M. Merlini, A. Albinati and F. Beghi, *CrystEngComm*, 2016, **18**, 2455–2462.
61 L. Carlucci, G. Ciani, J. M. Garcia-Ruiz, M. Moret, D. M. Proserpio and S. Rizzato, *Cryst. Growth Des.*, 2009, **9**, 5024–5034.
62 J. Bernstein, R. J. Davey and J. O. Henck, *Angew. Chemie - Int. Ed.*, 1999, **38**, 3440–3461.
63 W. Tao, J.-M. Liu, Y.-J. Zheng and C.-Y. Sun, *Chin.J.Inorg.Chem.*, 2011, **27**, 2419.
64 A. Schneemann, V. Bon, I. Schwedler, I. Senkovska, S. Kaskel and R. A. Fischer, *Chem. Soc. Rev.*, 2014, **43**, 6062–6096.
65 X.-J. Wang, P.-Z. Li, L. Liu, Q. Zhang, P. Borah, J. D. Wong, X. X. Chan, G. Rakesh, Y. Li and Y. Zhao, *Chem. Commun.*, 2012, **48**, 10286–10288.
66 Q. Yao, J. Sun, K. Li, J. Su, M. V. Peskov and X. Zou, *Dalt. Trans.*, 2012, **41**, 3953–3955.
67 X. Song, S. Jeong, D. Kim and M. S. Lah, *CrystEngComm*, 2012, **14**, 5753.
68 T. K. Prasad, D. H. Hong and M. P. Suh, *Chem. - A Eur. J.*, 2010, **16**, 14043–14050.
69 W. Li, Y. Zhang, C. Zhang, Q. Meng, Z. Xu, P. Su, Q. Li, C. Shen, Z. Fan, L. Qin and G. Zhang, *Nat. Commun.*, 2016, **7**, 1–9.
70 X. Song, T. K. Kim, H. Kim, D. Kim, S. Jeong, H. R. Moon and M. S. Lah, *Chem. Mater.*, 2012, **24**, 3065–3073.
71 C. Heering, I. Boldog, V. Vasylyeva, J. Sanchiz and C. Janiak, *CrystEngComm*, 2013, **15**, 9757.
72 C. K. Brozek, V. K. Michaelis, T.-C. Ong, L. Bellarosa, N. López, R. G. Griffin and M. Dincă, *ACS Cent. Sci.*, 2015, **1**, 252–260.
73 S. M. Cohen, *Chem. Sci.*, 2010, **1**, 32.
74 A. Zimpel, T. Preiß, R. Röder, H. Engelke, M. Ingrisch, M. Peller, J. O. Rädler, E. Wagner, T. Bein, U. Lächelt and S. Wuttke, *Chem. Mater.*, 2016, **28**, 3318–3326.
75 S. Wang, W. Deng, L. Yang, Y. Tan, Q. Xie and S. Yao, *ACS Appl. Mater. Interfaces*, 2017, **9**, 24440–24445.
76 P. Hirschle, T. Preiß, F. Auras, A. Pick, J. Völkner, D. Valdepérez, G. Witte, W. J. Parak, J. O. Rädler and S. Wuttke, *CrystEngComm*, 2016, **18**, 4359–4368.
77 J. M. Zamaro, N. C. Pérez, E. E. Miró, C. Casado, B. Seoane, C. Téllez and J. Coronas, *Chem. Eng. J.*, 2012, **195–196**, 180–187.
78 M. Zhao, T. Chen and C. Deng, *RSC Adv.*, 2016, **6**, 51670–51674.
79 J. H. Im, E. Kang, S. J. Yang, H. J. Park, J. Kim and C. R. Park, *Bull. Korean Chem. Soc.*, 2014, **35**, 2477–2480.
80 M. Mueller, S. Hermes, K. Kaehler, M. Muhler and R. a Fischer, *Abstr. Pap. Am. Chem. Soc.*, 2008, **235**, 4576–4587.
81 F. Schröder, D. Esken, M. Cokoja, M. W. E. Van Den, O. I. Lebedev, G. Van Tendeloo, B. Walaszek, H. Limbach, B. Chaudret and R. a Fischer, 2008, 6119–6130.
82 M. Zhang, J. Guan, B. Zhang, D. Su, C. T. Williams and C. Liang, *Catal. Letters*, 2012, **142**, 313–318.
83 M. Müller, S. Turner, O. I. Lebedev, Y. Wang, G. Van Tendeloo and R. A. Fischer, *Eur. J. Inorg. Chem.*, 2011, **5**, 1876–1887.
84 J. Zhu, P. C. Wang and M. Lu, *Appl. Catal. A Gen.*, 2014, **477**, 125–131.
85 L. Chen, H. Chen, R. Luque and Y. Li, *Chem. Sci.*, 2014, **5**, 3708–3714.
86 Z. Guo, C. Xiao, R. V. Maligal-Ganesh, L. Zhou, T. W. Goh, X. Li, D. Tesfagaber, A. Thiel and

W. Huang, *ACS Catal.*, 2014, **4**, 1340–1348.
87 L. Chen, H. Chen and Y. Li, *Chem. Commun.*, 2014, **50**, 14752–14755.
88 Y. Pan, D. Ma, H. Liu, H. Wu, D. He and Y. Li, *J. Mater. Chem.*, 2012, **22**, 10834.
89 Y. K. Park, S. B. Choi, H. J. Nam, D.-Y. Jung, H. C. Ahn, K. Choi, H. Furukawa and J. Kim, *Chem. Commun.*, 2010, **46**, 3086–3088.
90 M. Zahmakiran, *Dalt. Trans.*, 2012, **41**, 12690.
91 A. S. Hall, A. Kondo, K. Maeda and T. E. Mallouk, *J. Am. Chem. Soc.*, 2013, **135**, 16276–16279.
92 A. Fujishima, T. N. Rao and D. A. Tryk, *J. Photochem. Photobiol. C Photochem. Rev.*, 2000, **1**, 1–21.
93 A. Wold, *Chem. Mater.*, 1993, **2912**, 280–283.
94 M. Müller, X. Zhang, Y. Wang and R. A. Fischer, *Chem. Commun.*, 2009, **5**, 119–121.
95 T. Egami and S. J. L. Billinge, *'Underneath the Bragg Peaks'*, 2003.
96 S. Sharma, S. K. Ghosh, M. Kumar and J. N. Sharma, *Polyhedron*, 2015, **100**, 290–295.
97 Y. Liu, R. Zheng, Z. Han, K. Gong, X. He and X. Zhai, *J. Solid State Chem.*, 2015, **231**, 169–174.
98 C. Daniel and H. Hartl, *J. Am. Chem. Soc.*, 2005, **127**, 13978–13987.
99 A. Adach, M. Daszkiewicz and M. Cieślak-Golonka, *Polyhedron*, 2012, **47**, 104–111.
100 L. B. Fullmer, R. H. Mansergh, L. N. Zakharov, D. A. Keszler and M. Nyman, *Cryst. Growth Des.*, 2015, **15**, 3885–3892.
101 Rigaku Oxford Diffraction, (2017), CrysAlisPro Software System, Version 1.171.38.43, , Oxford, UK.
102 T. Proffen and T. R. Welberry, *Phase Transitions*, 1998, **67**, 373–397.
103 M. Chodkiewicz, *Acta Crystallogr. Sect. A*, 2010, 215–216.
104 C. Mealli and D. M. Proserpio, *J. Chem. Educ.*, 1990, **67**, 399.
105 I. H. Filip, E. Gál, I. Lupan, M. Perde-Schrepler, P. Lönnecke, M. Surducan, L. I. Găină, E. Hey-Hawkins and L. Silaghi-Dumitrescu, *Dalt. Trans.*, 2014, **44**, 615–629.
106 V. Kumar, N. Upadhyay and A. Manhas, *J. Mol. Struct.*, 2015, **1099**, 135–141.
107 J. J. H. Edema, S. Gambarotta, A. Meetsma, A. L. Spek, W. J. J. Smeetsc and M. Y. Chiangd, .
108 S. V. Rosokha and J. K. Kochi, *J. Am. Chem. Soc.*, 2007, **129**, 3683–3697.
109 T. Okamoto, M. Kuratsu, M. Kozaki, K. Hirotsu, A. Ichimura, T. Matsushita and K. Okada, *Org. Lett.*, 2004, **6**, 3493–3496.
110 A. G. Cook, R. M. Tolliver and J. E. Williams, *J. Chem. Educ.*, 1994, **71**, 160–161.
111 W. S. Kima, G. T. Janga, J. E. Leea and D. S. Rheea, *Energy Procedia*, 2014, **61**, 2456–2459.
112 L. Bergamonti, I. Alfieri, A. Lorenzi, A. Montenero, G. Predieri, R. Di Maggio, F. Girardi, L. Lazzarini and P. P. Lottici, *J. Sol-Gel Sci. Technol.*, 2014, **73**, 91–102.
113 M. Cen- and A. Medical, *Arch. Intern. Med.*, 2015, **113**, 578–585.
114 Editorials, *J. Am. Med. Soc.*, 1935, **105**, 721–722.
115 G. C. Geiger, *J. Am. Med. Soc.*, 1932, **100**, 59.
116 P. Kaufmann, *Dtsch. Mediyinische Wochenschrift*, 1919, 1365.
117 B. Coulibaly, A. Zoungrana, F. P. Mockenhaupt, R. H. Schirmer, C. Klose, U. Mansmann, P. E. Meissner and O. Müller, *PLoS One*, 2009, **4**, 1–6.
118 P. M. Färber, L. D. Arscott, C. H. Williams, K. Becker and R. H. Schirmer, *FEBS Lett.*, 1998, **422**, 311–314.
119 C. M. Wischik, P. C. Edwards, R. Y. Lai, M. Roth and C. R. Harrington, *Proc. Natl. Acad. Sci. U S A*, 1996, **93**, 11213–11218.
120 M. M. Raj, A. Dharmaraja, S. J. Kavitha, K. Panchanatheswaran and D. E. Lynch, *Inorganica Chim. Acta*, 2007, **360**, 1799–1808.

121 S. B. Jonnalagadda and N. R. Gollapalli, *Bull. Chem. Soc. Ethiop.*, 2008, **22**, 85–91.
122 E. A. Moawed, M. A. A. Zaid and M. F. El-Shahat, *Anal. Lett.*, 2003, **36**, 405–422.
123 T. Issue, C. Article and H. O. T. Article, *Phys. Chem. Chem. Phys.*, 2000, **2**, 4313–4317.
124 V. L. Goedken, L. M. Vallarino and J. V. Quagliano, 1971, **10**, 2682–2685.
125 D. D. J. W. Mercer and H. A. Jenkins, *Inorganica Chim. Acta*, 2007, **360**, 3091–3098.
126 M. H. Emmert, J. B. Gary, J. M. Villalobos and M. S. Sanford, *Angew. Chemie - Int. Ed.*, 2010, 49, 5884–5886.
127 S. Sailaja, G. Swarnabala and M. V Rajasekharan, *Acta Crystallogr. Sect. C*, 2001, **C57**, 1162–1165.
128 A. D. Becke, *J. Chem. Phys.*, 1993, **98**, 5648–5652.
129 V. Barone and M. Cossi, *J. Phys. Chem. A*, 1998, **102**, 1995–2001.
130 R. Dovesi, R. Orlando, A. Erba, C. M. Zicovich-Wilson, B. Civalleri, S. Casassa, L. Maschio, M. Ferrabone, M. De La Pierre, P. D'Arco, Y. Noël, M. Causà, M. Rérat and B. Kirtman, *Int. J. Quantum Chem.*, 2014, **114**, 1287–1317.
131 S. Grimme, *J. Comput. Chem.*, 2006, **27**, 1787–1799.
132 Apex3 V2016.1-0, APEX3 software Copyright © 2003, 2004 Bruker Nonius AXS, Copyright © 2005-2016 Bruker.
133 G. M. Sheldrick, SADABS - Bruker Nonius area detector scaling and absorption correction - V2016/2.
134 A. Lausi, M. Polentarutti, S. Onesti, J. R. Plaisier and E. Busetto, *Eur. Phys. J. Plus*, 2015, **130**, 1–20.
135 P. R. Willmott, D. Meister, S. J. Leake, M. Lange, A. Bergamaschi, M. B??ge, M. Calvi, C. Cancellieri, N. Casati, A. Cervellino, Q. Chen, C. David, U. Flechsig, F. Gozzo, B. Henrich, S. Jäggi-Spielmann, B. Jakob, I. Kalichava, P. Karvinen, J. Krempasky, A. Lüdeke, R. Löscher, S. Maag, C. Quitmann, M. L. Reinle-Schmitt, T. Schmidt, B. Schmitt, A. Streun, I. Vartiainen, M. Vitins, X. Wang and R. Wullschleger, *J. Synchrotron Radiat.*, 2013, **20**, 667–682.
136 G. M. Sheldrick, *Acta Crystallogr. Sect. A Found. Crystallogr.*, 2015, **71**, 3–8.
137 G. M. Sheldrick, *Acta Crystallogr. Sect. C Struct. Chem.*, 2015, **71**, 3–8.
138 Gaussian 09, Revision E.01, M. J. Frisch, G. W. Trucks, H. B. Schlegel, G. E. Scuseria, M. A. Robb, J. R. Cheeseman, G. Scalmani, V. Barone, G. A. Petersson, H. Nakatsuji, X. Li, M. Caricato, A. Marenich, J. Bloino, B. G. Janesko, R. Gomperts, B. Mennucci.
139 M. Reiher, *Theor. Chem. Acc.*, 2006, **116**, 241–252.
140 M. Cossi, N. Rega, G. Scalmani and V. Barone, *J. Comput. Chem.*, 2003, **24**, 669–681.
141 M. Dolg, H. Stoll, H. Preuss and R. M. Pitzer, *J. Phys. Chem.*, 1993, **97**, 5852–5859.
142 W. I. F. David, K. Shankland, J. Van De Streek, E. Pidcock, W. D. S. Motherwell and J. C. Cole, *J. Appl. Crystallogr.*, 2006, **39**, 910–915.
143 A. Altomare, C. Cuocci, C. Giacovazzo, A. Moliterni, R. Rizzi, N. Corriero and A. Falcicchio, *J. Appl. Crystallogr.*, 2013, **46**, 1231–1235.
144 I. J. Bruno, J. C. Cole, P. R. Edgington, M. Kessler, C. F. Macrae, P. McCabe, J. Pearson and R. Taylor, *Acta Crystallogr. Sect. B Struct. Sci.*, 2002, **58**, 389–397.
145 J. Ahrens, C. Law, B. Geveci, James Ahrens and Charles L. B. Geveci, *Vis. Handb.*, 2005, **836**, 717–731.

Ringraziamenti

(Acknowledgements)

"Lost in thought and lost in time
While the seeds of life and the seeds of change were planted
Outside the rain fell dark and slow
While I pondered on this dangerous but irresistible pastime
I took a heavenly ride through our silence
I knew the moment had arrived
For killing the past and coming back to life
I took a heavenly ride through our silence
I knew the waiting had begun
And headed straight
into the shining sun"

Pink Floyd

"Coming Back to Life"
1993

Finché c'è un insegnante,
c'è uno scopo

Questo è ciò che ho imparato in questi anni di ricerca e fatica, di meraviglie e delusioni, sostegni e solitudini, e importanti lezioni.

Questa tesi è dedicata a tutti gli insegnanti, consci o meno del loro ruolo, che mi han permesso di diventare quel che sono e quel che diventerò, dando senso anche ai momenti più bui e dannosi.

Siete veramente molti e non per questo non proverò a ringraziarvi tutti, tuttavia devo scusarmi con alcuni di voi, poiché parte dei ringraziamenti non saranno in inglese.

While there is a teacher,
there is a purpose

This is what I learned during these years of research and efforts, wonders and delusions, support and solitude, and invaluable lessons.

This thesis is dedicated to all the teachers, aware or not of their role, who allowed me to grow up and become who I am and who I will be, making sense even of the darker and more harmful moments.

You truly are so many, but this will not stop me from trying to thank you all. However, I must apologise to some of you, since the major part of the following acknowledgements is not in English.

Le primissime parole di gratitudine vanno ai Professori **Giovanni Predieri**, **Alessia Bacchi**, **Claudia Graiff** e **Paolo Pelagatti**, che hanno seguito le mie avventure scientifiche sin dall'inizio.

Giovanni e **Claudia**, non dimenticherò mai i tempi passati in triennale tra seleniti e telluriti o, citando il primo titolo di tesi triennale proposto, "*tra chimica e serendipità*". Aver avuto l'occasione di tornare a lavorare con voi è stata un'inaspettata sorpresa, una ricchezza e un vero piacere.
Giovanni, spero che la carriera e l'età non mi portino mai via ciò che considero la cosa più importante che ho cerato di imparare da te: la genuina curiosità che conduce alle scoperte e crea le occasioni, il non dare mai nulla per esatto o per scontato, quello che ho apprezzato sin dai primi mesi in cui ho iniziato con fare ricerca sotto la tua guida e che ho sempre più identificato con ciò che prima di tutto definisce un vero scienziato.
Alessia e **Paolo**, la tesi magistrale svolta sotto la vostra guida è stata un'altra fondamentale tappa nella mia crescita come ricercatore. È proprio in quel periodo che ho imparato, poco a poco, cosa significa approcciarsi alla ricerca e ho consolidato la mia passione per la cristallografia, che mi ha portato molte più soddisfazioni che fatiche.
Alessia, proprio a tal riguardo ti devo un grazie speciale per l'impagabile aiuto che mi hai dato, sia nello studio del metodo cristallografico che nel promuovermi nel panorama scientifico e coinvolgermi in numerose attività, sia di ricerca che di divulgazione e insegnamento.
Paolo, il tuo mood tranquillo e propositivo mi han fatto sentire presto a mio agio nel discutere di ipotesi e chiederti consigli per le attività di laboratorio. Un plauso per aver costantemente sopportato i miei deliri e aver trovato sempre il tempo per ragionare con lucidità e flessibilità sui problemi chimici, attività in cui ti ho sempre considerato un esempio da seguire.

Un secondo enorme ringraziamento va a tutte le persone che compongono quella larga e variopinta famiglia che è il dipartimento di chimica, in particolare la sezione inorganica.
Rimanendo nella metafora, posso considerare i miei compagni di dottorato e borsisti come dei veri e propri fratelli su cui poter contare, a cui prestare aiuto, con cui condividere problemi, disagi, risate e tavolate di cibo: perché per brindare e mangiare insieme non ci vuole necessariamente un'occasione speciale. Ricordo con particolare gratitudine tutti i "fantasmi di inorganica", soprattutto **Davide Balestri**, **Irene Bassanetti**, **Anna Gatti**, **Marianna Pioli**, **Vittoria Marzaroli** e **Jacopo Andreo**.

Davide, da " 'n altro bolognese" a "nonno Balo" il passo è stato corto, perlomeno per come è volato questo periodo della mia vita. In questi anni sei stato un collega a cui chiedere opinioni su idee chimiche folli, un pizzaiolo, un coinquilino, uno psichiatra, un master di D&D e uno spacciatore di droga (perlopiù caffè, ma a volte anche salumi vari). In ogni istante sei stato prima di tutto un prezioso amico con cui ho affrontato molte delle difficoltà che incontriamo nel nostro lavoro, oltre che un chimico dalle capacità fuori dal comune e dall'inossidabile dedizione.

Irene, una delle tappe più importanti della mia evoluzione personale credo sia stato passare da "ginger" a "psycho". Insieme a questa versatile identità mentale, ti devo i momenti di confronto, i consigli e le tue opinioni sincere da cui non di rado ho avuto occasione di imparare molto.

Anna, un altro dei membri originari dei "fantasmi di inorganica", una delle prime persone con cui ho condiviso i momenti di follia dovuti ad assurdità legate a chimica, burocrazia e molto altro. Grazie dell'aiuto sempre presente e dell'esempio che sei stata per me come ricercatrice seria e competente.

Marianna, sin dalla tua entrata in tesi magistrale nel lab 050 apprezzai la tua solarità e gentilezza, che insieme alla tua semplicità e bravura nel dedicarti alla ricerca ti rendono una delle migliori compagne di laboratorio che mi possa augurare di avere. Grazie di aver rallegrato molte giornate e per la costante disponibilità.

Vittoria, la tua capacità di occuparti di duemila cose contemporaneamente e non mollare mai di nemmeno un millimetro l'obiettivo è segno di una disciplina e di una passione veramente rare, che nemmeno le montagne di stress e difficoltà tipiche del dottorato riescono ad abbattere. La passione che metti nella tua ricerca e la voglia di lavorare seriamente per imparare tutto ciò che può servire è di grande esempio per me. Grazie per i confronti, i consigli e le risate che hanno alleggerito le nostre giornate.

Jacopo, sebbene il tuo arrivo sia stato il più recente, non posso non ringraziarti sinceramente di tutti i momenti di pausa e confronto avuti insieme. Una chiacchierata con te è capace in una mancata di minuti di dare preziosi consigli di chimica, conforto e motivazione in una giornata pesante, idee che mai sarebbero nate, raffinati aneddoti e "... una sigaretta?". Negli ultimi mesi di dottorato, i più pesanti ed intensi, ho trovato in te una persona amichevole e vera, senza la quale non sarei arrivato fino a questo punto con la stessa ricchezza d'animo.

Ringrazio per il prezioso aiuto nelle attività di ricerca i tesisti Luca Fornasari e Prisca Montali, a cui devo una parte importante del lavoro sperimentale di questa tesi.

Infine, la famiglia include anche tutta la parte "strutturata" che ha reso ogni fatica più sopportabile e che mi ha regalato sorrisi ed aiuto un numero indefinibile di volte.

Un grande grazie a Giorgio Pelosi, buon amico sin dai tempi del biennio magistrale, una persona con cui sento di potermi prendere qualche minuto per scambiare quattro chiacchiere a mente serena e stemperare gli stress del lavoro. Ricordo sempre con piacere le nostre cene liberatorie, e le divagazioni, cristallografiche e non, in cui ci buttavamo quando riuscivo a trovarti libero nel tuo ufficio. La tua gentilezza, calma, e cultura sono sempre state per me un importante esempio da seguire.

"Ma poi Dio disse: Canossa sia! E tutto fu luce." Come si potrebbe mai affrontare la routine del dottorando se non sapendo che prima o poi, inaspettatamente, Luciano Marchiò farà irruzione nello "stanzino dottorandi" con una parola per chiunque incroci il suo sguardo. "Aah stai bene te… vai al sincrotrone, mangi i sardoni, capisci poco…", "Stasera Canossa ha sbagliato le pillole, ha scambiato quelle per la pressione con quelle per il colesterolo"… a pensarci ne escono a decine. Ma in questo sfondo di momenti improvvisamente divertenti apparivano ogni tanto brevi ed incisive lezioni cristallografiche e consigli che potevano cambiare l'approccio a quel che si stava facendo. Grazie Lucio per i tuoi interventi e la tua positività contagiosa ed inesauribile.

Un grazie di cuore a Chiara Massera, che insieme a Claudia mi ha accompagnato nel mio percorso dai tempi della tesi triennale con infinite parole di amicizia, incoraggiamento e consiglio. Vivere il dottorato senza visitare di tanto in tanto il vostro ufficio per aggiornamenti sui diffrattometri, chiarimenti cristallografici o un semplice saluto e un pezzo di cioccolata sarebbe stato molto più triste e vuoto.

To all the friends I met during my periods abroad

During my PhD course, I had the honour and pleasure of spending periods abroad as guest research fellow, and I could not imagine meeting so many nice and welcoming people, as well as so incredibly valuable scientists.

First, I must thank Prof **Martin Schmidt** and Dr **Lothar Fink** for the short but intense period I spent at Frankfurt University. **Martin**, I guess that you would like me to say it in Italian, as we used in Frankfurt, so: grazie infinite per la tua gentilezza e per i consigli cristallografici che mi hai dato. Avere avuto la possibilità di stringere amicizia con te è stata una fortuna inaspettata di cui sarò sempre grato alla tua disponibilità e ad Alessia. I tanti discorsi che abbiamo avuto durante il mio periodo a Francoforte e le tue visite in Italia sono momenti felici che ricorderò sempre con molto piacere, e che spero si aggiungano a molti altri negli anni a venire.

I owe a huge thank also to Prof **Juan Manuel García-Ruiz**, Dr **Duane Choquesillo-Lazarte**, Dr **Cristobal Verdugo** and Dr **Juan Morales-Sanchez**, who welcomed me in Granada during my 6-months exchange period. Dear **Juanma**, working with you has been a constant inspiration. Your passion and dedication are what I consider among the most powerful qualities for a scientist and an important example to follow. **Duane**, **Cristobal**, your friendly words and your availability really made my stay at the institute pleasant and productive. I'm sincerely looking forward to meeting you all again soon and keeping in touch both as friends and researchers.

Last but not the least, I gratefully thank the people who hosted me in Zurich and granted me a ticket for an amazing journey in the reciprocal space: Prof **Hans-Beat Bürgi** and Dr **Ruggero Frison**. It is unbelievable the mountain of things I leaned while I was there, and how it changed my approach to crystallography. **Hans-Beat**, with few words at a time you have been able to open my head, turn the earth of my crystallographic bases and plant lots of seeds which I will try my best to take care of. **Ruggero**, although your hectic routine you found the time to teach me the bases that allowed us to work on our scientific questions and proceed towards a solution. Working with both of you has been very important for my education, not only for the notions I learned on diffuse scattering analyses, but also for the inspiration I got from your humble and meticulous approach to crystallographic studies.

Un grazie sincero anche a **Federica Bertolotti** per la disponibilità e tutti i consigli che mi ha dato, e per avermi messo in contatto con Ruggero Frison rendendo possibile la collaborazione che ha cambiato il mio approccio alla cristallografia.

Ringrazio anche tutte le persone con cui che ho avuto la fortuna di collaborare in questi anni e che hanno arricchito il lavoro di tesi con dati di grande importanza: il dott. **Nicola Demitri** (Sincrotrone ELETTRA, Trieste) per i dati di diffrazione su cristallo singolo con luce di sincrotrone, la Dott.ssa **Monica Mattarozzi** per le analisi ESEM, i Dott. **Carlo Mealli**, **Gabriele Manca** e **Andrea Ienco** (Istituto ICCOM-CNR) per i calcoli computazionali.

Ricalcando le parole di apertura, ringrazio tutti coloro che mi hanno lasciato degli insegnamenti, e che hanno nutrito la mia cultura e la mia persona: i miei amici istruttori e praticanti di Kung Fu di Verona, i compagni di studi, avventure e disavventure degli anni passati come studente, gli ex colleghi di lavoro e quei vecchi e nuovissimi amici, che han lasciato un segno importante nel mio passato e nel mio presente.

Un ultimo ringraziamento, il più grande, va alla mia famiglia e in particolare ai miei genitori: i miei primi insegnanti. La vostra costante presenza mi ha da sempre insegnato ad impegnarmi, a perseverare, a credere, ad amare ciò che faccio e a donare ciò che posso, e lo ha fatto tramite un esempio costante che mai è vacillato, indipendentemente dal mio umore o dalle mie scelte in cui mi siete sempre stati vicini. Questo amore inesauribile ha lasciato la sua impronta su ogni mia conquista e sentirò sempre il suo impulso nei momenti più bui e nelle sfide più difficili.

Grazie